Alma Mater Studiorum – Università di Bologna

DOTTORATO DI RICERCA IN

INGEGNERIA CIVILE, CHIMICA, AMBIENTALE E DEI MATERIALI

Ciclo 35°

Settore Concorsuale: 08/B2 – SCIENZA DELLE COSTRUZIONI

Settore Scientifico Disciplinare: ICAR/08 – SCIENZA DELLE COSTRUZIONI

NANOMECHANICAL CHARACTERIZATION OF SOFT BIOELECTRONIC INTERFACES VIA MODELING-INFORMED ATOMIC FORCE MICROSCOPY

Presentata da: Giorgio Cortelli

Coordinatore Dottorato

Prof. Alessandro Tugnoli

Supervisore

Prof. Stefano de Miranda

Co-supervisori

Prof. Luca Patruno

Prof. Tobias Cramer

Esame finale anno 2023

RINGRAZIAMENTI

Prima di procedere con la trattazione, vorrei dedicare qualche riga a tutti coloro che mi sono stati vicini in questo percorso di crescita personale e professionale.

Ringrazio innanzitutto il mio relatore Prof. Stefano de Miranda per la sua disponibilità, la sua comprensione e la sua capacità di creare un ambiente di lavoro sano e stimolante. Insieme a lui, ringrazio i professori Luca Patruno, Tobias Cramer, e Beatrice Fraboni, che hanno saputo guidarmi con suggerimenti pratici nella mia ricerca dedicandomi tempo e soprattutto pazienza.

Ringrazio di cuore i miei genitori che mi hanno sempre supportato fornendomi i mezzi e l'amore per poter realizzare i miei sogni. Senza di loro nulla di tutto ciò sarebbe stato possibile. Ringrazio anche mia sorella che ha da sempre la capacità di farmi vedere le cose sotto altri punti di vista, arricchendo il mio pensiero. Ringrazio Dalia, senza la quale oggi sarei completamente un'altra persona. Il suo supporto, i suoi sorrisi e la sua pazienza sono stati fondamentali nell'affrontare i fallimenti tanto quanto nel condividere i successi.

Ringrazio i miei amici, soprattutto le 7P, per avermi ascoltato fino a tarda sera mentre gli spiegavo cosa non andava nella mia ricerca, ma soprattutto per le centinaia di chilometri percorsi insieme. Santiago, la via Romea, l'alta via numero 1 delle Dolomiti, sono momenti indelebili nella mia mente che hanno contribuito a rendere questi tre anni di dottorato indimenticabili. Un ringraziamento particolare a Zed.

Infine, ringrazio i miei nonni e la zia Anna, che fin da quando ho memoria mi hanno accudito, venendomi a prendere a scuola, preparandomi il pranzo ed aiutandomi a fare i compiti. Senza la loro pazienza, probabilmente non avrei mai intrapreso questo percorso, e per questo non smetterò mai di ringraziarli.

ABSTRACT

Interfaccia bioelettronica è un termine generico per indicare elettrodi progettati per scambiare segnali elettrici con sistemi biologici. La bioelettronica può trasdurre segnali attraverso l'interfaccia tra tessuto e dispositivo per misurare e regolare le attività biologiche a fini diagnostici e terapeutici. Poiché il corpo umano è intrinsecamente morbido ed in continuo movimento meccanico, i dispositivi impiantabili devono soddisfare tali condizioni meccaniche per essere biocompatibili e sicuri nell'integrazione a lungo termine con il corpo umano. La bioelettronica rigida attualmente applicata non soddisfa questi criteri e la mancata corrispondenza meccanica con i tessuti molli circostanti può scatenare risposte infiammatorie e causare l'instabilità delle funzioni del dispositivo, soprattutto in caso di impianto a lungo termine negli organi bersaglio. Negli ultimi anni, sono stati raggiunti traguardi significativi nell'elettronica flessibile ed estensibile e primi studi hanno utilizzato questi progressi per sviluppare interfacce bioelettroniche maggiormente biocompatibili da un punto di vista meccanico. Per raggiungere pienamente questo obiettivo, i progressi nella scienza dei materiali e nell'ingegneria dei dispositivi elettronici morbidi devono essere combinati con strumenti di caratterizzazione e modellazione quantitativa al fine di raggiungere una piena comprensione dei problemi meccanici che sono rilevanti all'interfaccia tra la tecnologia elettronica e i tessuti biologici.

Esempi di questi problemi meccanici sono i fenomeni che causano il danno del dispositivo, come la delaminazione, la formazione di microfratture eccessivamente ampie, o il deterioramento dello strato di incapsulamento. Inoltre, il dispositivo deve essere progettato per sostenere i carichi meccanici dovuti al maneggiamento ed inserzione. La morfologia della superficie del dispositivo ha un ruolo cruciale nel determinare le proprietà e le prestazioni dell'interfaccia bioelettronica morbida. Infatti, la superficie è il punto di contatto tra il sensore ed il corpo. I fenomeni che possono intaccare le prestazioni del dispositivo avvengono tutti localmente. Pertanto, una caratterizzazione meccanica microscopica è fondamentale per comprendere l'attivazione dei meccanismi di danneggiamento ed ottimizzare i dispositivi. Inoltre, i dispositivi devono interfacciarsi con parti del corpo eterogenee. Ciò rende cruciale

un'indagine locale delle proprietà meccaniche delle interfacce bioelettroniche morbide al fine di ottenere un buon accoppiamento tra dispositivo e tessuto. I meccanismi di danneggiamento avvengono quando il dispositivo è sottoposto a sforzi meccanici. Pertanto, solo una caratterizzazione meccanica *in situ*, ovvero svolta durante la deformazione, potrebbe fornire chiari indizi sui meccanismi a scala nanometrica attivati dalla deformazione che possono determinare il guasto del dispositivo. La combinazione di modelli interpretativi e metodi sperimentali consente una migliore comprensione dei meccanismi locali di dispositivi flessibili/estensibili e delle loro singole componenti. In questo contesto, i modelli analitici e numerici (FEM) basati sulla meccanica del continuo consentono di confrontare i parametri costitutivi dei materiali stimati su scala nanometrica con i corrispondenti valori su scala macro (cioè quelli utilizzati nella meccanica del continuo). Questo tipo di confronto è cruciale e può rivelare la necessità di introdurre fattori correttivi nei modelli basati sulla meccanica del continuo per tenere conto degli effetti tipici della nanoscala. L'ottimizzazione delle prestazioni di questi dispositivi può avvenire solo attraverso la progettazione di specifici setup sperimentali per la caratterizzazione meccanica locale *in situ* supportati da modelli predittivi. Solo una comprensione più approfondita di questi aspetti meccanici aprirà la strada a una progettazione ottimizzata della bioelettronica morbida indossabile e impiantabile, dando inizio a una nuova era di monitoraggio della salute, diagnosi e terapia.

Al giorno d'oggi stanno emergendo tecniche sperimentali per testare le proprietà meccaniche *in situ* su scala nanometrica. Tuttavia, queste tecniche spesso comportano l'uso combinato di due o più strumenti, risultando quindi costose e difficili da riprodurre in altri laboratori con altre configurazioni sperimentali. Pertanto, sono necessarie tecniche sperimentali di facile accesso e che richiedano la minima manipolazione possibile dei campioni. Il microscopio a forza atomica (AFM) è un buon candidato per ottenere la caratterizzazione meccanica locale *in situ* delle interfacce bioelettroniche morbide. L'AFM consente misure non distruttive su scala nanometrica in aria o addirittura in acqua e non richiede un alto vuoto e campioni conduttivi, a differenza del microscopio elettronico a scansione (SEM). Inoltre, il principio di funzionamento dell'AFM consente il sondaggio meccanico e il campionamento della topografia reale del campione contemporaneamente.

In questo lavoro sono riportate tecniche sperimentali *in situ* unicamente con AFM supportate da modelli interpretativi per la caratterizzazione di dispositivi planari e tridimensionali adatti per sperimentazioni biomediche *in vivo* e *in vitro*. La combinazione dei modelli proposti e delle tecniche sperimentali consente di ottenere informazioni riguardo alle proprietà meccaniche delle interfacce bioelettroniche morbide. In particolare, sono state indagate sia la nanomeccanica di un film sottile di oro su un substrato polimerico (Polidimetilsilossano PDMS), sia quella di *micropillars* stampati a getto d'inchiostro in 3D, soggetti a diversi stati deformativi. Le interfacce planari metallo-elastomero sono essenziali per i dispositivi elettronici estensibili, poiché la presenza di microfratture controllate consente al dispositivo di mantenere le sue prestazioni elettriche sotto sforzo. I risultati evidenziano la formazione di un'interfaccia diffusa tra il film metallico e il polimero, con un impatto importante sulle proprietà meccaniche ed elettriche. Inoltre, il metodo proposto di mappatura multicanale *in situ* consente di osservare la transizione indotta dalla deformazione dal trasporto ohmico al trasporto per effetto tunnel nei film sottili d'oro microfratturati. I *micropillars* stampati a getto d'inchiostro in 3D sono necessari per gli impianti biomedici di prossima generazione, per registrare segnali cellulari, per i biosensori e per la somministrazione di farmaci, poiché sono strutture tridimensionali elastiche, flessibili e conduttrici che consentono un'elevata risoluzione spaziale. Il metodo di caratterizzazione proposto consente di determinare in modo rapido e preciso le proprietà meccaniche, dando così la possibilità di parametrizzare le fasi di microfabbricazione e di studiare il loro impatto sul dispositivo finale.

ABSTRACT

The bioelectronic interface is a general term to indicate electrodes designed to exchange electrical signals with biological systems. Bioelectronics can transduce signals across the tissue and device interface to measure and regulate biological activities for diagnostic and therapeutic purposes in biomedical devices and healthcare applications. Since the human body is inherently soft and in continuous mechanical motion, implantable devices have to match such mechanical conditions in order to be biocompatible and safe in intimate, long-term integration with the human body. Currently applied, rigid bioelectronics does not fulfill these criteria and the mechanical mismatch with the surrounding soft tissue can trigger inflammatory responses and cause unstable device functions, especially with long-term implantation into target organs. In recent years, significant advances in flexible and stretchable electronics have been obtained and first studies translate these advances to bioelectronic interfaces in order to make them mechanically more biocompatible. To fully achieve this goal, advances in the material science and engineering of soft electronic devices have to be combined with quantitative characterization and modelling tools to achieve a full understanding of the mechanical issues that are relevant at the interface between electronic technology and biological tissue.

Examples of such important mechanical issues are phenomena that lead to the device failure, such as delamination, the formation of overly wide microcracks, or damage to the encapsulation layer. Additionally, the device must be developed to withstand mechanical loads during handling and insertion. The impact that surface morphology has on the properties and performance of a bioelectronic soft interface is crucial. Indeed, it is the surface that is the point of contact between the sensor and the body. The phenomena affecting the device's performances all occur locally. So that a microscopic mechanical characterization is mandatory to understand the activation of failure mechanism and optimize the devices. In addition, the devices must interface with heterogeneous body parts. This makes a local investigation of the mechanical properties of the soft bioelectronic interface crucial to establish good coupling with heterogeneous biological tissue. The failure mechanism take place when the device is operating under strain. Therefore, only a *in situ* mechanical characterization, i.e.

performed during the deformation, might give clear insights into the nanoscale mechanisms activated by deformation that led to device failure. The combination of interpretative models and experimental methods allows a greater understanding of the local working mechanisms of these stretchable/flexible devices and their components. In this context, analytical and numerical (FEM) models based on continuum mechanics allow comparison of the material constitutive parameters estimated at the nanoscale with the corresponding macroscale values (i.e. those used in continuum mechanics). This type of comparison is critical and can reveal the need to introduce corrective factors into continuum mechanics-based models to take into account effects typical of the nanoscale. Therefore, optimization of the performance of these devices can only occur through the design of specific experimental setups for local *in situ* mechanical characterization supported by predictive models. Only a deeper understanding of these mechanical aspects will pave the way to an optimized design of wearable and implantable soft bioelectronics initiating a new era of health monitoring, diagnosis, and therapeutic.

Experimental techniques for testing mechanical properties *in situ* at the nanoscale are emerging nowadays. However, these techniques often involve the combined use of two or more instruments, thus being expensive and difficult to reproduce in other laboratories with other experimental setups. Therefore, experimental techniques are needed that are easy to access and require as little sample handling as possible. The Atomic Force Microscope (AFM) is a good candidate to achieve *in situ* local mechanical characterization of soft bioelectronic interfaces. AFM allows nondestructive measurements at the nanoscale in air or even in water. AFM do not require high vacuum and conductive samples, as opposed to the Scanning Electron Microscope (SEM). In addition, the working principle of AFM allow mechanical probing and sampling of the real sample topography simultaneously.

In this work, *in situ* experimental techniques with solely AFM supported by interpretive models for the characterization of planar and three-dimensional devices suitable for *in vivo* and *in vitro* biomedical experimentations are reported. The combination of the proposed models and experimental techniques provide access to the local mechanical properties of soft bioelectronic interfaces. In particular, both the nanomechanics of hard thin gold films on soft polymeric substrates

(Poly(dimethylsiloxane) PDMS), and 3D inkjet printed micropillars, were investigated under different deformation states. Planar metal-elastomer interfaces are essential for stretchable electronic devices as the presence of controlled microcracks allow the device to maintain its electrical performance under strain. The findings highlight the formation of a diffuse interface between the metal film and the polymer with an important impact on the mechanical and electrical properties. Furthermore, the proposed *in situ* multi-channel mapping method allow to observe the strain-induced transition from ohmic transport to tunneling transport in microcracked gold thin films. 3D inkjet printed micropillars are needed in next-generation biomedical implants, cellular recording, biosensors, and drug delivery, since they are elastic, flexible, conducting 3D structures which allows high spatial resolution. The proposed characterization method provides rapid and precise determination of mechanical properties, thus giving the possibility to parametrize the microfabrication steps and investigate their impact on the final device.

SUMMARY

Ringraziamenti 3
Abstract 7

1 Introduction 13
1.1 State of the art of Soft Bioelectronic Interfaces 16
1.1.1 Physical biosensors 17
1.1.2 Electrical biosensors 18
1.1.3 Chemical biosensors 20
1.2 State of the art of *In situ* local characterization of soft bioelectronic interfaces 23
1.2.1 Tensile test 25
1.2.2 Bending test 29
1.2.3 Nanoindentation test 32
1.2.4 Micropillar compression test 33
1.3 My research project 35

2 Atomic Force Microscopy Nanomechanics of Hard Nanometer-Thick Films on Soft Substrates: Insights for Stretchable Conductors 39
2.1 Introduction 40
2.2 Experimental section/methods 43
2.2.1 PDMS/Au and PDMS/Ti/Au preparation 43
2.2.2 AFM characterization 43
2.2.3 Van der Pauw measurements 44
2.3 Results 45
2.3.1 Analytical Model 47
2.3.2 Experimental validation of the model 49
2.3.3 Nanomechanical and electrical properties influenced by thin film growth 51
2.4 Discussion and Conclusions 54
2.5 Supporting Information 57
2.5.1 Introduction of the analytical indentation model and linearization 57
2.5.2 FEM Model 58

3 *In situ* force microscopy to investigate fracture in stretchable electronics: insights on local surface mechanics and conductivity 61
3.1 Introduction 62
3.2 Experimental Section 64
3.2.1 PDMS/Cr/Au preparation 64
3.2.2 AFM Probe 64
3.2.3 AFM resonant frequencies investigation 65
3.2.4 AFM multichannel imaging 65
3.3 Result 66
3.4 Conclusions and Discussion 76
3.5 Supporting Information 78

4 Determination of Stiffness and the Elastic Modulus of 3D-printed micropillars with Atomic Force Microscopy-Force Spectroscopy 81
4.1 Introduction 82
4.2 Experimental Section/Methods 84
4.2.1 3D Inkjet printing micropillar arrays 84
4.2.2 3D printed micropillars length and diameter measurements 85
4.2.3 Sample preparation for AFM mechanical characterization . 86
4.2.4 AFM tip calibration 86
4.3 Results and Discussion 87
4.4 Conclusions 94
4.5 Supporting Information 96

5 Conclusions 99

List of Figures 105
List of Acronyms 109
List of Symbols 110

References 113

1 INTRODUCTION

The bioelectronic interface is a general term to indicate electrodes designed to be integrated and to communicate with biological systems. Bioelectronic interfaces can be established either on human skin (wearable bioelectronics) or inside the human body (implantable bioelectronics). [1,2] Bioelectronics can transduce signals across the tissue and device interface to measure and regulate biological activities for healthcare monitoring and disease treatment. Currently, a variety of bioelectronic devices are widely used, such as glucose sensors, cardiac pacemakers, and electrocorticograms. Unfortunately, most currently known high-performance electronic materials are based on hard and stiff inorganic conductors and semiconductors. Because the human body is soft and curvilinear, a safe, intimate, and long-term integration of a device with the human body calls for soft, biocompatible, and multifunctional devices. In this manner, the current rigid bioelectronics may induce inflammatory responses, particularly under long-term integration on the target organ. [2–7] This need has led many researchers to focus on the topic in recent years, giving rise to a new branch of electronic materials science and device engineering, which investigates the development, design, characterization, and possible application of deformable electronic devices that are compliant to a mechanically demanding environment while maintaining their electronic functionality. Recently, soft electronic devices have been developed for application in different fields such as low-invasive biomedical implants,[8,9] soft robotics [10], and electro-mechanical energy harvesters. [11] In the biomedical field, devices with these characteristics are called soft bioelectronic interfaces. This work is focused more on the devices developed for biomedical applications. However, it is crucial to emphasize how characterization techniques apply to devices regardless of their final application.

First, it is necessary to understand in detail what are the limitations of conventional stiff bioelectronic interfaces and how the development of soft bioelectronic interfaces can overcome these limitations. The main limitations are largely due to the mismatches in the mechanical properties and in chemical compositions between soft biological tissues and conventional rigid electronics. In **Figure 1.1** the orders of

magnitudes of the elastic moduli of the materials involved in bioelectronic interfaces are reported. Typically soft bioelectronic devices have to be designed for long-term applications, so they must adapt to the mechanical strains exerted by the surrounding tissue while maintaining good coupling with the tissue for recording and stimulation.[12–16] Usually Young's modulus of biological tissues varies between 100 Pa and 10 kPa.[17] In contrast, stiff bioelectronic devices exhibit elastic moduli on the order of tens of GPa, for rigid silicon-based chips. Rigid bioelectronics cannot make conformal contact either with soft and curvilinear skin or tissue, and such incomplete contact lowers bioelectronic performance leading to high impedance and low signal-to-noise ratio.[18,19] Moreover, the mechanical mismatch between the wearable or implantable device and the target tissues can cause tissue damage and lead to device failure. For stiff and flat wearable devices, the device cannot follow the contour of soft and curvilinear skin, resulting in concentrated pressure in a localized area. Friction between the device and the skin may result in skin rashes and allergic reactions.[20,21] Stiff implantable bioelectronics may trigger foreign body responses either during insertion or after implantation, as the natural micromotion of the tissue and external mechanical stresses can move the implant.[7,22] Such stress can lead to inflammatory reactions that replace normal tissues near the device with scar tissue, encapsulating the implant. Accordingly, this thick, fibrous scar tissue leads to increased electrical impedance, reduced recording performance, and more mechanical and chemical stress on the electrodes.[23,24] In addition, it is crucial to study the impact that mechanical stresses and differences in chemical composition between the device and its target tissue have on the biocompatibility and performance of the bioelectronic interfaces. In fact, unlike conventional wearable and implantable bioelectronics that consist of metal and/or inorganic materials, biological tissues are hydrophilic, ion rich, and fluidic. The long-term biocompatibility and the performance of bioelectronics can be affected by this difference in chemical compositions,[25] as enzymes, radicals, and reactive oxygen species gradually degrade bioelectronics materials, including the insulating encapsulation layers, eventually leading to device failure.[26] In addition, undesired biochemical reactions, such as

water electrolysis or radical formation can be triggered either by the impedance increase or the leakage of current from the degraded material. [27]

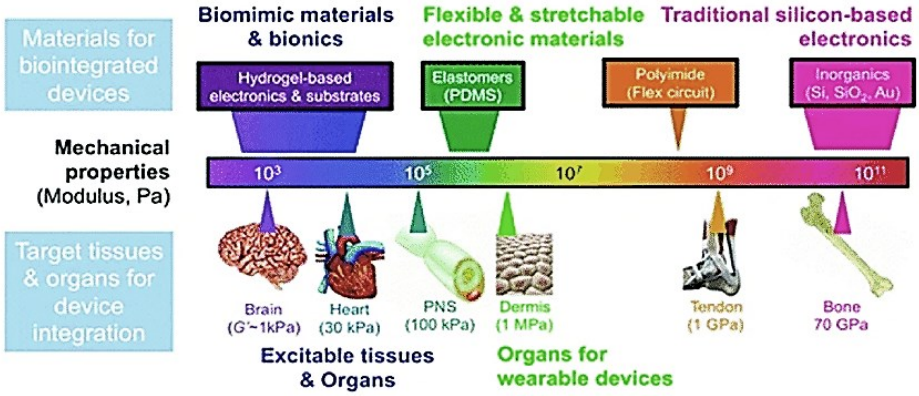

Figure 1.1. Elastic moduli of target tissues, organs, and materials involved in bioelectronic interfaces. The figure is adapted from [185].

1.1 STATE OF THE ART OF SOFT BIOELECTRONIC INTERFACES

Soft bioelectronic interfaces can be divided into two different sets depending on the point of application of the device. If its operation involves only external skin contact, the device is called a wearable sensor, while if a surgical operation is needed to place the electrode, the device is called implantable. The skin is a dynamic and complex organ, which provides a wide range of physiological signals that reflect the overall health and fitness conditions. Three primary types of physiological information, including physical, electrical, and chemical signals, can be measured by wearable sensors.[28–30] Similarly, biosensing devices implanted in the human body monitor the condition of internal body from all physical, electrical, and chemical aspects. [31,32] Nevertheless, the most important aspect of implantable devices lies in neural signal recording and modulation via directly interfacing the nerve with invasive electrodes. Bidirectional communication between nerves and foreign electronics is established by directly interfacing conductive electrodes with neural tissues or cells. On one hand, the non-invasive nature of wearable devices to form bioelectronic interfaces is their main advantage over implantable devices that require surgical procedures to form tissue-device interfaces. On the other hand, implantable devices can collect signals more locally and with reduced noise as the skin is bypassed. Moreover, implantable devices allow for reaching a high spatial resolution, as typically they have three-dimensional pillar-like structures (e.g. Michigan array, UTAH array, 3D Microelectrode Arrays) that can probe the tissue at different depths. In this section, the different types of soft bioelectronic interfaces and the different signals (physical, electrical, and chemical) of the human body that can be monitored with them are described. Typical physical signals to be monitored are strain, pressure, and temperature. Electrophysiological signals are generated by changes in the membrane potential of individual cells, such as activated neurons and muscle cells. Chemical signals are typically related to the concentrations of specific biochemical markers such as pH, ions, glucose, and lactate. In the following, a wearable device case and an implantable device case are described for each type of signal that can be recorded by soft bioelectronic interfaces.

1.1.1 Physical biosensors

Physical biosensors provide a promising way for human physiological signals monitoring, disease diagnosis, and health assessment. Physical biosensors are mainly to detect physical signals such as skin temperature, movement of the body or organs, and other physical phenomena caused by organs in people's daily life. [2,32] Typical physical signals to be monitored are strain, pressure, and temperature. A majority of physical biosensors being investigated are strain or pressure sensors, which are vital to body part motion monitoring, [33,34] heart rate, and blood pressure recording. [35–38] Strain and pressure sensors are typically two terminal devices that measure electrical changes induced by mechanical deformations.[39,40] Several sensing mechanisms have been exploited to measure body motion-induced electrical changes, such as piezoresistive change,[41–43] piezoelectrical change,[44–47] capacitance change.[48,49] For example, *Zhang et al.* developed a wearable highly flexible, stretchable, and sensitive strain sensor by designing a special nanostructure using one-dimensional (1D) nanomaterial (carbon nanotubes (CNTs)), zero-dimensional nanomaterial (Ag nanoparticles (NPs)) and a poly(dimethylsiloxane) substrate (PDMS).[50] The working principle of the strain sensor is sensing the resistance changes due to the device's deformation. The performances of the sensor are found to be dependent on the Ag NPs concentration. Macroscopic and microscopic images of the wearable strain sensors are reported in **Figure 1.2a** and **Figure 1.2b**, respectively. An example of an implantable physical sensor has been reported by *Ruhhammer et al.* [51] Specifically, they designed an implantable magnetic sensor that is applied and fixed to arterial vessels without any blood vessel constriction to measure blood pressure. By calibrating the sensor, a long-term monitoring system for continuously measuring blood pressure is obtained. Two flexible polyimide substrates are fixed by highly deformable and soft silicone strips on opposite sides of an artery. The two substrates are equipped with a Hall sensor and a permanent magnet, respectively. When the diameter of the blood vessel varies, the distance between the Hall sensor and magnet changes leading to an alteration of the output voltage of the Hall sensor. The sensor measures the absolute value of the diameter of the blood vessel. Once the diameter is known, the blood pressure is calculated. **Figure 1.2c** shows a scheme of the implantable pressure sensor.

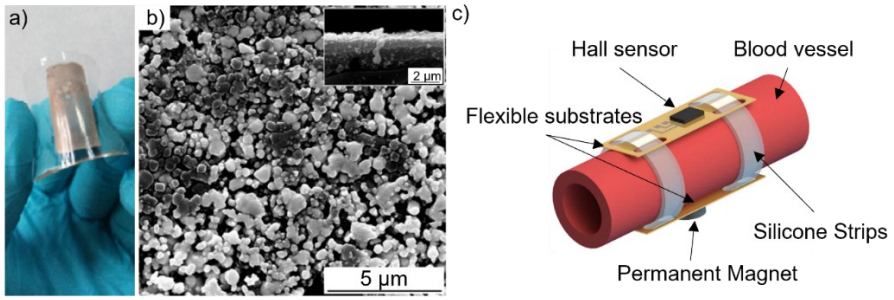

Figure 1.2. Physical Sensors: a) wearable strain sensor as it looks at the macroscopic scale. The image is adapted from [50]. b) SEM image of the strain sensor to investigate the Ag nanoparticles distribution. The inset shows the cross-section of the wearable device. The image is adapted from [50]. c) Scheme of implantable sensors for blood pressure measurements, reported in [51].

1.1.2 Electrical biosensors

Electrophysiological signals represent another class of measurable physiological information. Activated neurons and muscle cells generate action potentials across the membranes, which ultimately result in electrophysiological signals.[52] Wearable electrical biosensors detect tissue-scale potentials that reach the skin surface, which are the summation of the cell's action potential. The signals are then captured by high-resolution electrogram methods, such as electrocardiography (ECG), electromyography (EMG), and electroencephalography (EEG) in a non-invasive manner.[2] For example, *Dong et al.* developed a stretchable bio-potential electrode with a second-order self-similar serpentine structure to continuous, long-term, stable ECG signal recordings which can accommodate larger deformation. Being soft and stretchable, the electrode can establish contact along a wide area adapting to the skin surface.[53] The wearable sensor is designed as a stretchable substrate (PDMS) on top of which a gold serpentine with a specific geometry is placed. The electrode is shown in **Figure *1.3*a**.

Implantable electrode-based neural interfaces have been developed to monitor and stimulate either the central nervous system,[54] or the peripheral nervous system.[55] Being invasive, implantable electrodes not only can detect the tissue-scale potential but also the action potential of a single cell. Electrophysiological recording and

stimulation in both the central and peripheral nervous systems are crucial for the diagnostics and therapy of neural diseases. Electrocorticogram (ECoG) is an invasive alternative to EEG which monitors superficial local field potentials.[54] Compared to EEG, ECoG exploits implanted epidural/subdural multielectrode arrays to eliminate noise from sources between the dura and scalp, and hereby enhance the signal-to-noise ratio. For example, *Chang et al*. present a minimally invasive neural interface for distributed wireless electrocorticogram (ECoG) recording systems.[56] The proposed interface equips all necessary components for ECoG recording, such as high-performance front-end integrated circuits, a fabricated flexible microelectrode array, and wireless communication inside a miniaturized custom-made platform (**Figure *1.3*b**). A thin and flexible microelectrode array is designed and fabricated to be placed on top of the epidural layer in the brain. The electrodes of the device are made of Parylene C and Pt and there are 16 recording electrodes in addition to 4 reference electrodes and one large local ground electrode. The recording electrodes are exposed through the bottom surface of the device to be in contact with the dura mater, while the reference and the ground electrodes are exposed on the top surface to be in contact with the surrounding average potential.

Recently, electrical sensors aiming at single entity recordings in the brain have been proposed. For example, *Schuhmann et al*. reported a microfabrication method to develop syringe-injectable mesh electronics.[57] Following the implantation of flexible mesh electronics via syringe injection, the mesh probes enables stable tracking of individual neurons. A scheme of the device and the syringe is shown in **Figure *1.3*c**. *Khodagholy et al*. designed a different approach to record from a single neuron.[58] The planar electrode is based on PEDOT:PSS, Parylene C, Pt and Au. Their method is based on a conformable neural interface array that can record both local field potentials and action potentials from superficial cortical neurons without penetrating the brain surface. **Figure *1.3*d** shows the electrode structure and its location on the brain to record. Similarly, *Tybrandt et al.* developed a stretchable electrode array based on PDMS and a composite of gold-coated titanium dioxide nanowires (**Figure *1.3*e**).[59] The developed grid can resolve high spatiotemporal neural signals from the surface of the cortex in freely moving rats with stable neural recording quality and preserved electrode signal coherence during 3 months of implantation.

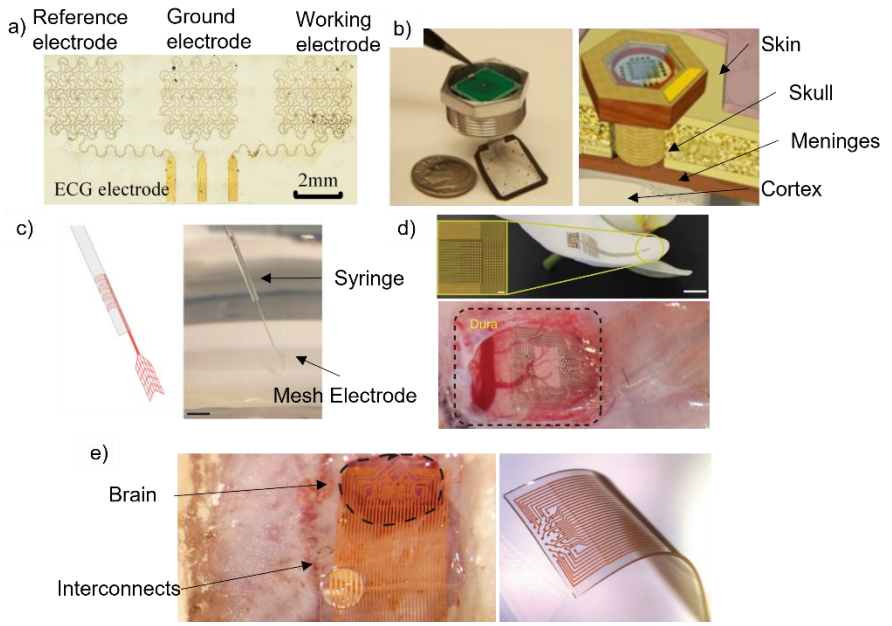

Figure 1.3. Electrical Sensors: a) wearable sensor for ECG recording as it looks at the macroscopic scale. The image is adapted from [53]. b) The implantable sensor for ECoG recording is shown on the left. On the right, a scheme of the sensor implanted into the brain is depicted. The images are adapted from [56]. c) Syringe injectable mesh electronics for single neuron recording. The images are adapted from [57]. d) Planar PEDOT:PSS - based electrode array implanted in the cortex. The images are adapted from [58]. Stretchable electrode array based on PDMS and conductive nanowires for single neuron monitoring. The images are adapted from [59].

1.1.3 Chemical biosensors

Conventional approaches to detect biochemical markers such as pH, ions, glucose, and lactate require extracting a small volume of blood via a syringe needle. However, sampling blood with the needle involves pain and infection risk. Moreover, real-time monitoring of biochemical markers is desired for obtaining comprehensive information about the wearer's health, performance, or stress at the molecular level. [32,60] Non-invasive (wearable) access to biochemical markers is only possible by measuring biofluids secreted by the body, such as saliva, sweat, and tears. The skin behaves as an almost perfect barrier to most chemicals. For example, *Shu et al.* reported a non-invasive fiber material-based wearable electrochemical sensor to

continuously monitor the glucose level in sweat.[61] The working electrode (Ni–Co MOF/Ag/rGO/PU fiber), the reference electrode (Ag/AgCl fiber), and the Pt wire counter electrode were sutured with absorbent fabric and fixed on a stretchable PDMS substrate to form a wearable nonenzymatic sweat glucose sensor, which can be used to continuously monitor the glucose level in sweat. The working electrode structure and the glucose sensor are shown in **Figure 1.4a.** In the case of implantable chemical devices, the skin is bypassed, therefore no barriers separate the target biomarkers from the sensors. The invasiveness not only increases the efficiency of the signals recording but also allows the use of implantable devices as local and long-term drug delivery systems.[62] For example, *Kim et al.* propose an electromagnetic-based sensor that can be subcutaneously implanted and capable of tracking minute changes in dielectric permittivity owing to changes in blood glucose level.[63] The operating principle is that the dielectric permittivity of blood changes as the glucose level changes. These glucose-dependent permittivity changes are reflected in the sensor resonance frequency. Using a regression model, sensor frequency can be mapped to blood glucose levels. A scheme of the implantable sensor and its operative location site are reported in **Figure 1.4b**. It must be highlighted that at the moment, even though several implantable chemical sensors have been developed, only few succeeded clinical trials.

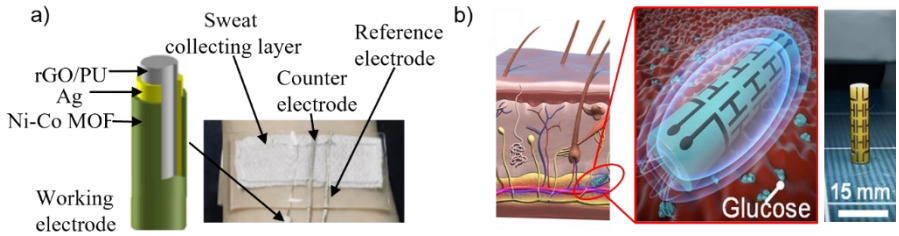

Figure 1.4. Chemical Sensors: a) On the left the scheme of the working electrode is shown. The figure on the right shows the glucose sensor integrated into the elastic fabric. Both images are adapted from [61]. b) The first image on the left shows an EM-based subcutaneous implant glucose sensor allocated under the skin. The inset zooms into the implantable sensor. The image on the right shows how the sensor looks after the microfabrication. Both images are adapted from [63].

With the development of new functional materials and specific geometries for soft bioelectronic interfaces, the need to characterize the mechanical properties of these devices and their individual components increases. Contemporary to the experimental characterization tests, it is also necessary to develop interpretative models and numerical simulations able to describe the mechanical behavior of the device. Only in this way it will be possible to develop optimal materials and designs for the performance required by the specific application of the implantable or wearable device. In the next section, first *in situ* mechanical characterization techniques of flexible/stretchable devices and their individual components such as nanowires, nanofiber, nanopillars, and ultra-thin films are reported. It is necessary to specify that in this context *in situ* means that the mechanical characterization takes place during deformation.

1.2 STATE OF THE ART OF *IN SITU* LOCAL CHARACTERIZATION OF SOFT BIOELECTRONIC INTERFACES

Although flexible and stretchable soft bioelectronic interfaces have achieved a great breakthrough compared to their traditional rigid counterpart, several mechanical aspects must still be investigated and optimized. First, while the goal is to obtain a device that is as soft as possible to overcome the mechanical mismatch between electrode and tissue, the device must also be handled and inserted without being damaged. Second, it has been reported that modifying the surface with coatings and three-dimensional nanostructures or microcracks, might improve the performance of the device in terms of mechanical failure, coupling between electrode and tissue, adhesion, and biocompatibility.[64–67] However, a rational and comprehensive understanding of these mechanisms has not yet been found and therefore this precludes effective optimization of device performance to date. Third, the mechanical characterization of these devices is typically done macroscopically, that is, the mechanical performance of the whole device rather than either the local properties or individual micro/nano components are tested.[68,69] Although macroscopic characterizations are fundamental to investigating the properties of a device, microscopic and local aspects of the device can also significantly determine its properties. The phenomena that lead to device failures such as delamination, the formation of overly wide microcracks, or damage to the encapsulation layer, all occur locally, even though they have global effects on device performance. A microscopic mechanical characterization is necessary because these devices are extremely small. In addition, the devices must interface with heterogeneous body parts. This makes a local investigation of the mechanical properties of the soft bioelectronic interface crucial to establish good coupling with heterogeneous biological tissue. Therefore, the mechanical characterization must also occur locally. Furthermore, mechanical characterization of a device developed to operate under strain should also take place while the device is deformed, and not just compare device properties before and after deformation. Only an *in situ* characterization might give clear insights into the nanoscale mechanisms activated by deformation that led to device failure.

Fourth, to extract quantitative parameters describing the mechanical response of the device, predictive models are needed. Therefore, the development of new experimental techniques for nanoscale characterization is closely related to the development of models to interpret the results. In this context, analytical and numerical (FEM) models based on continuum mechanics allow comparison of the material constitutive parameters estimated at the nanoscale with the corresponding macroscale values (i.e. those used in continuum mechanics). This type of comparison is critical and can reveal the need to introduce corrective factors into continuum mechanics-based models to take into account effects typical of the nanoscale.[70] Therefore, optimization of the performance of these devices, can only occur through the design of specific experimental setups for local *in situ* mechanical characterizations that, supported by predictive models, allow a greater understanding of the local working mechanisms of these functional materials and stretchable/flexible device components. Only a deeper understanding of these mechanical aspects will pave the way to an optimized design of wearable and implantable soft bioelectronics initiating a new era of health monitoring, diagnosis, and therapeutic. In this section, the first attempts of *in situ* local mechanical characterization and modeling of flexible/stretchable devices and their individual components such as nanowires, nanofiber, nanopillars, and ultra-thin films are reported.

In situ local micromechanical testing of individual components and local properties of devices introduces three practical challenges: (i) observation of the sample at the nanoscale, (ii) nanomanipulation of the sample so that a mechanical test can be performed, and (iii) accurate recording of the applied force and deformation during mechanical testing. Conventional universal material testing machines are typically able to test devices that can be manipulated by hand and do not require direct observations at the microscale.[64] On the contrary, the relatively small size of the individual component cannot be observed without the aid of a microscope. In addition, a greater manipulation precision and force resolution than provided by conventional methodologies is required. Initial attempts of *in situ* local micromechanical testing used various microscale imaging techniques such as Scanning Electron Microscopy (SEM), Transmission Electron Microscopy (TEM),

Confocal Laser Scanning Microscopy (CLSM), and Atomic Force Microscopy (AFM). The instrument to perform the mechanical test is placed inside the chamber of the imaging tool to observe the samples during the acquisitions. Recently, specific instruments, such as microelectromechanical systems (MEMS) or AFM cantilevers, have been developed, depending on the sample under investigation. In the following, the experimental techniques for micromechanical characterization are reported. In particular, the experimental approaches are divided depending on the type of mechanical test: tensile test, bending test, nanoindentation test, and micropillar compression test.

1.2.1 Tensile test

In materials science, the tensile test is a materials characterization test that consists in subjecting a specimen of well-defined size and shape (typically dog-bone shape) of a material under test to an initially zero uniaxial load that is increased to a maximum value that eventually results in material failure. The tensile test is used to determine several characteristics of the material under test, including ultimate strength, Young's modulus, and yield strength. In recent years, researchers have been trying to reproduce tensile tests at the nanoscale with different experimental setups. Along with the development of the experimental setups, it is crucial to find models to interpret and generalize the findings. Typically, samples of different materials are used as prototypes to test the experimental techniques. For example, *Zhu et al.* developed a material testing system for *in situ* electron microscopy mechanical testing of nanostructures.[65] The testing system consists of a microelectromechanical system (MEMS) that includes an actuator (electromechanical or thermomechanical) and a load sensor based on capacitance measurement. To observe the specimen during the uniaxial tensile test, they used either a SEM or a TEM and monitor two displacement markers during the acquisition (**Figure 1.5a**). To test their experimental setup, they investigated different free-standing nanostructures, such as carbon nanotubes, palladium nanowires, and polysilicon films, acquiring the stress-strain curves. Similarly, *Thomas et al.* designed an experimental setup to investigate the plastic deformation process of semi-crystalline polymers capturing images from the same locus of the sample as a function of strain. [66] The strain is applied and monitored with a motorized stretching stage which is placed under the AFM probe to capture

images of the sample. In particular, they studied the initiation, growth, and coalescence of crazes in poly(1-butene) at different strain values. **Figure 1.5b** shows the samples under SEM with 10% strain. Their findings show the presence of crazes oblique with respect to the principal tensile stress. A different use of AFM, not as an imaging tool but as a mechanical tester, was employed by *Hang et al.* in studying the mechanical properties of nanofibers.[64] The mechanical testing of individual nanofibers was carried out in a chamber of an SEM incorporating an AFM system. A custom-built AFM system with the sample stage rotated at 90° with respect to a conventional AFM system was used to allow access to the SEM electron beam. Fine manipulation is provided by the movement of the AFM probe attached to the cantilever using the piezoscanner connected to the AFM head. The nanofiber under investigation was glued on both sides, one to a substrate and one to the AFM tip. A scheme of the experimental setup as well as a glued nanofiber to the AFM tip before the acquisition are shown in **Figure 1.5c**. The nanofibers were tested by applying a uniaxial tensile load moving the AFM tip. Force spectroscopy showed increased tensile strength and elastic modulus when compared to bulk equivalents. In the case where nanofibers are embedded in a polymer matrix, *Cao et al.* proposed *in situ* tensile testing by exploiting the ability of TEM to obtain not only surface information of the sample.[67] Specifically, they considered graphene hybrid films with Ag nanowires. The sample and the experimental setup can be seen in **Figure 1.5d**. Their findings highlight a softening of the hybrid films compared to a single graphene film.

So far, tensile test experiments that reach the sample failure within a single acquisition have been reported. Nevertheless, it is also crucial to investigate the material behavior at the nanoscale under cyclic load, i.e. under multiple usages. This is the case of the fatigue test, which consists in the application of a cyclic load to the sample, keeping the maximum load in the elastic regime. These tests are used either to generate fatigue life and crack growth data, identify critical locations or demonstrate the safety of a structure that may be susceptible to fatigue. For example, *Cattarinuzzi et al.* investigated the failure mechanism of aluminum/polyimide stretchable interconnects under cyclic load with a uniaxial stress test with *in situ* SEM or CLSM.[68] Their work highlights the crucial role played by the interface between the substrate and the metal serpentine in defining the mechanical properties of the

stretchable interconnects. When stretching the substrate, the stresses experienced by the interconnect metal core are relieved by the deformation of the meandering structure, which undergoes in-plane and out-plane distortions, as shown in **Figure 1.5e**. In addition, the restraint offered by the underlying compliant substrate contributes to retard ductile failure of the metal film. In subsequent work, *Kleinendorst et al.* used the same experimental setup with CLSM to extract height profiles of metal serpentines on polyimide.[69] Using a digital height correlation algorithm, they recorded the three-dimensional microscopic deformation both in-plane and out-of-plane. They then compared the experimental results with numerical simulations to model and describe the behavior of the interface during the experiment. The comparison between experiments and simulations suggests that only considering residual stresses and different properties in shear and normal directions allows a comprehensive description of the delamination mechanism. A simulation result and a CLSM image are compared in **Figure 1.5f**.

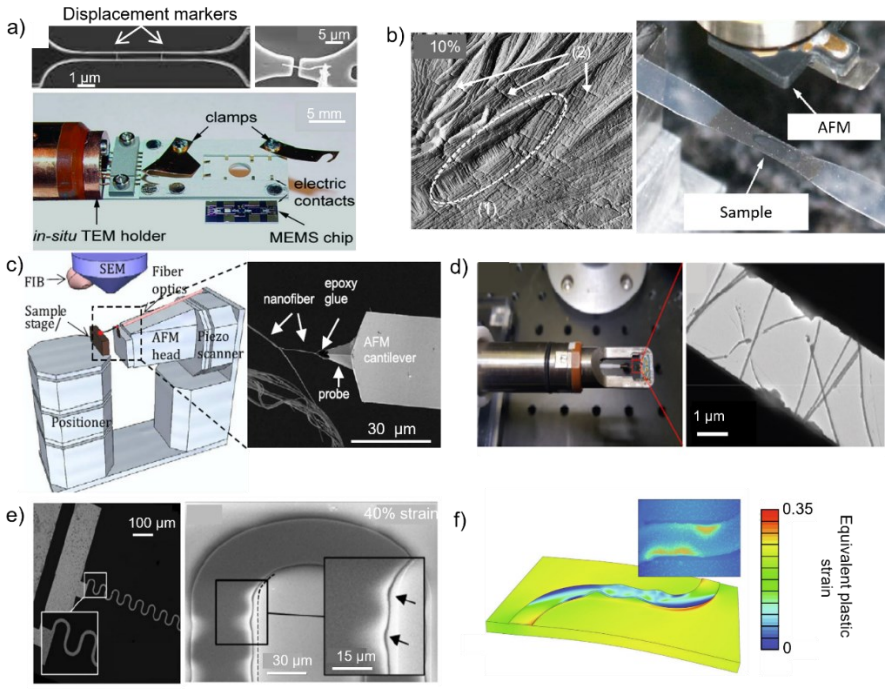

Figure 1.5. Tensile test. a) *In situ* TEM holder along with a 5x10 mm MEMS chip. In an actual experiment, the MEMS chip is flipped, placed in the TEM holder, and fixed by the left and right clamps. The two SEM images on top show the working configuration of both a thin film and a nanowire. The images are adapted from [65]. b) On the left the AFM image of the diagonal region of spherulite at 10% strain is shown. The label (1) indicates craze nucleated at the boundary of stacks with different lamella orientations, while (2) labels the lamella fragmentation within a lamella stack. The images are adapted from [66]. c) AFM-in-SEM configuration for *in situ* nanofiber tensile test. The image on the right shows the glued nanofiber attached to the AFM probe before the acquisition. The figures are adapted form [64]. d) *in situ* TEM tensile testing platform of Ag NW/graphene hybrid film sample. The images are adapted from [67]. e) Image of the aluminum serpentine on a polyimide substrate. On the right, the delamination of the metal serpentine at 40% strain is shown. The images are adapted from [68]. f) FEM results with the mixed-mode cohesive zone model. For comparison, the insets show the topographic height profile measurements from the experiments at the same global stretch increment. The figures are adapted from [69].

1.2.2 Bending test

In bending tests, specimens characterized by a geometry for which one (two) dimension(s) are greater than the other two (one) are considered, so that a longitudinal axis (middle plane) can be identified. These specimens are loaded perpendicularly to the longitudinal axis/middle plane. Typically, samples, such as nanowires, nanofiber, or nanopillar, can be modeled as a beam, while planar specimens are usually modeled as plates. Therefore, depending on the geometry of the specimen, different interpretative models are used and allow to investigate different aspects of its mechanical behavior, such as the bending stiffness, the maximum deflection, and the failure stress. For example, *Kim et al.* investigated the nanomechanical properties of Silicon nanowires with a radius between 15 and 70 nm by means of AFM bending on freestanding samples.[71] In this case, the nanowires were clamped on both ends, as shown in **Figure 1.6a**. In order to find out what analytical model adapts better to the experimental data, they performed systematic investigations of the testing configurations through finite element simulations. In particular, their results highlight that under a certain threshold of radius the mechanical properties show significant size dependency since the nanowire strength dramatically increases as the radius is reduced. Similarly, *Morel et al.* investigated the micromechanical properties of poly(L-lactide) nanofibers of different diameters with AFM bending.[72] Young's moduli show a strong increase for thinner fibers below a critical diameter of 800 nm. To apply the load at the center of the nanofiber, a hook was used. The experimental setup and the sample during the acquisition can be found in **Figure 1.6b.** *Antsov et al.* used AFM to measure the elastic modulus of five-fold twinned gold nanowires and compare three different sample configurations to perform the acquisitions.[73] Specifically, they tested the following configurations: three-point bending with fixed ends, three points bending with free ends, and cantilevered-beam bending. The configurations are depicted in **Figure 1.6c.** In addition, all three configurations were simulated with a finite element method to obtain better insight into stress distribution inside NWs during bending depending on test conditions. An experimental approach to characterize micromechanical properties of nanopillar in vertical rather than freestanding configuration has been recently proposed by *Angeloni et al*.[74] They proposed two atomic force microscopy

methods, based on contact mode imaging and force spectroscopy imaging, to determine the mechanical characteristics of individual micro- and nanopillars as fabricated, without using SEM. **Figure 1.6d** shows the samples as well as the working principle of both techniques. The technique has been tested either on polymeric nanopillars or electron beam-induced deposited nanopillars. With the proposed technique, authors were able to estimate the stiffness of the nanopillars, as well as the maximum lateral force, the maximum deflection, and the failure stress. *Abrahamians et al*. developed an experimental setup to perform *in situ* stiffness measurements on ultrathin membranes.[75] Specifically, the stiffness of suspended Indium Phosphite (InP) membranes was locally measured by contact at several points of their surface, using a self-sensing quartz tuning fork probe controlled in frequency modulation. Experiments were conducted *in situ* through the robotic nanomanipulation system implemented in a SEM. A scheme of the experimental setup is shown in **Figure 1.6e**.

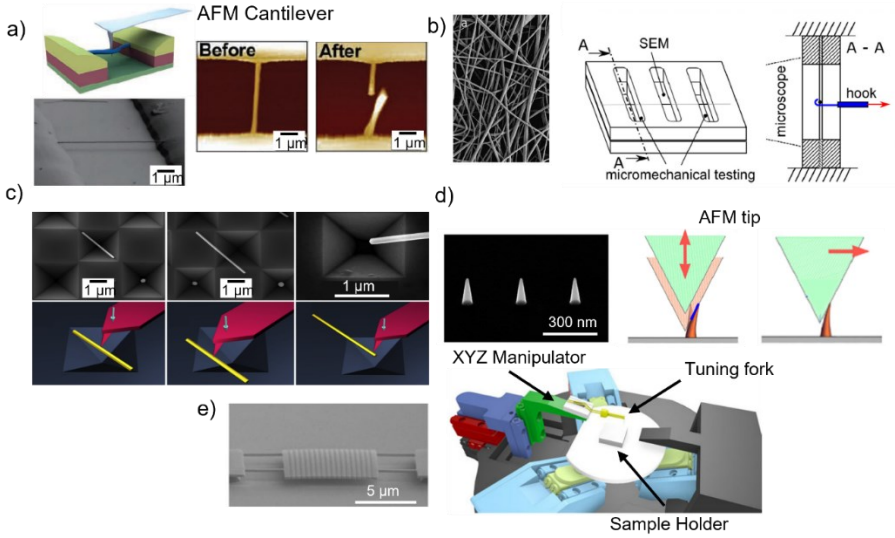

Figure 1.6. Bending test. a) SEM images of fabricated structures and AFM bending configuration. AFM images before and after the bending are reported on the right. The figure is adapted from [71]. b) On the left the electrospun nanofibers are shown. On the right, the micromechanical testing setup is reported. The hook used to apply the load to the fibers is drawn in blue. The images are adapted from [72]. c) SEM images and corresponding schematics of Au NWs in three different configurations: free-ends (left), fixed-ends (center), and cantilevered (right). The images are adapted from [73]. d) SEM image of the nanopillars under investigation. On the right, the force spectroscopy imaging approach and the contact mode imaging method are shown, respectively. The images are adapted form [74]. e) Ultra-thin membrane under investigation and a scheme of the experimental setup with the tuning fork to measure the resonance frequencies. The figure is adapted from [75].

1.2.3 Nanoindentation test

Nanoindentation is an efficient method to study the mechanical properties of materials at a small scale with minimal sample preparation. The technique is ideal for the study of thin films or small volumes of material located in the proximity of the surface. In a typical nanoindentation test, force and displacement are recorded when an indenter is pressed against the surface of the material being measured, with defined loading and unloading profiles. Nanoindentation is most often used to measure hardness and elastic modulus, but significant advances have also been made in measuring other mechanical parameters such as hardening exponents, creep parameters, and residual stresses.[76] Traditionally, *ex-situ* nanoindentation is a common method for determining the hardness and modulus of elasticity of materials, and quantitative stress-strain curves can be obtained. Discontinuities in the stress-strain curve are associated with specific phenomena in the material. Typically, such phenomena take place during the test while the deformation is applied. Therefore, *ex-situ* nanoindentation tests might not be suitable to investigate the causes that determine the deformation mechanism. The combination of nanomechanical testing and direct observation provides unique insights into the material's behavior, including crack initiation, crack extension, delamination, stacking, elastic, and plastic deformation. For example, *Guillonneau et al.* developed an experimental method to determine the true projected contact area during indentation testing.[77] In particular, the experimental setup is composed of a microindenter placed inside a SEM. They investigated the pile-up and sink-in effect during the nanoindentation of different thin films such as nanocrystalline nickel, ultrafine-grained aluminum, and fused silica. **Figure 1.7a** shows the contact area after the nanoindentation experiment. The indentation testing process is continuously observed in the SEM to monitor the surface deformation around the tip. Their findings highlight that the hardness/elastic modulus ratio define a threshold to what contact mechanics model is appropriate to describe the nanoindentation model. Using a similar setup, *Lewis et al.* designed a method able to microfabricate the sample first and characterized them with the same instrumentation.[78] Exploiting the focused ion beam-induced deposition, they were able to microfabricate platinum-carbon 3D nanoscale architectures. The nanomechanical tests were performed using a nanoindentation system inside the

same SEM for simultaneous *in situ* imaging. The real-time imaging during the sample deformation, allowed them to record a viscoelastic response of the material under investigation. **Figure 1.7b** shows a platinum-carbon 3D architecture before and after the nanoindentation on top. Recently, an AFM-in-SEM setup has been proposed by *Novotna et al.*[79] Such a setup allows the exploitation of the imaging capabilities of the two techniques, while an indenter performs the mechanical testing. This hybrid technique enables sample phase identification, precise indentation targeting, and topographical analysis all in one measurement, as shown in **Figure 1.7c**.

1.2.4 Micropillar compression test

Similar to the nanoindentation test is the micropillar compression test. During a micropillar compression test, a rigid indenter is placed inside a SEM. To apply this characterization technique the samples must have a pillar-like structure, which is typically achieved with a focused ion beam. Differently, from nanoindentation, compression testing is usually performed using a flat punch indenter which has a slightly larger diameter than the micropillar itself. Therefore, the compression technique is less sensitive to the indenter geometry. The samples for the compression test provide a small volume of material with a very defined geometry (commonly cylindrical or square). *In situ* SEM micropillar compression tests provide a way to measure the uniaxial mechanical response of low volumes of materials and to directly correlate the stress-strain data to individual deformation events. It enables quantifying specific phases and particles or to study deformation behavior and strengthening mechanisms. For example, *Jun et al.* reported a study of local deformation mechanisms in two-phase Ti alloys.[80] Specifically, they performed micropillar compression tests using a displacement-controlled nanoindenter set inside a SEM, with a constant displacement rate. The results show that the two phases' morphology significantly affects the local deformation behavior. Snapshots extracted from the time step evolution of the compression test can be seen in **Figure 1.7d.**

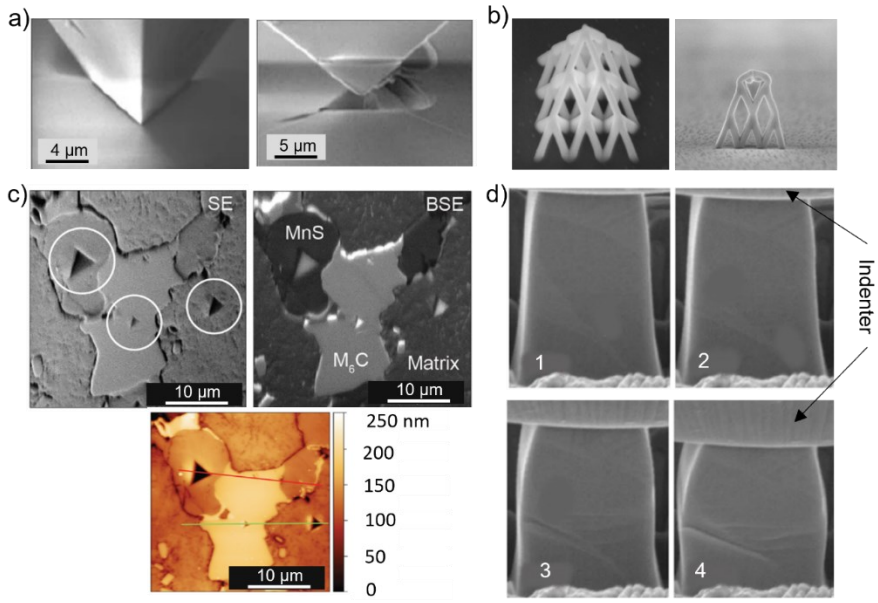

Figure 1.7. Nanoindentation and Micropillar compression tests. a) the indentation at maximum load and the indentation after unloading, showing the trace left by the material on the tip, and used to determine the sink-in. The figure is adapted from [77]. b) Pyramidal structure before (image is at a 30° tilt) and after (taken at an 89° angle relative to the electron beam) compression. The scale bars are 200 nm. The images are adapted from [78]. c) SEM image obtained with secondary electrons (SE) with circles highlighting individual indents and SEM image obtained with backscattered electrons (BSE) indicating the material composition. On the bottom, the AFM image of the same region of the sample is shown. The AFM image allows the extraction of the profiles of the nanoindentation imprint into the sample. The images are adapted from [79]. d)Time step evolution of the micropillar compression test. The figure is adapted from [80].

1.3 MY RESEARCH PROJECT

As described in the previous section, experimental techniques for testing mechanical properties *in situ* at the nanoscale are emerging nowadays. However, the reported techniques often rely on custom components specifically designed for the sample under investigation. Moreover, these techniques often involve the combined use of two or more instruments, thus being expensive and difficult to reproduce in other laboratories with other experimental setups. Thus, experimental techniques are needed that are easy to access and require as little sample handling as possible. Among the various imaging and mechanical testing tools, AFM appears to be among the most promising to overcome these limitations. The atomic force microscope can test nonconductive samples, unlike SEM and TEM which require at least a conductive coating. In addition, AFM can operate in room temperature conditions without the need for a vacuum. The absence of vacuum among the requirements for micromechanical testing also simplifies sample nanomanipulation during experiments. As much as the AFM looks very promising, it also has some limitations that can affect its suitability for certain applications. Its scanning process is slow compared to other imaging tools, which limits its throughput and makes it less suitable for high-speed imaging. While it provides high-resolution topographic information about the sample, it does not provide detailed chemical information. Finally, AFM probes are delicate and can wear out over time, which can result in reduced image quality, presence of artifacts or even probe failure. As reported in the previous section, to describe and interpret the experimental data, predictive models and numerical simulations need to be added to the laboratory tests. It is necessary to make use of interpretive models that allow a greater understanding of the local working mechanisms of these functional materials and stretchable/flexible device components, paving the way to the investigation and optimization of the performance of soft bioelectronics interfaces.

In this context, my doctoral research activity regarding the nanomechanical characterization of soft bioelectronic interfaces took place. The research project synergistically adopted two different and complementary approaches to develop experimental setups and interpretive models for nanomechanical characterization: (i) numerical modeling of the sample under investigation; (ii) experimental analyses to

provide direct inputs to simulations and to evaluate the result. The skills and instrumentation needed to perform the activities described in (ii) are available at the Department of Physics, University of Bologna, while the skills and software tools needed for (i) are available at the Laboratory of Computational Mechanics (LAMC), located at DICAM. The AFM used in this work is the NX10 model, manufactured by Park System. Specifications of the instrument can be found here.[81] For a detailed description of the operating mechanism of an atomic force microscope, the reader is referred to textbook.[82] In what follows are reported, one by one, the papers published during my Ph.D. program.

Chapter 2 is based on the first paper published during my Ph. D and describes an experimental method to study the mechanical response of an ultra-thin metal film deposited on the polymeric elastomer. This type of material is a prototype stretchable conductor employed in wearable and implantable soft bioelectronics. In this first work, nanoindentation experiments and electrical measurements were carried out with AFM to characterize the nanomechanics of ultrathin gold films on polydimethylsiloxane (PDMS) elastomer. The method, along with an analytical method, enables quantifying the local Young's modulus of elasticity of the nanometer-thick film. By investigating the effect of different film thicknesses, a threshold value for the percolation of the thin metallic film is revealed. Only if the thickness of the metallic film is greater than the threshold a linear increase in bending stiffness and electrical conductivity is recorded.

Chapter 3 contains the second work done during my Ph.D. In this work, a novel atomic force microscopy (AFM) method is demonstrated, which provides multichannel images of surface morphology, conductivity, and elastic modulus *in situ* during sample deformation. The experimental approach has been tested by investigating strain effects in thin gold films deposited on a soft silicone substrate. The findings show the effect of microcrack opening during tensile strain and their impact on local current transport. The acquisitions reveal that although the films fracture into separate fragments, at higher strain a current transport is sustained by a tunneling mechanism.

In the context of the collaboration with the Department of Electrical and Computer Engineering of the Technical University of Munich (TUM), the nanomechanical response of 3D-printed inkjet micropillars has been investigated. These types of structures constitute microelectrode arrays (MEAs) and are often used in implantable devices as they allow better spatial resolution and have a high signal-to-noise ratio. In the context of this collaboration, samples with different microfabrication techniques were developed in Munich. Afterward, the fabricated samples were nanomechanically characterized with an AFM-based method developed in Bologna to measure the flexural stiffness and elastic modulus of materials. Accurate mechanical characterization of micropillars is pivotal in the fabrication and optimization of MEA, as it determines the mechanical compliance with the tissue and whether the device will fail or not. The results of this research are reported in Chapter 4.

2 ATOMIC FORCE MICROSCOPY NANOMECHANICS OF HARD NANOMETER-THICK FILMS ON SOFT SUBSTRATES: INSIGHTS FOR STRETCHABLE CONDUCTORS

The content of this chapter was published in the journal ACS Applied Nano Materials.

Abstract

The nanomechanical properties of ultrathin and nanostructured films of rigid electronic materials on soft substrates are of crucial relevance to realize materials and devices for stretchable electronics. Of particular interest are bending deformations in buckled nanometer-thick films or patterned networks of rigid materials as they can be exploited to compensate for the missing tensile elasticity. Here, we describe Atomic Force Microscopy (AFM) indentation experiments and electrical measurements to characterize the nanomechanics of ultrathin gold films on polydimethylsiloxane (PDMS) elastomer. The measured force-indentation data can be analyzed in terms of a simple analytical model describing a bending plate on a semi-infinite soft substrate. The resulting method enables to quantify the local Young's modulus of elasticity of the nanometer-thick film. Systematic variation of the gold layer thickness reveals the presence of a diffuse interface between the metal film and the elastomer substrate that does not contribute to the bending stiffness. The effect is associated to gold clusters that penetrate the silicone and are not directly connected to the ultrathin film. Only above a critical layer thickness percolation of the thin metallic film happens, causing linear increase in bending stiffness and electrical conductivity.

2.1 INTRODUCTION

Integration of advanced microelectronic sensor and actuator technology into devices with soft and stretchable mechanical properties is a major challenge for electronic materials science and device engineering.[83,84] Low-invasive biomedical implants,[8,9] soft robotics,[10] or electro-mechanical energy harvesters,[11] all rely on deformable electronic devices that are compliant to a mechanically demanding environment while maintaining their electronic functionality. Unfortunately, most of currently known high-performance electronic materials are based on hard and stiff inorganic conductors and semiconductors. Only recent research demonstrated how structural engineering at the micro- and nanoscale permits to combine such hard materials with soft and elastic substrates resulting in overall stretchable properties.[83] The progress relies on the fact that hard inorganic materials can be bent with small forces, when patterned into ultra-thin layers or nanowires.[85] Such bending deformations can then be exploited to compensate tensile strain during device stretching. Examples of this approach are stretchable serpentine conductor lines,[86] buckled conducting thin films,[87] a kirigami,[88] or island based conducting network structures.[89,90] So far, development and optimization of the stretchable surface patterns has been based on the analogy to their macroscopic counterparts and empirical findings. However, the nanoscale confinement of the thin inorganic layer as well as its adhesion to the elastic substrate can have a critical impact on the mechanical properties, changing the bending as well as fracture behavior. To take such effects into account and to achieve a rational optimization of wavy surface patterns for stretchable electronics, techniques and models are needed to characterize the nanomechanics of ultrathin hard layers on soft substrates.

Atomic force microscopy (AFM) has evolved in the last decade as a powerful tool to study the nanomechanics of complex surface structures. Advances in instrumentation have carried to a versatile tool thanks to highly specified probes to investigate different mechanical properties at the nanoscale. Colloidal AFM probes have been widely used to measure the friction and adhesive surface properties of materials.[91,92] The typical diameter of colloidal probes is in the order of a few µm to avoid penetration and fracture of the material under investigation. In a nanoindentation experiment, instead, the tip must locally penetrate the target surface, therefore sharp

AFM probes have been developed with a diameter in the order of 10nm.[93] The variation in the tip diameter allows operating in different force regimes with the same instrument. Important examples demonstrating the power of these techniques, regard the characterization of nano-phase separated polymers or investigations of the cytoskeleton in living biological cells.[94] Inspired by this success, first research groups have employed the AFM to systematically investigate samples with more complex layered structures.[95] Examples are thin layers on top of a substrate with softer or harder elastic properties, thin bilayers of polymeric materials with differing elastic modulus or multi-layered structures of layer-by-layer microcapsules.[91,96,97] Indentation experiments on bi- or multilayer structures face difficulties as analytical models are needed to extract the materials properties (i.e. elastic moduli, Poisson ratio) and structural information (i.e. layer thicknesses) from the measured force-indentation curves. For the case of homogeneous semi-infinite surfaces with isotropic elasticity, such models based on Hertz, Boussinesq or Sneddon theories are available and are routinely applied in experiments.[94,98–100] Instead for layered systems, no general analytical solution is available for the more complex nanoindentation process and up to now only few approximate or phenomenological models have been introduced. For example, under the assumption that the mechanical properties of the different layers do not differ widely, a perturbative approach has been developed to derive an effective, depth dependent modulus that combines contributions from different layers and substrate.[96,97,101] Other works employ numerical finite element models to understand and quantitatively analyze indentation curves.[102] Many works on bilayers focus on the case of a soft top layer on a hard substrate as this is relevant to indentation studies on living cells where the so-called “bottom effect” introduces artifacts to the quantitative analysis of cell’s elastic properties.[103] Inspiration for the derivation of analytical AFM nanomechanics models comes from classical mechanical engineering works describing stiff, bendable layers on top of an elastic semi-infinite continuum to assess the stability of construction sites on soft soil.[104,105] Advancing on this background, first analytical models have been derived in the literature to describe indentation of hard stiff nanometer-thick layers on soft substrates and open new opportunities to interpret experimental nanoindentation data.[106,107]

Here we introduce Atomic Force Microscopy to investigate the nanomechanics of thin gold-layers deposited on a silicone elastomer substrate. We consider such bilayers a model system for stretchable conductors based on ultrathin bendable metallic layers deposited on a soft substrate. Gold on silicone structures have recently been used to realize stretchable bioelectronic implants with low-invasiveness due to their compliance to the mechanics of the surrounding tissue.[55,108] The gold nanometer-thick film maintains its conductivity during stretching due to the formation of a microcrack pattern when a suitable layer thickness and adhesion promotor (titanium or chromium interlayer) are applied.[109,110] With increasing strain, the non-conducting microcracks exposing the elastomer substrate open and the ultrathin gold layer takes the form of a network structure that compensates the tensile strain by bending deformations without breaking its interconnectivity.[111] Therefore, the microcracked gold-layer can maintain its electrical conductivity yielding a stretchable conductor. Gold layer thickness and adhesion are two fundamental parameters that decide on the performance of the stretchable conductor: too thin layers do not offer sufficient conductivity whereas thick gold layers have a large bending stiffness and create only few but large fractures that interrupt conducting pathways during strain.

In order to understand the crucial role of thickness on the nanomechanics of such thin metallic films on elastic substrates, we introduce in this work indentation experiments combined with electrical characterizations. To interpret the indentation data, we exploit the analytical model provided by Lee,[107] and compare with finite elements simulations. To our knowledge, it is the first time that the analytical model is confirmed experimentally and used to provide quantitative insight from AFM nanoindentation experiments. For the case of ultrathin metal films evaporated on a soft elastomer substrate, our results demonstrate the existence of a critical threshold of a few nanometers of thickness that decides on the mechanical properties. Below the threshold thickness, force-indentation curves show only a smaller increase in surface stiffness and maintain a Hertzian curved shape. Above the threshold, the metal film behaves as a bending plate and shows a linear force indentation curve that becomes independent of the shape of the identing tip. In this regime, the surface mechanics are fully dominated by the flexural rigidity of the metallic ultrathin film

and the elastic modulus of the substrate. By performing measurements on gold layers with different thicknesses, we can relate the bending stiffness to the bulk elastic properties of the thin metallic film. Finally, comparison with the electrical conductivity of the gold-silicone layer shows that the threshold behavior in the indentation nanomechanics matches the onset of surface conductivity. Accordingly, we attribute the observed threshold to the onset of percolation of gold islands growing on the silicon substrate.

2.2 EXPERIMENTAL SECTION/METHODS

2.2.1 PDMS/Au and PDMS/Ti/Au preparation

PDMS is obtained by mixing crosslinker and Sylgard 184 silicone in a ratio of 1:10. After intensive stirring, the mixture is put under vacuum so that the air bubbles are removed. The mixture is then poured onto a microscopy glass slide and spin-coated at 250 rpm for 3 min. Substrates are then stored for one hour at 70 °C in an oven. Then the titanium adhesion layer (1-2 nm thickness) and gold are deposited on the glass/PDMS substrates by thermal evaporation (source sample distance = 25 cm, vacuum pressure = $5.5\ 10^{-6}$ mbar).

2.2.2 AFM characterization

A Park System's NX10 AFM was used in the experiments. The Rocky Mountain Nanotechnology's probe 25Pt300B was used to perform simultaneously conductive AFM and force spectroscopy. For normal indentation experiments we used nonconductive tips such as Mikromash's NSC36B and NCHR from Nanosensors. To study the linear elastic regime, we typically used a setpoint of 400 nN and an indentation speed of 3 $\mu m\, s^{-1}$. The range of Z height scanned is defined to obtain at least 200 nm baseline before the contact between the tip and the sample takes place. Prior to each experiment the tip sensitivity and force constant are calibrated by indentation on a silicon surface and thermal tune method. The uncertainties reported for h_0^{mec} and E_{Au} are obtained by error propagation of the uncertainties estimated by the linear fit of the stiffness-thickness data and the relative error of the spring constant of the AFM cantilever, found during calibration to be approximately 5%. The AFM tips 25Pt300B, NSC36B and NCHR have spring

constant equal to 18 $N\,m^{-1}$, 11 $N\,m^{-1}$, 5 $N\,m^{-1}$, respectively. The stiffness map shown in Figure 2.1c was obtained by the PinPoint mode of the AFM. NCHR tips in non-contact mode was used to measure the gold film thickness. To do so, during the gold deposition, we placed a glass carrier near each PDMS sample, and we covered partially the glass. The thickness was measured by scanning 40μm^2 area between the covered and uncovered part of glass/Au samples.

To investigate the dependence of the force-indentation curves on the tip radius, we vary the tip curvature by applying frictional wear. We first characterize the tip radius by performing NCM measurements on a tip-shape characterization sample (MicroMasch, PA01). We then approach the AFM tip on a microscopy slide glass surface and scratch in a controlled way (200 nm, 10 lines, 50nN Setpoint). Finally, the new radius is estimated as fitting parameters of force-indentation curves of pure PDMS with known elastic modulus, according to the Hertz model.

2.2.3 Van der Pauw measurements

A current of 100 mA is injected into the samples by means of Keysight SMU. Copper tape and silver paste are used to favor electrical contact between the gold thin film and the SMU. We measure the resistance of the film using four different configurations by varying the side in which the current is injected. The voltage is measured on the opposite side as in the standard van der Pauw setup.[112,113]

2.3 RESULTS

Figure 2.1a shows the basic experimental configuration that we exploit to investigate the nanomechanics of thin gold films on elastomeric substrates. Investigated samples contain a 0.7 mm thick Poly(dimethylsiloxane) (PDMS) layer attached to a glass carrier. On top of the PDMS films we thermally evaporated a thin titanium adhesion layer followed by a thicker gold layer (see experimental section for details). In an atomic force spectroscopy experiment, we push the tip against the surface and measure how the force increases as a function of the sample indentation. Typical indentation depth is about 100 nm. The thickness of the PDMS substrate ensures that the presence of the glass carrier is negligible as we probe less than 1% of the sample. Typical curves obtained for hard thin films on soft substrates such as PDMS/Ti/Au (blue) and PDMS/Au (red) are shown in **Figure 2.1b**. The curves show an immediate linear increase in force with indentation. Also, we observe an elastic response in which there is no hysteresis between the loading and unloading curves. This finding is at strong difference to indentation experiments performed on the pure PDMS substrate (black line). For PDMS forces are significantly lower and show a super-linear increase with indentation, precisely following the prediction of the Hertz model.[94,98–100] By performing indentation experiments at different positions on the surface, we can verify that the increase in stiffness due to the thin metal layer is constant throughout the surface (**Figure 2.1c**). From the high-resolution stiffness map shown in **Figure 2.1c** we obtain an average value of 1.3 $\mathrm{N\,m^{-1}}$ for a film of 38 nm Au. The small standard deviation of 0.07 $\mathrm{N\,m^{-1}}$ points to a homogeneously deposited metal film. Little variations only emerge due to local fluctuations in film thickness and grain structure as seen in the height map (**Figure 2.1c**). Differently, measurements at the border between stiff Au-islands and zones with exposed PDMS show an abrupt decrease of stiffness (**Figure 2.5a**).

To understand possible perforation of the metal film during indentation, we increase the maximum indentation force and combine the measurement with conducting AFM. In this way, it is possible to study the mechanical response of the bilayer, while monitoring the current flowing from the film into the tip. **Figure 2.1d** shows such a measurement with a force limit of 400 nN. Within this range the response is linear

and reversible, and a constant current is monitored between tip and sample. Increasing the force limit (**Figure 2.1d** right), we enter a second regime, in which at a critical force value (here 2000 nN), the current is interrupted, and indentation continues without further need to increase the force. During unloading, a strong hysteresis emerges in the indentation curve and the current remains at zero. These findings point to a fracture of the surface at critical forces. This is also confirmed by the surface topography measured after the indentation that shows a clear tip imprint once the threshold force is exceeded during indentation (**Figure 2.5b**).

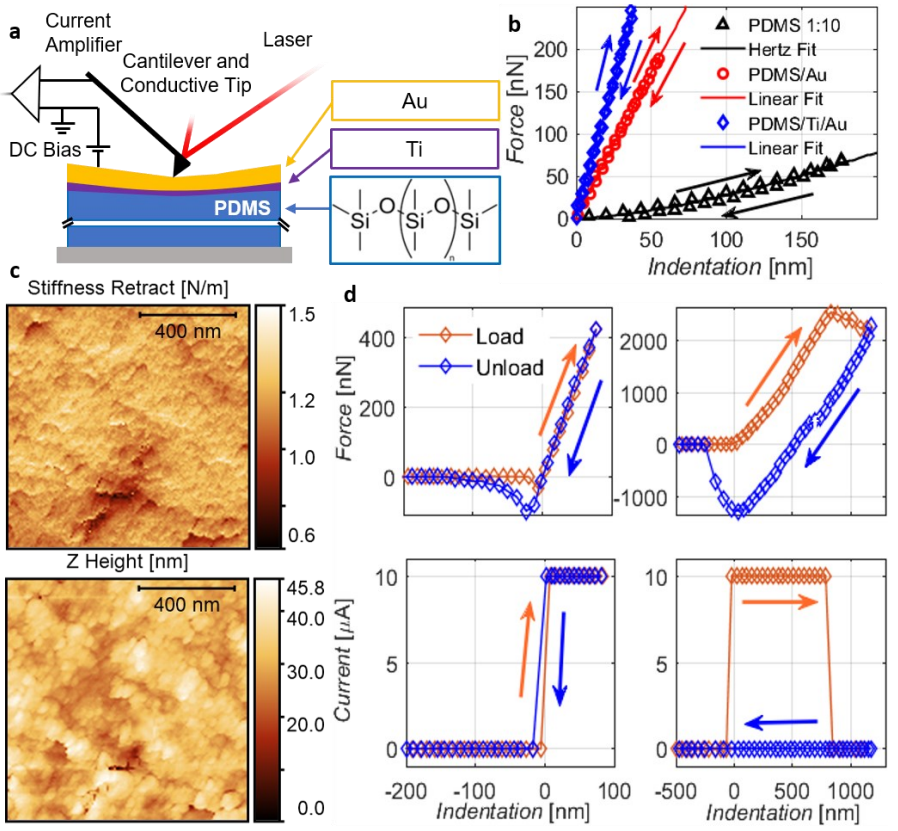

Figure 2.1. Nanomechanical and electrical characterization of thin gold films on elastomeric substrate. a) Scheme of the AFM experimental setup. b) Force–indentation curves on thin metal films of thickness 38 nm (Au, red) and 57 nm (Ti/Au, blue), compared to pure PDMS substrate (black) and the fit with Hertz model setting the tip radius to 20 nm. c) Height and stiffness map (128 x 128 pixel) of Au deposited on PDMS. d) Force–indentation and conductive AFM curves of PDMS/Ti/Au (40 nm thickness) with different force limits.

2.3.1 Analytical Model

From the experiments described above, profound differences emerge between the response of the pure PDMS and that of layered samples such as PDMS/Ti/Au and PDMS/Au: the presence of gold not only stiffens the system, but also modifies the force-indentation curve, which no longer follows the Hertz model. To obtain a quantitative description of this behavior, we consider the analytical model proposed by Lee *et al.*,[107] which represents the layered system as a thin elastic plate bonded to an elastic half-space, see **Figure 2.2a**. As described in the supporting information, the model yields a nonlinear analytical solution to the indentation mechanics. For our case we further simplify the model by representing the indenter as a concentrated force F and neglecting local Hertz-like deformations in the stiff metal layer. These assumptions are justified by the large mismatch of the elastic modulus of the metal layer with respect to the substrate. The resulting linear relation between force and indentation $F = K\delta$ is characterized by the stiffness K, i.e. the slope of the force-indentation curve, that can be expressed as:

$$K = \frac{3\sqrt{3}\,D}{l^2} = 3\sqrt{3}\left(\frac{4\left(1-\nu_{soft}\right)^2}{\left(1+\nu_{soft}\right)^2\left(3-4\nu_{soft}\right)^2}\frac{E_{soft}^2\;E_{hard}}{12(1-\nu_{hard}^2)}\right)^{\frac{1}{3}}\cdot h \qquad (2.1)$$

where, $E_{hard}, E_{soft}, \nu_{hard}$, and ν_{soft} are the elastic moduli and the Poisson's ratios of the hard thin layer and of the soft substrate, respectively, and h is the thickness of the thin layer. We note that the linearization of the force-indentation curves, removes any functional dependence on the indenter geometry. This differs greatly from other indentation models proposed in the literature such as the Hertz model or more advanced bilayer models.[96,98–100,114] In fact, in such models the shape of the indenter and local effects under the tip play a crucial role, as they determine the effective contact area, which is function of the indentation depth. For the here investigated case of $E_{hard} >> E_{soft}$, the linearized model appears suitable to represent the hard on soft bilayer behavior at small indentation. This is justified, by considering the characteristic length scale l defining the radius of the area on the rigid bending plate below the indenter which undergoes relevant vertical displacement. The characteristic length can be written as:

$$l = \left(\frac{D(1 + \nu_{soft})(3 - 4\nu_{soft})}{2E_{soft}(1 - \nu_{soft})} \right)^{\frac{1}{3}} \quad (2.2)$$

where $D = h^3 E_{hard}/12(1 - \nu_{hard}^2)$ is the flexural rigidity of the plate.[107] Using the typical experimental parameters, a value of $l = 1.1$ μm is expected and is clearly much larger than typical contact areas between the indenting tip and the surface. Accordingly, the indenter can be modeled as a concentrated force applied to the plate. Furthermore, the model neglects the shear deformability of the plate,[104] which requires $\frac{l}{h} \gtrsim 4$.

The conditions for the linearized solution are met when the ratio of the elastic moduli of the thin film and the substrate is high enough. This condition is equivalent to require that the ratio between the characteristic length scale l and the thin film thickness h is great enough. This fact highlights that the suitability of the linearized model depends on the thickness of the metal film. In our case, the ratio is on the order of 10^4. **Figure 2.2b** compares the analytical solution and its linearized version. For the computations we assumed bulk values for PDMS and Au as found in literature ($E_{hard} = 78$ GPa, $E_{soft} = 1.55$ MPa, $\nu_{hard} = 0.44$ and $\nu_{soft} = 0.5$), a gold layer thickness of $h = 44$ nm and a spherical indenter of radius $R = 20$ nm. As it is clearly visible from the plot, the linear term is dominant up to approximately 10 μm indentation. However, experimentally, a typical maximum indentation to perform AFM force spectroscopy is around 250 nm (**Figure 2.2b** inset). Furthermore, the fracture of the gold film occurs at loads in which the two curves are still overlapped. For example, with a tip of radius around 20 nm the fracture occurs at around 500 nN of load applied.

To further confirm the validity of the aforementioned conditions, we perform numerical simulations based on Finite Element Method (FEM). The input parameters of the numerical simulations are set equal to the ones reported for the comparison between the analytical solution and its linearized version. The inset in **Figure 2.2b** shows the numerical results in the typical experimental operating range compared to the two analytical curves. More details about numerical simulations can be found in the supporting information.

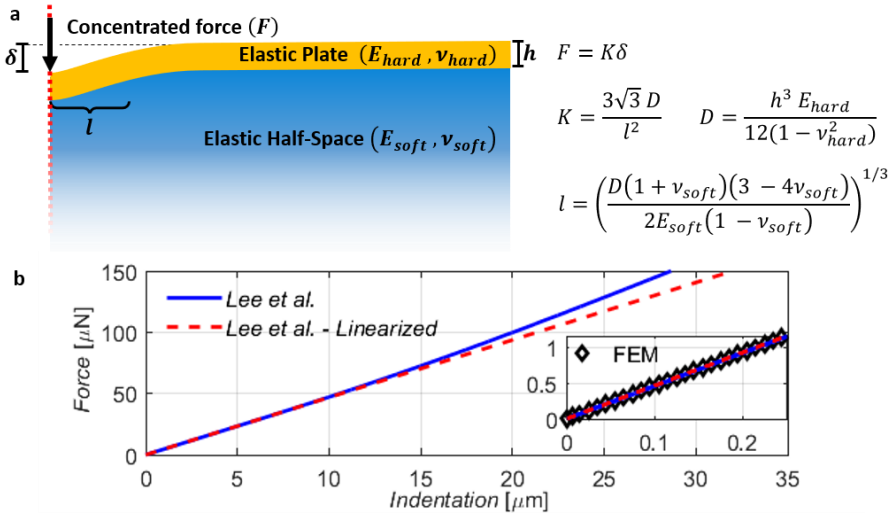

Figure 2.2. Indentation models for hard films on soft substrates: a) Scheme showing the main parameters. On the right the main equations of the model in case of indentation of a uniform layer bonded to an elastic half-space are reported. b) Calculated force-indentation curves according to the analytical solution (blue) and its linearized version (red).[107] The two curves start to diverge significantly at indentations exceeding 10 μm. The inset shows the calculated indentation curves in the experimental range of indentation. The black data correspond to the result of the FE numerical simulations.

2.3.2 Experimental validation of the model

To validate the model, we first investigate the impact of the indenter geometry by means of force spectroscopy with three different AFM tips, characterized by increasing radii of curvature, called R_1 (20 nm), R_2 (135 nm) and R_3 (490 nm), respectively. The acquired curves are shown in **Figure 2.3a** in different blue colors. We compare with indentation experiments performed on pure PDMS as represented in warm colors. For PDMS, as expected from the Hertz model, a strong dependence on the tip radius is found. Differently, the acquisitions made on PDMS/Ti/Au (cold colors) show superimposed force-indentation curves. Therefore, the experiments confirm the absence of any impact of the tip geometry, as predicted by **Equation 2.1**. Accordingly, the representation of the AFM tip as a concentrated force in the analytical model appears to be well justified.

Next, we investigate the variation of the response in samples with different gold thicknesses (20 - 60 nm). A linear relationship between thickness and stiffness, as predicted by the analytical model (**Equation 2.1**), is confirmed for both PDMS/Ti/Au and PDMS/Au, as shown in **Figure 2.3b**, where also the linear fit of the data are shown. We notice that the linear relation reported in **Equation 2.1** passes through the origin. Thus, the stiffness vanishes as the gold thickness goes to zero. Instead, **Figure 2.3b** shows that the linear fit of the experimental data results in an offset different to zero and extrapolation suggests a nominal gold layer thickness of h_0^{mec} at which the stiffness is zero. On this regard, we note that the nominal thickness of the evaporated metal film is evaluated by a quartz crystal balance calibrated by AFM measurements of layers deposited on a glass support. The presence of h_0^{mec} in the experimental data indicates the existence of an ineffective thickness of the metal film which does not contribute to the stiffness of the metal layer. Taking such effect into account, **Equation 2.1** can be rewritten as:

$$K = 3\sqrt{3}\left(\frac{4\left(1-\nu_{soft}\right)^2}{\left(1+\ \nu_{soft}\right)^2\left(3-4\nu_{soft}\right)^2}\frac{E_{soft}^2\ E_{hard}}{12(1-\ \nu_{hard}^2)}\right)^{\frac{1}{3}}\cdot(h-h_0^{mec}) \qquad (2.3)$$

In our case, in absence of titanium (red curves in **Figure 2.3b**), the evaluated ineffective thickness value is $h_0^{mec} = 11\ \pm 2$ nm, while, for PDMS/Ti/Au (blue curves in **Figure 2.3b**), we obtain $h_0^{mec} = 12\ \pm 3$ nm. We estimate E_{hard} from the slope of the linear fit of the thickness-stiffness experimental data using **Equation 2.3**. The Poisson's ratio of the hard film is set equal to its bulk counterpart, $\nu_{hard} = 0.44$. With the above settings, **Equation 2.3** yields $E_{hard} = 103 \pm 21$ GPa for PDMS/Au. No significant impact of the titanium adhesion layer on E_{hard} is observed, as it is estimated to be $E_{hard} = 110 \pm 22$ GPa for PDMS/Ti/Au (**Figure 2.3b** blue data points). Once the relation between film thickness and stiffness is found, the linear force-indentation curve can be obtained. **Figure 2.3c** shows a comparison between the model predictions and experimental data, showing a good agreement between the two.

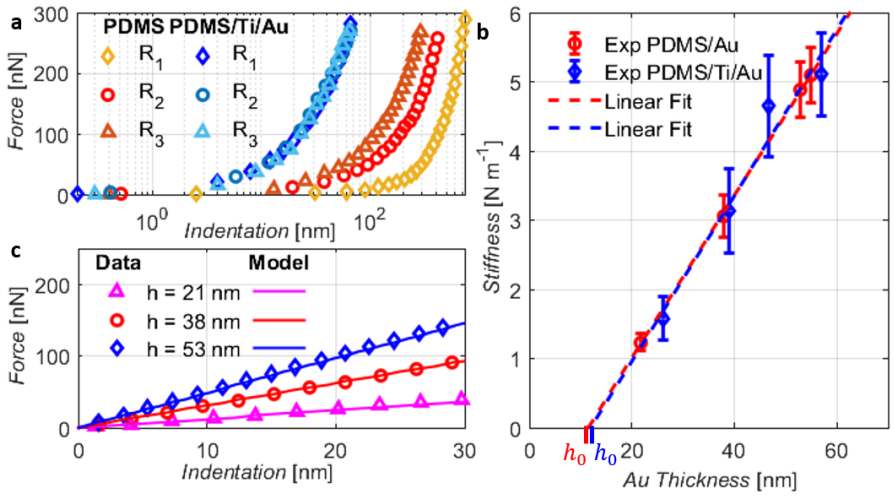

Figure 2.3. Experimental validation of the indentation model: a) Force–indentation curves acquired with three different AFM tips on both pure PDMS (warm colors) and PDMS/Ti/Au (blue colors). b) Stiffness dependence on the thin film thickness. Note that the experimental data shown in **Figure 2.3b** correspond to the average of the stiffness of the loading and unloading curves. This avoids possible systematical errors due to thermal drift during the AFM acquisition. c) Comparison between the experimental indentation curves and the model predictions for PDMS/Ti/Au samples of different thickness ($h = 21$ nm, $h = 38$ nm, $h = 53$ nm).

2.3.3 Nanomechanical and electrical properties influenced by thin film growth

In the former paragraph we found that the nominal thickness of the hard thin film systematically leads to an overestimation of the bilayer stiffness. Then, the presence of a mechanically ineffective layer of thickness h_0^{mec} has been introduced to explain the mismatch, leading to a good approximation of the experimental data. To understand the reasons for the presence of such a mechanically ineffective part of the gold layer, we perform AFM analysis of several samples with thicknesses lower than h_0^{mec}. **Figure 2.4a**, **Figure 2.4b** and **Figure 2.4c** compare the surface morphologies of the pure PDMS substrate and two bilayer samples with gold thicknesses 7.5 nm and 53 nm. The deposition of the 7.5 nm Au layer did not increase the overall surface roughness, which is characterized by a standard deviation of the height equal 0.31 nm, similar to the results obtained for pure PDMS ($std = 0.36$ nm). The only difference is that the small variations in surface height show a more granular structure.

Considering now the morphology of a film with thickness greater than h_0^{mec}, a completely different picture emerges: the deposition of a larger amount of gold leads to a rough surface ($std = 4$ nm) characterized by clusters whose diameter measures several nanometers. These images indicate that a continuous gold film is formed only for thicknesses greater than the threshold thickness h_0^{mec}. Below such thickness, the deposited gold clusters seem to permeate into the elastic polymer substrate giving rise to a diffused interface. Consequently, the deposited gold clusters do not connect between each other and offer no resistance against bending of the surface. This picture is further supported by the force-indentation curves acquired on the samples shown in **Figure 2.4d**. For samples with $h < h_0^{mec}$ the mechanical response follows the Hertzian curve.

The presence of a diffused interface is further confirmed by additional independent measurements of the electrical sheet resistance of the deposited films. Below h_0^{mec} we do not find any conductive behavior of the gold film. For thicker layers, above the onset of percolation, electrical conductivity is established. Using a van der Pauw contact geometry, the sheet resistance, R_s^{Au}, of the thin film is experimentally measured.[112,113] By using simple geometric arguments we express the thickness dependence of the sheet resistance as:

$$R_s^{Au} = \frac{\rho^{Au}}{h - h_0^{el}} \tag{2.4}$$

where ρ^{Au} is the resistivity of gold, h is its nominal thickness and, in analogy to the proposed mechanical model, an ineffective thickness, h_0^{el}, has been introduced. Below such threshold the gold film is not interconnected and is not conductive. We note that a similar threshold thickness for electrical conductivity was also reported by *Graudejus et al.* for thermally evaporated metallic thin films on silicone substrates.[115]

In analogy to the procedure used to study the mechanical behavior, it is possible to estimate h_0^{el} and ρ^{Au} by fitting the experimental data according to the **Equation 2.4**. As the sheet resistances differ by orders of magnitude, we fit the measurement data on a logarithmic scale as shown in **Figure 2.4e**. In this way, we evaluate $h_0^{el} = 13 \pm 3$ nm for PDMS/Au samples, that compares well to the mechanical measurements.

The estimated resistivity $\rho^{Au} = 127 \pm 21\,\Omega\,\mathrm{nm}$ is significantly larger than its bulk equivalent. The reason for the larger resistivity is associated to the disordered, cracked microstructure of the thin metallic film.

Both, mechanical as well as electrical measurements point to a critical thickness h_0, below which the metal layer is not continuous. A simplified scheme of such a situation is depicted in **Figure 2.4f**. Such diffused interfaces have been described for several cases in which metals were thermally deposited onto organic or polymeric substrates.[94] Migration of metal clusters into the polymer is possible due to the high kinetic energy and the small size of the arriving clusters. With the ongoing deposition, larger clusters start to condense closer to the interface and increase in size, so that penetration into the polymer becomes more and more unlikely. Finally, when the threshold thickness is reached, clusters percolate and a continuous film starts to build up. The amount of material diffused into the polymer does not contribute neither to the mechanical bending stiffness nor to the electrical conductivity.

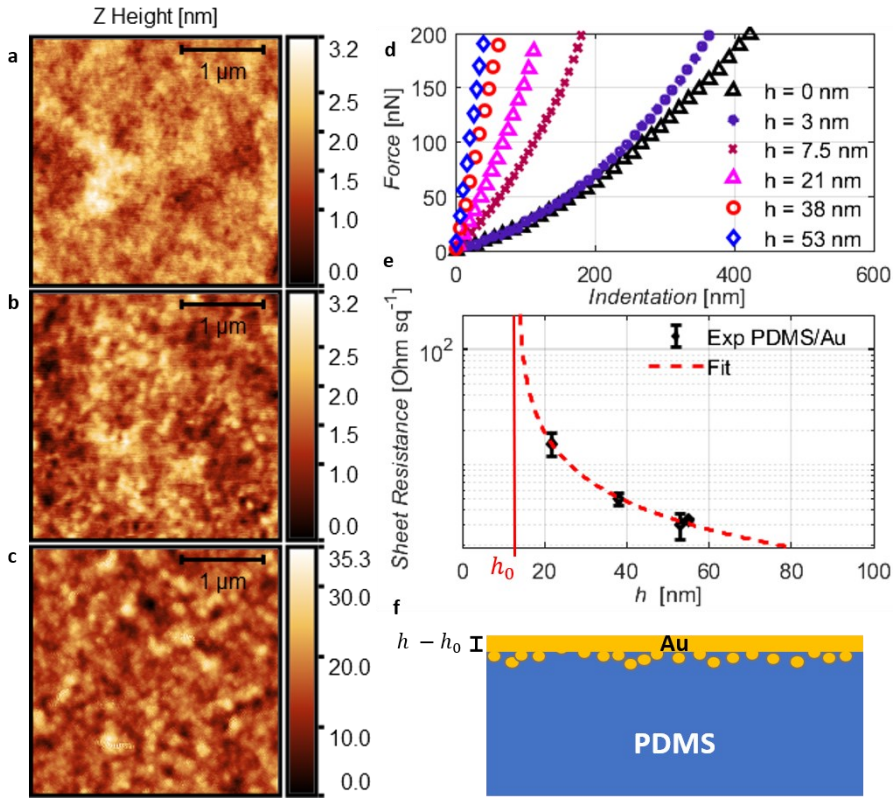

Figure 2.4. Relationship between gold layer thickness and electrical properties: a, b, c) Non–Contact Mode AFM images (128 x 128 pixel) acquired on pure PDMS (a), PDMS/Au with gold film thickness below (b) and above (c) the threshold value h_0^{mec}. d) Force–indentation curves of PDMS/Au with gold film thickness above and below the threshold value h_0^{mec}. e) Sheet resistance of samples with different film thickness. f) Qualitative representation of the effective thickness interpretation.

2.4 DISCUSSION AND CONCLUSIONS

Our work demonstrates how AFM indentation experiments can be performed and interpreted to investigate the nanomechanics of hard nanometer-thick metallic films on soft elastomer substrates. By combining the mechanical nanoindentation experiments with conductive AFM, we were able to distinguish perforation of the conductive surface that leads to irreversible damage and conductance failure. Instead, when nanoindentation experiments are performed with forces remaining below the critical fracture force, the response is elastic and reversible. In this elastic regime of

indentation, we find that the nanomechanics become independent on the indenter geometry and scale linearly with layer thickness. We achieve a quantitative description of this behavior by referring to the analytical model proposed by Lee et al. for the indentation of a hard uniform layer bonded to a soft, elastic half-space.[107] We show that a linearized version of the model already accounts for all the observed phenomena in the experimental parameter range and allows to relate the observations to mechanical material properties such as the elastic modulus and Poisson ratio of the involved materials. By comparing also to finite elements simulations, we find that the linearized model holds due to the large mismatch in elastic moduli between soft substrate and hard metallic thin film ($\frac{E_{hard}}{E_{soft}} > 500$). For such a situation the metallic film behaves effectively as a bending plate for which it is possible to disregard local deformation under the tip.

For the investigated case of gold thermally deposited on silicone elastomer we exemplify how the described method enables a deeper understanding on the relation between nanometer-thick film structure and its nanomechanical properties. By varying the gold layer thickness, we demonstrate that a significant increase in layer stiffness only happens above a threshold thickness h_0^{mec}. We explain the presence of this threshold by the penetration of initial evaporated gold clusters into the polymer substrate to create a diffuse interface that retards percolation of interfacial clusters into a continuous film. The existence of a percolation threshold is also confirmed by electrical measurements of surface conductivity that show an onset at a similar layer thickness. Once percolation is achieved, the film builds up a flexural rigidity and significant surface stiffening happens. From the quantitative analysis of the surface stiffness, we find a local Young's modulus of such ultrathin gold films of 103 ± 21 GPa. The value matches within its uncertainties the gold elastic modulus obtained in macroscopic deformation experiments. Interestingly, we find no significant impact on the investigated thin film nanomechanics by the thin titanium adhesion layer used to bind gold stronger to the elastomer substrate and to prevent delamination. This observation agrees with the analytical model presented by Lee et al.,[107] in which no effect of the adhesion between layer and substrate is found if the latter one is assumed incompressible ($\nu_{soft} = 0.5$). We further note that in our experiments the

delamination effects are not relevant, but they become important once a microcracked network is established to achieve reversible stretching stability.

In conclusion our work demonstrates a quantitative analysis of the surface nanomechanics of thin hard metallic films on soft substrates. It enables to extract the effective layer thickness and the local Young's modulus of the thin metallic layer. Both are parameters that are crucial to understand and predict the properties of such films once they are employed as stretchable conductors where their bending is needed to compensate tensile strain. So far nominal thickness values and bulk elastic moduli were used as parameters when modelling such systems to optimize strain compensating geometries.[102] Instead, our method provides an experimental access to the relevant parameters thereby paving the way towards a quantitative understanding and optimization of hard on soft interfaces for stretchable electronics.

2.5 SUPPORTING INFORMATION

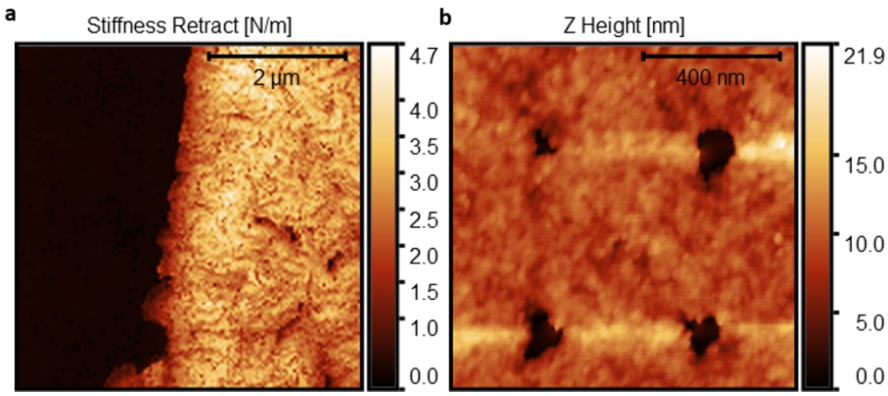

Figure 2.5. a) Stiffness map (128 x 128 pixel) on region of PDMS/Au bordering to pure PDMS region. b) Tip imprints left on the gold film by reaching the second regime during nanoindentation.

2.5.1 Introduction of the analytical indentation model and linearization

The analytical model for the indentation of a uniform stiff layer bonded to a homogeneous half-space has been proposed by Lee *et al.* [107] The relation between the force (***F***) and the indentation (***δ***), can be written as:

$$\delta = \frac{F}{D}\left\{\frac{l^2}{3\sqrt{3}} - \frac{l^2}{2\pi}\left[1+\frac{\pi D}{FR}\right]\exp\left(-2C-\frac{2\pi D}{FR}\right)+\frac{1}{4h^2}\left(\frac{D}{4FR}\right)^{\frac{1}{3}}\right\} \qquad (2.5)$$

where C is Euler's constant, R is the radius of the rigid spherical indenter, h is the plate thickness, D is the flexural rigidity of the plate and l, reported in **Equation 2.2**, is a characteristic length of the problem. Notice that **Equation 2.2** is valid if no sliding is allowed between the plate and the substrate. When sliding is allowed a different expression for l is provided in [107]. However, differences are limited to the 10% and the two coincide for incompressible substrates ($\nu_{soft} = 0.5$). In **Equation 2.5** the first term gives the contribution of a concentrated force representative of the indenter. The second term is a correction that takes into account the distribution of the load along the ring of contact between the indenter and the plate. The third term

considers Hertz-like local deformations of the plate under the indenter. It must be highlighted that **Equation 2.5** has only one linear term and that all the other terms depend on the indenter radius. Therefore, assuming the load to be concentrated leads to the linear force-indentation relation:

$$\delta = \frac{F}{K} \tag{2.6}$$

where K is the stiffness of the bilayer given in **Equation 2.1**.

2.5.2 FEM Model

We investigate also with numerical simulations based on FEM the independence of the force-indentation curve on the indenter radius. **Figure 2.6a** shows the setup of the axisymmetric FE model, together with a detail of the mesh under the tip. A mesh entirely composed of quadrilateral elements is adopted. The hard thin layer and the soft substrate are assumed as homogeneous, isotropic, linear elastic materials. We set the input parameters of the numerical simulations equal to the values used to compare the analytical solution and its linearized version (see **Figure 2.6b**). The indenter is assumed to be a spherical rigid body. Three radii have been considered, namely 20, 100, 400 nm. The computational domain is a square of side equal to 50 μm. The nodes on the axis of symmetry are fixed in the horizontal direction, while those at the bottom are constrained in the vertical direction. Concerning the numerical treatment of the contact problem, the indenter is defined as a master surface, while the layer is defined as a slave surface, together forming a contact pair. The normal contact is set to avoid interpenetration of the two bodies, while the tangential behavior is assumed to be frictionless. The hard film is assumed to be connected to the substrate without the possibility to slide. The great difference between the elastic moduli of the substrate and the metallic film, ensures that the contact area between the AFM tip and the metal film is substantially smaller than the characteristic length l, resulting in a linear force indentation curve which does not depend on the tip geometry. The FEM simulations have been carried out with different mesh sizes; however the variations turn out to be negligible, highlighting once again the independency of the force-displacement curves from the local deformation of the sample under the AFM tip.

It must be noticed that an infinite half-space is considered in the analytical model. Therefore, when comparing results of the analytical model to FEM results it is essential to ensure that the numerical domain is big enough with respect to l. For example, a variation of the domain side from $7l$ to $50l$ leads to force estimations that differ of 2%.

Figure 2.6b reports the output of three numerical simulations performed varying the indenter radius. It must be highlighted that we measure the displacement at the interface between the rigid indenter and the hard layer. In this way, also local deformations under the indenter are taken into account. Nevertheless, the three simulated force-indentation curves are practically coincident. Therefore, also the FEM numerical simulations confirm the suitability of the linearized version of the analytical model for the considered application.

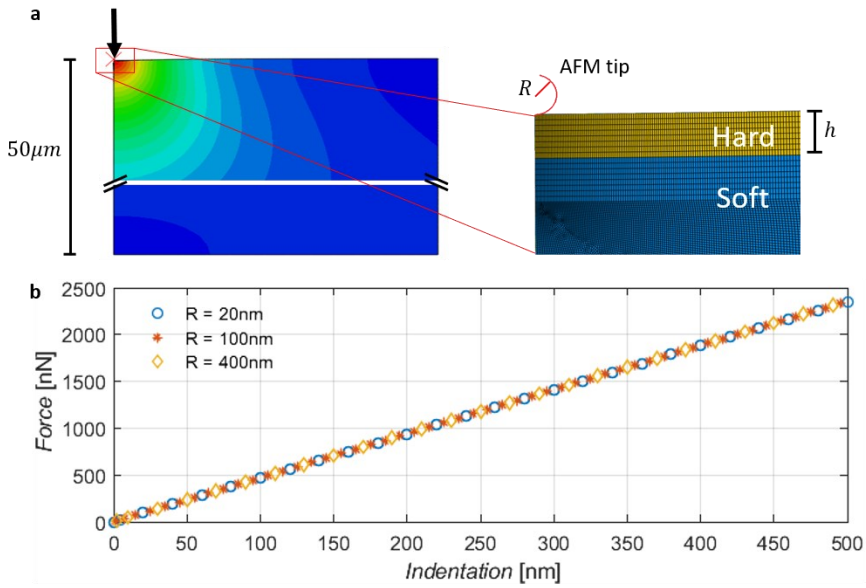

Figure 2.6. Finite Element Model. a) Example of vertical displacement map. Only the first 10 μm near the axis of symmetry are shown. The domain in the simulation is a square of side 50 μm. The inset shows details of the mesh in proximity to the indenter. b) Force-indentation curves obtained from numerical simulation with different indenter radii, namely 20, 100 and 400 nm.

3 *IN SITU* FORCE MICROSCOPY TO INVESTIGATE FRACTURE IN STRETCHABLE ELECTRONICS: INSIGHTS ON LOCAL SURFACE MECHANICS AND CONDUCTIVITY

The content of this chapter was published in the journal ACS Applied Electronic Materials.

Abstract

Stretchable conductors are of crucial relevance for emerging technologies such as wearable electronics, low-invasive bioelectronic implants or soft actuators for robotics. A critical issue for their development regards the understanding of defect formation and fracture of conducting pathways during stress-strain cycles. Here we present a novel atomic force microscopy (AFM) method that provides multichannel images of surface morphology, conductivity, and elastic modulus during sample deformation. To develop the method, we investigate in detail the mechanical interactions between the AFM tip and a stretched, free-standing thin film sample. Our findings reveal the conditions to avoid artifacts related to sample bending modes or resonant excitations. As an example, we analyze strain effects in thin gold films deposited on a soft silicone substrate. Our technique allows to observe the details of microcrack opening during tensile strain and their impact on local current transport and surface mechanics. We find that although the film fractures into separate fragments, at higher strain a current transport is sustained by a tunneling mechanism. The microscopic observation of local defect formation and their correlation to local conductivity will provide novel insight to design more robust and fatigue resistant stretchable conductors.

3.1 INTRODUCTION

Stretchable conductive thin films on polymeric substrates are of pivotal importance for several novel applications such as flexible and wearable electronics, stretchable bioelectronic implants, microelectromechanical systems, or soft actuators for robotics.[116–118] In these applications, the electrical properties of the thin film have to withstand the mechanically demanding deformations occurring during device operation and wear.[119] A fundamental problem regards the mismatch in elastic properties between conductive thin film and the dielectric substrate material. Conductivity relies on rigid metals or conducting polymers whereas the substrate is made of soft elastomers to warrant device compliance. Differences in elastic moduli spanning orders of magnitude are often the case and lead to the build-up of interfacial stress during deformation. The consequence are defect formation and defect evolution as observed in the form of thin film necks, cracks, fracture, and delamination. Understanding the microscopic mechanism of defect formation as well as the impact of defects on the electric properties is of paramount importance to optimize the mechanical wear resistance as needed in future application scenarios. Despite this need, microscopy techniques that characterize local morphological, mechanical, and electric properties of the metal layers *in situ* during the deformation process are still missing. [120,121] Only such multichannel imaging techniques will ultimately enable the correlation of morphological defects to the electrical response.

To date, several studies demonstrate optical or electron microscopy techniques combined with mechanical stretching to provide rapid imaging of the metallic surface during sample deformation.[64,116–118,122,123] Digital image analysis allows then to quantify the local strain field and to obtain quantitative information on the onset of crack formation, the crack length, and the crack density as a function of the strain.[121,124–126] These are all parameters of central importance to describe the fracture mechanics of such thin films. The drawback of optical or electronic imaging techniques comes from the reflection-based image reconstruction that cannot provide quantitative information on surface height changes. Accordingly, it is difficult to clearly distinguish through and part-through surface cracks or necking structures in tensile strain experiments or to distinguish bulged structures from delaminated ones. Instead, quantitative morphological information is provided by atomic force

microscopy or confocal laser scanning microscopy. First reports demonstrate the applicability of these microscopy techniques in *in situ* experiments combined with macroscopic mechanical testing and conductivity measurements.[127] Such data is highly needed to establish quantitative models for predicting the degradation of conductivity as a function of strain. [116,118,119,126,128–130]

Despite these successes, several crucial local properties of the thin metal film remain experimentally not accessible, hampering the development of more precise and realistic mechanical models. This regards in particular local conductivity, which is notoriously influenced by the development of the crack pattern. In fact, current models assume ohmic conductance in the defect-free parts of the metal layer, whereas through-thickness cracks are considered as completely isolating barriers.[131,132] Relying on these two assumptions, the determination of the conductivity of the cracked metallic film reduces to the determination of the geometry of the ohmically conducting pathway connecting through the fractured film. Once it is known, one can estimate the increase in the effective path length and its width reduction during the fracture process to predict the reduction in macroscopic conductivity. So far, no experimental confirmation has been obtained on these central assumptions. Observations such as the degradation of conductivity at large strain values point already to a more complicated role of local conductivity. [131]

To address these issues, we report here an *in situ* atomic force microscopy method that provides multichannel images of local surface morphology, mechanics, and conductivity on strained metal thin films. The method employs fast repetitive force spectroscopy experiments combined with a conducting AFM probe. Its application on a free-standing strained sample is demonstrated allowing efficient acquisition of multichannel images at different strain values. Possible artifacts due to substrate bending or resonant vibration are analyzed in detail to derive the optimized experimental conditions for AFM measurements on free-standing samples. As an example, we investigate the fracture of a thin gold film deposited with an adhesion layer on silicon elastomer substrates. Similar films have important roles as stretchable conductor lines in implantable electronics.[55,85,133,134] The combination of topographic, micromechanical and electrical imaging channels in our microscopy technique allows to clearly distinguish different defect types and to understand their effect on

the macroscopic properties. For example, we find that although the macroscopic conductivity shows linear ohmic conducting behavior, the local current paths connecting individual fragments behave in a strongly non-linear way at increasing strain. The observation points to the relevance of tunneling based transport processes in microcracked geometries.

3.2 EXPERIMENTAL SECTION

3.2.1 PDMS/Cr/Au preparation

PDMS was obtained by mixing crosslinker and Sylgard 184 silicone in a ratio of 1:8. After intensive stirring, the mixture was degassed to remove air bubbles. Few μms of PAA were spin-coated on the glass substrate before casting PDMS to decrease the adhesion. After pouring the mixture, 20 minutes were waited to let it spread homogeneously onto the glass. Samples were then stored for one hour at 70 °C in an oven. Then the chromium adhesion layer (5 nm thickness) and gold (18 nm thickness) were deposited on the glass/PDMS substrates by thermal evaporation (source sample distance = 25 cm, vacuum pressure = $5.5\ 10^{-6}$ mbar). Before clamping the sample in the strain stage, the sample was manually bent and twisted to pre-crack the gold surface to avoid the formation of a single crack cutting all conductive paths. The electrical contacts were made with copper tape and a conductive epoxy silver-based (without the hardener to keep it liquid), to increase the contact stability during strain variation.

3.2.2 AFM Probe

A Park System's NX10 AFM was used in the experiments. The Rocky Mountain Nanotechnology's probe 25Pt300B was used to perform fast repetitive force spectroscopy. The AFM tip used for resonant frequencies investigation was PPP CONTSCR, while for thickness measurement was NCHR, both from Nanosensors. Before each experiment, the tip sensitivity and force constant are calibrated by an indentation on a silicon surface and thermal tune method. The AFM tips 25Pt300B, PPP CONTSCR, and NCHR have spring constant equal to 18 $N\ m^{-1}$, 0.2 $N\ m^{-1}$, 5 $N\ m^{-1}$, respectively.

3.2.3 AFM resonant frequencies investigation

A loudspeaker (Visaton K50) was used as a source of acoustic waves and controlled by a function generator (integrated in the Zurich Instruments MFLI Lock-in Amplifier). The vibrations of the sample were probed by a very soft AFM tip (PPP CONTSCR) in contact with a setpoint force of 10nN. The Position Sensitive Photo Detector voltage signal (V_{a-b}) was recorded by a Lock-in amplifier as a function of the loudspeaker excitation frequency. Since the impact of 20nm thick metal layer on the resonance frequencies is considered negligible, we performed the experiments on pure PDMS substrates (2.1mm thick). The strain stage shown in **Figure 3.5a** and **Figure 3.5b** was used to apply different tensile strain values and sample oscillation was measured in the frequency range from 10 Hz to 40 kHz.

3.2.4 AFM multichannel imaging

Height, Stiffness, and current maps were generated by performing a fast force spectroscopy for each pixel of the image. Working in Contact mode, before the fast force spectroscopy the approach of AFM tip to the sample surface is performed. The approach is concluded when the setpoint force is reached. To move from pixel to pixel, the tip is lifted from the substrate. Then the XY stage is moved to place the new pixel below the tip and a tip approach is performed before the next force spectroscopy starts. As force spectroscopy parameters we set the maximum force to be 500nN, while the speed of the tip along the Z-axis was 100 $\mu m\ s^{-1}$. We set the lift height to be 1μm, the time for the pixel-to-pixel motion to be 5ms, and a pre-approach time of 100 μs. These parameters were optimized on PDMS/Cr/Au surfaces and an acquisition of a 128x128 pixels images of 40x40 μm^2 sample area is achieved in ca. 30 minutes. Current maps were obtained by applying a potential difference of 100 mV for strain 0% and 10V for greater strain values, between the sample and the tip. The macroscopic I-V curves were acquired with a SMU, tuning the voltage between -7 V and 7 V, and measuring the current.

3.3 RESULT

Our *in situ* atomic force microscopy technique is based on the experimental setup shown in **Figure 3.1a**. This setup provides multichannel acquisitions to map the surface morphology, micro-mechanics, and local conductivity as a function of the strain applied to the sample. A conductive AFM probe is used to perform simultaneously conductive AFM and force spectroscopy. During a conductive AFM experiment, a bias voltage is applied between the AFM probe and the sample to measure the local electrical current (I_{local}) that enters the probe through the contact area with the thin film. At the same time, the macroscopic current (I_{macro}) flowing in the entire sample is measured with a SMU. Uniaxial tensile strain is applied by a custom-designed strain stage in which a screw controls the distance between two clamps that hold the free-standing sample (**Figure 3.5**). The multichannel images are obtained through fast repetition force spectroscopy. Each pixel of the image corresponds to a force spectroscopy performed with a conductive probe and can thus provide information on surface height, stiffness and local current measured at a threshold force.

To test the AFM method, we analyzed the strain response of a thin gold film deposited with a chromium adhesion layer on a silicon elastomer substrate (PDMS). Such films are considered a prototype of a stretchable conductors, as during strain a pattern of microcracks evolves, that absorbs the strain by 3D deformation while maintaining an inter-connected conductive pathway in the gold layer.[111] **Figure 3.1b** shows an optical microscopy image of such a microcracked film with a gold thickness of 18nm and PDMS substrate of 2.1mm thickness as investigated in our experiments. A typical measurement curve acquired with force spectroscopy and conductive AFM on a gold region is shown in **Figure 3.1c**.[135] During the measurement the AFM probe is pushed into and retracted from the sample at constant speed while the force, the current and the tip position relative to the surface (indentation) are measured. When the tip contacts the conductive film, an increase of force and a sudden rise in current are recorded. During indentation, the current reaches a saturation value while the force increases linearly. Upon retraction, the force follows the loading curve as expected for an elastic response. Due to adhesion, the surface sticks to the tip when

it is displaced above the surface and a negative force is measured while the current remains stable until the contact is lost during snap off.

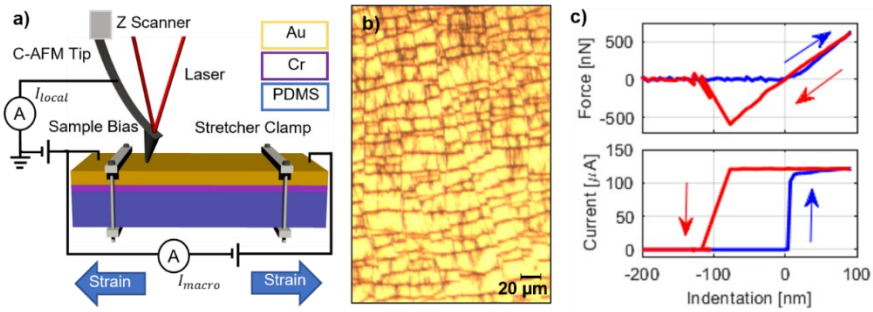

Figure 3.1. Experimental design of multichannel AFM *in situ* experiments. a) Scheme of the experimental setup. The stretcher used to apply tensile strain to the sample is represented by its clamps. The electrical circuit permits to apply a bias between tip and sample to measure local currents entering the conducting AFM tip and to also measure the macroscopic sample conductivity. b) Optical microscopy image of the investigated microcracked gold layer. c) Force-indentation and current-indentation curves obtained in a single-pixel acquisition. Blue and red arrows represent the load and unload, respectively.

Since the images are obtained through fast repetition of the force spectroscopy experiment, it is crucial to investigate the possible excitation of resonant oscillations of the free-standing sample that would interfere with the AFM characterization. To study resonant oscillations, we used the experimental setup shown in **Figure 3.2a**. Oscillation modes were excited by sound produced at different frequencies with a speaker connected to a function generator. The oscillations of the sample were probed by an AFM tip in contact with the sample. The AFM tip deflection signal was recorded with a Lock-in amplifier and analyzed as a function of frequency. **Figure 3.2b** shows the measured frequency response of the sample vibrations at different strain. As expected, an increase in strain corresponds to a shift of the resonance peak to higher frequencies. To ensure that the AFM measurements are not affected by the sample's vibrations, the fast repetitive acquisitions must operate at frequencies below the first resonance peak. The resonant frequencies of the sample depend on its dimensions and the strain applied. Therefore, these parameters define limits in which the setup can operate.

To understand the dependence of the resonant frequencies on the sample dimensions and the strain, we developed a model starting from the well-known Rayleigh quotient method for vibration analysis and compared it with the experimental results.[136] The sample is modeled as a pre-stressed plate clamped at two ends. Geometrical variations due to large strains and Poisson effect have been accounted for. In fact, as the strain increases, the length increases, while the width and thickness decrease. With these considerations we obtained the following formula for the first vibrating mode of a rectangular plate clamped at two ends to which a pre-stress is applied:

$$f_0^{1st}(\varepsilon) = \frac{\pi h}{3L^2}\frac{(1-\nu\varepsilon)}{(1+\varepsilon)^2}\sqrt{\frac{E}{\rho(1-\nu^2)}\left(1+\frac{3L^2}{\pi^2 h^2}\frac{\varepsilon(1-\nu^2)(1+\varepsilon)^2}{(1-\nu\varepsilon)^2}\right)} \qquad (3.1)$$

where L and h are the length and the thickness of the sample, respectively, while ρ is the density, E is the elastic modulus, ν is the Poisson's ratio and ε is the strain. More details can be found in the Supporting Information. We then compared the experimental results with the analytical model. To do so, we considered the dimensions of our sample and the PDMS material parameters ($h = 2.1\ mm$, $L = 19.5\ mm$, $\nu = 0.5$, $\rho = 0.965\ g\ cm^{-3}$, $E = 2.21\ MPa$). The elastic modulus of our PDMS substrate was determined from indentation experiments relying on the Hertz model for the indentation of a rigid spherical tip into an elastic half-space.[100] As shown in **Figure 3.2c**, the analytical model agrees well with the experimental results, even though no fitting parameters are involved. To exclude the excitation of substrate resonant oscillations, the force spectroscopy experiments have to be conducted in a frequency space below the first oscillation peak. The power spectral density of tip-sample interaction modes occurring during the approach and retract movement of the tip is shown in **Figure 3.2d**. The inset displays the related time transient of the tip-sample force as caused by vertical movements during consecutive fast force spectroscopy measurements. The power spectral density demonstrates that significant frequency components are only below 100 Hz. This is sufficiently lower than the frequency of the first sample oscillation mode starting at 300 Hz to exclude excitation of sample oscillatory modes and to warrant stable AFM measurement conditions.

A second possible artifact during force spectroscopy measurements on free-standing samples regards global sample deflection. It must be ensured that the displacement due to bending of the free-standing sample, δ_{flex}, can be neglected with respect to the local displacement under the tip, δ_{hertz}, during indentation. Combining the expressions for beam deflection with the Hertz model, the ratio between the deflection and the indentation is expressed as:

$$\frac{\delta_{flex}}{\delta_{hertz}} = \frac{L^3}{192I}\left(\frac{8FR(1-\nu^2)}{9E}\right)^{1/3} \tag{3.2}$$

where $I = \frac{Bh^3}{12}$ is the beam cross section inertia, and B is the sample width. Considering our experimental case, we obtain $\delta_{flex}/\delta_{hertz} = 0.0008$. Therefore, the bending of the sample is negligible with respect to the indentation. For this estimation we neglected the impact of the thin gold layer. A detailed discussion of **Equation 3.2** is provided in the Supporting Information.

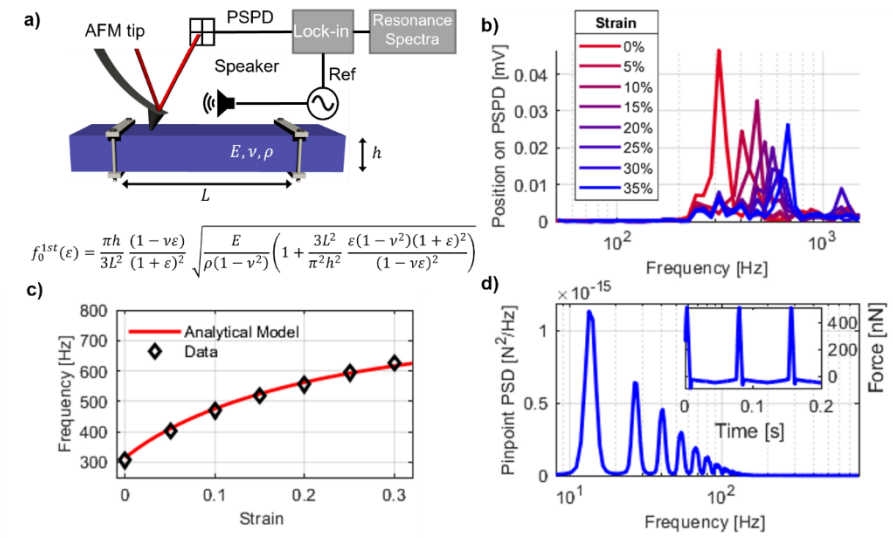

Figure 3.2. Investigation of measurement artifacts in AFM experiments on free standing stretched samples. a) Scheme of the experimental setup to measure the stretched sample's resonant frequencies. Oscillation modes are excited by sound produced at different frequencies. The response of the sample is measured with AFM in contact mode. b) Sample oscillation frequency spectra at different strains. Note that the peak corresponding to the first mode moves to the right as the strain increases. c) Peak frequency, extracted from the data in **Figure 3.2b**, as a function of strain. The red line corresponds to the analytical model. d) Power Spectral Density of forces between sample and AFM probe occurring during fast repetitive force spectroscopy acquisition. Note that tip-sample interactions occur at frequencies below the first vibration mode of the free-standing sample thus excluding possible resonant interactions.

Knowing the operational limits of our setup, we tested the *in situ* atomic force microscopy method on the stretchable conductor prototype PDMS/Cr/Au. **Figure 3.3** shows the surface height, stiffness, and current maps for three different strain values, 0%, 5%, 10% respectively. The blue dashed lines indicate the position of the profile reported at the bottom of **Figure 3.3**. The straining direction is indicated by the red arrows. The heights of the morphology map represent the Z position when the maximum force value is reached. The stiffness is calculated as the slope of the force-indentation curve, while the local electrical current is measured at maximum force. The morphology maps (Z Height) and the extracted profiles show that at 0% strain the microcracks are closed. As the strain increases, the size of the microcracks increases. As expected, cracks are oriented in a direction normal to the strain. The

maps show that the density of microcracks in the gold thin film is not strain-dependent: no new cracks are formed during the experiment. In the morphology map at strain 10% a second effect is present, the buckling of the gold layer. This is due to the Poisson effect, i.e. the compression of the sample in the direction orthogonal to that in which the strain is applied.[137] The stiffness maps show that the gold film is more compliant near the cracks. In fact, the width of the microcracks in the stiffness maps appears greater than about 1 μm, as measured from the profiles. It can be conjectured that this effect is caused by the loss of rigidity of the gold film when it is indented close to the microcracks.[107,135] Also, note that the stiffness of the gold film does not vary with strain. This indicates that the effect of strain on the single gold region is mainly to increase the distance to other regions, i.e. widen the microcracks.

From the stiffness maps, we estimated the elastic moduli of the thin metal film and the polymeric substrate. Considering the stiffness density distributions shown in **Figure 3.4a** one can see the presence of two peaks. The lower stiffness peak corresponds to the substrate and is therefore the result of the force spectroscopies performed in the microcracks. As the strain increases, the part of the image where microcracks are present increases. Therefore, the peak is more and more evident. On the other hand, the second peak corresponds to the force spectroscopies made on the regions with the gold film. Fitting the stiffness density distributions with a sum of two Gaussians, we estimated the average stiffness values of the PDMS (dotted lines) and the thin gold film (dashed lines). Given the mean values, we calculated the elastic modulus of PDMS with the Hertz model for a spherical rigid indenter in an infinite half-space obtaining the following values: $E_{0\%}^{PDMS} = 2.8 \pm 0.5\ MPa, E_{5\%}^{PDMS} = 2.6 \pm 0.5\ MPa, E_{10\%}^{PDMS} = 2.8 \pm 0.2\ MPa$. To calculate the elastic modulus of the gold thin film, we used the linear relationship between force and displacement as predicted by the indentation model of rigid thin film deposited on a compliant substrate.[135] The values obtained are: $E_{0\%}^{Au} = 92 \pm 23\ GPa$, $E_{5\%}^{Au} = 85 \pm 27\ GPa$, $E_{10\%}^{Au} = 125 \pm 43\ GPa$. The elastic modulus of the gold thin film is found to be comparable with the bulk value.

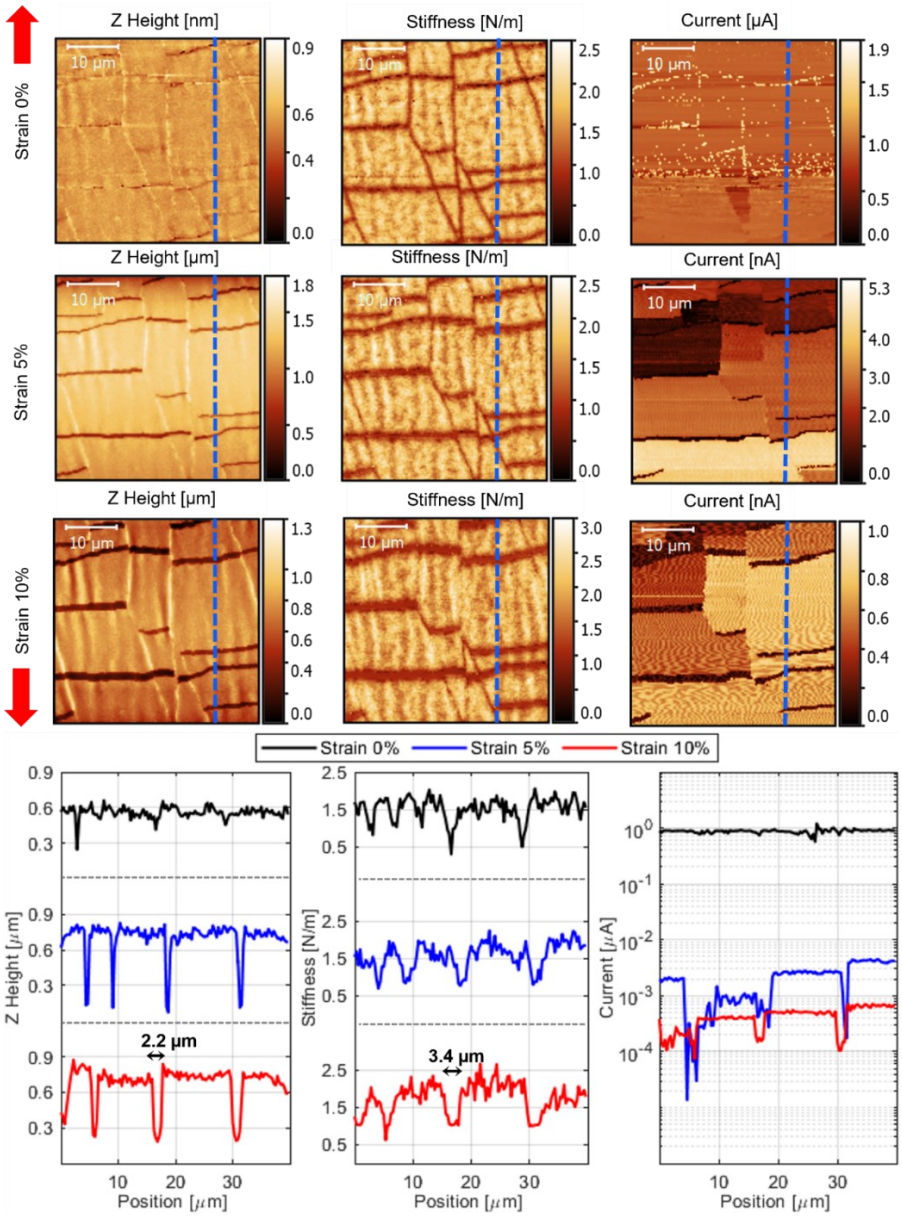

Figure 3.3. *In situ* AFM multichannel acquisition. a) Morphology, stiffness, and current maps as a function of strain acquired on the same region of a microcracked gold film deposited on PDMS elastomer. The strain direction is represented by the two red arrows on the left. b) Height, stiffness, and current profiles extracted from the AFM maps. The dashed blue lines in a) indicate the positions of the profiles.

Current maps shown in **Figure 3.3** were obtained by applying a potential difference of 100 mV for strain 0% and 10V for greater strain values, between the sample and the tip. At the same time, we apply a voltage difference of 7V between the two ends of the freestanding film to monitor its macroscopic conductivity and to induce a lateral contrast in the current maps. At 0% strain, the gold film is entirely conductive, and the presence of the microcracks does not seem to have a major impact. In this regime the measured current is limited by the tip-sample contact. At higher strain values instead, there is a drop in the conductivity of the sample. The measured currents are three orders of magnitude lower. Close observation of the current maps and comparison with the height maps allows to identify the two crucial factors that impact on the local current value: First, the height map shows that the microcracks separate the gold thin film into individual fragments and on the current map we see that each of such fragments is characterized by constant current signal. Accordingly, we can conclude that a high conductivity is preserved within a fragment and the current is limited by how the fragment is connected to the rest of the film. Second, the map shows that different fragments are characterized by different current values and higher currents are observed in fragments positioned closer to the bottom of the map. This correlates with the potential gradient that builds up along the current transport path through the microcracked film driven by the external potentials applied to the sample ($V_{top} = 0\text{V}, V_{bottom} = 7\text{V}, V_{tip} = 0\text{V}$). Hence, the current is also controlled by the local potential that builds-up on individual gold fragments. Barriers in the current transport path due to weakly connected fragments are overcome by stronger local electric fields hence causing a larger potential step between fragments. The current map contains therefore also important information on how the current transport through the microcracked film evolves during strain.

To investigate the current transport onto individual fragments in more detail, we perform conductive AFM I-V scans at different strain values (**Figure 3.4b)**. In the figure we compare the local conducting AFM analysis with the overall current flowing through the sample on normalized linear scale and logarithmic scale. Both, local AFM-current as well as macroscopic sample current, show a significant decrease with increasing strain. However, the macroscopic I-V curves maintain a linear, ohmic behavior, while the local current curves show a transition from linear

at 0% strain to superlinear at elevated strains. The observed shape suggests that charge transport at the microscale between the gold fragments occurs by a field enhanced tunneling effect. Similar measurement curves have been obtained by studying the tunnel effect in gold nanogap junctions.[138,139] A quantitative description of tunneling transport across metal-insulator-metal systems is provided by the Simmons model.[140] The model introduces as parameters the insulator width (s), the height of the potential barrier (φ), and the overall current scale (A), which corresponds to the area of the two metal regions where charge transport by the tunneling effect occurs. The model provides a good fit to our data and the obtained parameter values are reported in **Table 3.1**. The barrier height of 5.4 eV and the gap size of a few angstroms indicates a dielectric mediated tunneling mechanism that proceeds through gaps between different gold fragments. Although the significant strain causes a widening of the cracks in the thin film, in the direction orthogonal to the strain, fragments remain closely spaced therefore enabling a tunneling mediated transfer path. In the macroscopic current measurement, the transition to the superlinear behavior is not present because a large number of fragments participate in the transport path. Accordingly, several small cracks have to be overcome and they all induce small potential steps driving field induced tunneling. At individual steps the potential drop remains strongly below the tunneling barrier height and a linear response is maintained.

	$s\,(\text{Å})$	$\varphi\,(eV)$	$A\,(\text{Å}^2)$
Strain 5%	2.80 ± 0.04	5.7 ± 0.2	0.29 ± 0.01
Strain 10 %	2.86 ± 0.02	5.4 ± 0.1	0.11 ± 0.01

Table 3.1. Parameters of the Simmons model estimated by fitting the local I-V experimental data.

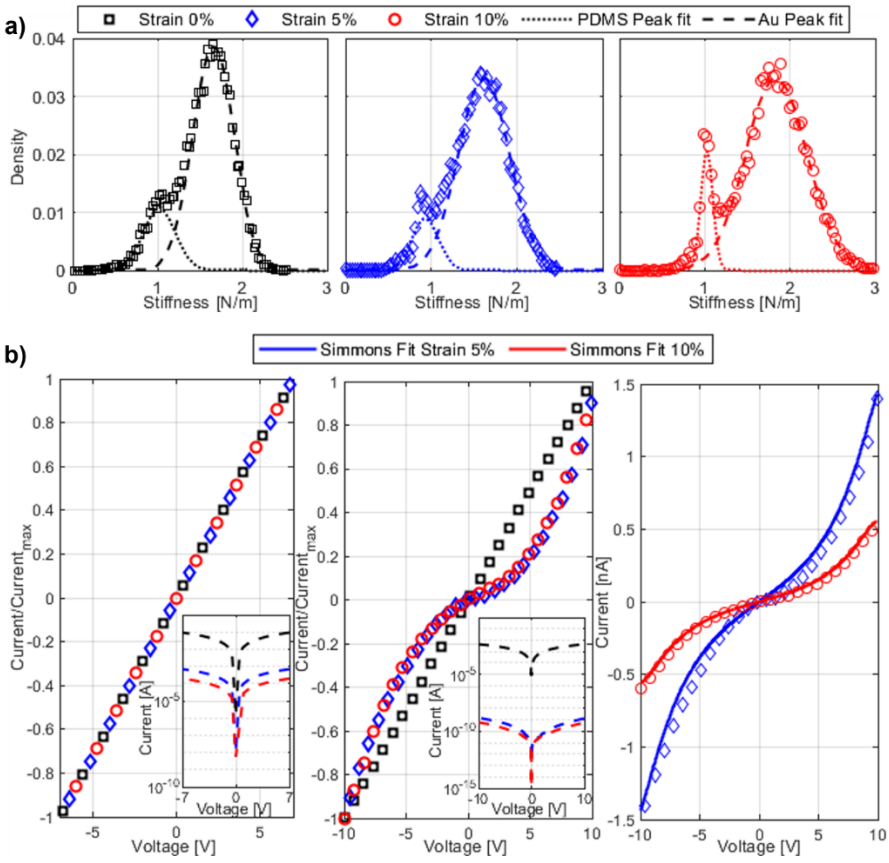

Figure 3.4. a) Stiffness histograms obtained from stiffness maps at different strains. The peak at lower stiffness corresponds to the PDMS, while the peak at higher stiffness corresponds to Au thin film. The dotted and dashed lines are Gaussian fit to estimate the average stiffness of PDMS and Au, respectively. b) the first graph on the left shows the macroscopic I-V curve of the entire metallic thin film at different strains. The graph in the middle shows the microscopic I-V curve of a single gold region acquired with C-AFM at different strains. The insets report the same data in a semilogarithmic plot to show the orders of magnitude. The graph on the right shows the microscopic I-V curve not normalized and fitted with the Simmons model describing the tunneling for a metal-insulator-metal system.

3.4 CONCLUSIONS AND DISCUSSION

Our work demonstrates a novel *in situ* experimental method to investigate strain effects in materials and devices for stretchable electronics. Based on fast repetitive force spectroscopy acquisitions with a conductive AFM probe the method enables the microscopic investigation of morphological, mechanical, and electrical properties as a function of strain. The development became possible through a detailed investigation of possible artifacts that can occur when dynamic AFM techniques are performed on a free-standing substrate, only attached at its two ends to the clamps of a tensile stretcher. By deriving and testing the analytical equations that describe substrate deflection and resonant vibrations (**Equation 3.1** and **Equation 3.2**), we find the experimental conditions for stable, artifact-free image acquisitions. Disturbing sample deformation modes can be reduced by using elastic substrates with a sufficiently large thickness to length ratio, high elastic modulus or by operating force spectroscopy at slower approach and retract velocities to avoid excitation of resonant modes.

Once the conditions for stable measurements are met, our method provides an unprecedented multichannel imaging technique to correlate morphological defects generated during tensile strain with the mechanical and electrical response. As an example, we analyze the tensile deformation and conductivity changes of a thin gold film deposited with a chromium adhesion layer on silicon elastomer substrates (PDMS). With our experimental setup, we provide unique insight into the mechanisms of charge transport across gold regions separated by microcracks. For this the combination of all three imaging channels is crucial: First, the surface height mapping allows to identify gold fragments surrounded by microcracks and to investigate their morphological evolution during strain. Second, the micromechanical imaging channel provides quantitative measures on the local elastic modulus. It demonstrates that the externally applied strain is locally absorbed in micro-crack widening while gold fragments do not alter their physical extension and stiffness properties as increasing strain. Third, the local conducting properties demonstrate that individual gold fragments remain highly conductive, and transport is crucially determined by cracks separating the conducting fragments. We note that for gold on elastomer films, the processing conditions such as gold and adhesion layer thickness

as well as pretreatment procedures have a crucial impact on how the microcrack pattern forms and separates islands. In the case studied here, we find at lower strains that a fully conductive, ohmic pathway remains present even though cracks widen in the direction perpendicular to the strain. Instead at higher strains, our detailed analysis of local IV-curves demonstrates the transition from the ohmic regime into a tunneling dominated regime, where local barriers have to be overcome by a field enhanced tunneling mechanism. We associate such barriers to microcracks oriented in the direction parallel to the strain. Only in this direction, cracks do not open significantly, thus leaving fragments in close enough proximity to permit tunneling transfer.

In conclusion, our work demonstrates a new *in situ* experimental approach to investigate mechanical and electrical properties and their correlation at the microscale. It enables to map properties of stretched samples as a function of strain and to access experimentally the local electrical properties. Both are crucial aspects to understand and predict the properties of stretchable conductors. We highlight the value of the method by demonstrating the transition from local ohmic transport to field enhanced tunneling at increasing tensile strain in a microcracked gold layer. So far, models on the conductivity of thin films subjected to strain, assume ohmic transport in the defect-free parts of the metal layer, whereas through-thickness cracks are considered as completely isolating barriers.[131,132] However, our results show that charge transport occurs even if a conducting fragment is completely surrounded by microcracks due to the tunneling effect, introducing a conduction mechanism that has not been accounted for in models.

3.5 SUPPORTING INFORMATION

The multichannel images of the *in situ* AFM experimental method proposed in this work are obtained through fast repetition of the force spectroscopy experiment. Therefore, it is crucial to investigate the possible excitation of resonant oscillations of the free-standing sample that would interfere with the AFM acquisitions. A picture of the strain stage is shown in **Figure 3.5a**, while a picture of the experimental setup showing the free-standing configuration, is reported in **Figure 3.5b**. To understand the dependence of the resonant frequencies on the sample geometry and the strain, we developed a model starting from the well-known Rayleigh quotient method for vibration analysis and compared it with the experimental results.[136] The sample is modeled as a pre-stressed rectangular plate clamped at two ends. Geometrical variations due to large strains and Poisson effect have been accounted for. In fact, as the strain increases, the length increases, while the width and thickness decrease. Denoting with u the transverse displacement of the plate and with x the axis on the plate mid-surface and orthogonal to the clamps, we assumed $u\,(x) = \frac{1}{2}\left(1 - cos\left(\frac{2\pi x}{L}\right)\right)$ as approximating function for the first vibration mode of the plate (cylindrical bending), with $x \in [0, L]$. With these assumptions, using the Rayleigh quotient method, we obtained the following formula for the frequency of the first vibration mode:

$$f_0^{1st}(\varepsilon) = \frac{\pi h}{3L^2}\frac{(1-\nu\varepsilon)}{(1+\varepsilon)^2}\sqrt{\frac{E}{\rho(1-\nu^2)}\left(1+\frac{3L^2}{\pi^2 h^2}\frac{\varepsilon(1-\nu^2)(1+\varepsilon)^2}{(1-\nu\varepsilon)^2}\right)} \qquad (3.3)$$

where L and h are the length and the thickness of the sample, respectively, while ρ is the density, E is the elastic modulus, ν is the Poisson's ratio and ε is the strain.

We then investigated the impact on force-indentation curves of the bending of the sample. In fact, considering the force applied from the AFM tip as a concentrated force, it must be ensured that the bending of the free-standing sample can be neglected with respect to the indentation of the tip inside the sample. To get an estimate of the bending at the center of the sample, we assumed the plate to behave like a beam clamped on both ends. The stiffness of the beam is then given by the formula:

$$K_{flex} = \frac{192EI}{L^3(1 - \nu^2)} \tag{3.4}$$

where $I = \frac{Bh^3}{12}$ is the beam cross section inertia, and B is the sample width. Notice that such approach is valid only if B is smaller than L, and the error for $B = L$ is approximately 10 %. The plate deflection is then $\delta_{flex} = F/K_{flex}$. The validity of this description has been confirmed with numerical simulations. An estimate of the indentation of the AFM tip on the PDMS sample is given by the well-known Hertz model for a rigid spherical indenter in an infinite half-space. Therefore, it can be expressed as $\delta_{hertz} = \left(\frac{3F(1-\nu^2)}{4E\sqrt{R}}\right)^{2/3}$. The ratio of δ_{flex} and δ_{hertz} allows understanding of which between indentation and bending is the dominant term. The ratio can be expressed with **Equation 3.2**.

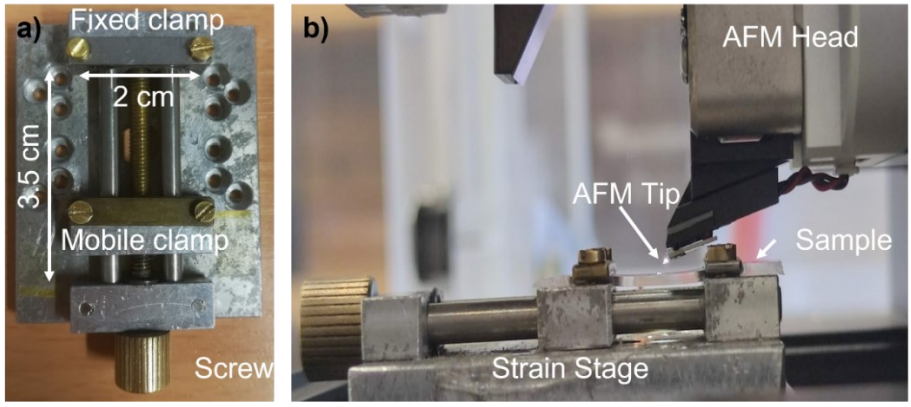

Figure 3.5. a) Photo of the strain stage with its dimensions. b) Photo of the experimental setup with sample clamped to the strain stage under the AFM tip.

4 DETERMINATION OF STIFFNESS AND THE ELASTIC MODULUS OF 3D-PRINTED MICROPILLARS WITH ATOMIC FORCE MICROSCOPY-FORCE SPECTROSCOPY

The content of this chapter was published in the journal ACS Applied Material and Interfaces.

Abstract

Nowadays, many applications in diverse field are taking advantages of micropillars such as optics, tribology, biology, and biomedical engineering. Among them one of the most attractive is three-dimensional microelectrode arrays for in vivo and in vitro studies, such as cellular recording, biosensors, and drug delivery. Depending on the application, the micropillar optimal mechanical response ranges from soft to stiff. For long-term implantable devices, mechanical mismatch between the micropillars and the biological tissue must be avoided. For drug delivery patches, micropillars must penetrate the skin without breaking or bending. Accurate mechanical characterization of micropillar is pivotal in the fabrication and optimization of such devices, as it determines whether the device will fail or not. In this work, we demonstrate an experimental method based only on AFM force spectroscopy that allows to measure the stiffness of a micropillar and the elastic modulus of its constituent material. We test our method with four different types of 3D inkjet printed micropillars: silver micropillars sintered at 100 and 150°C, polyacrylate microstructures with and without a metallic coating. The estimated elastic moduli are found to be comparable with the corresponding bulk values. Furthermore, our findings show that neither the sintering temperature nor the presence of a thin metal coating play a major role in defining the mechanical properties of the micropillar.

4.1 INTRODUCTION

Micropillars are three-dimensional microstructures characterized by a very large extension in one dimension resulting in a great aspect ratio. Nowadays, many applications in diverse field are taking advantages of micropillars such as optics, tribology, biology and biomedical engineering. [141–144] Usually micropillar are fabricated in a clean room by subtractive processes such as photolithography in combination with dry and wet etching, wire-electrode cutting, bulk micromachining, and laser cutting. [3,145–147] One microfabrication method that is gaining more momentum is 3D inkjet printing. It is an attractive technique for micropillar production because it allows flexible, room-temperature, scalable, and economical fabrication processes. [148–150] In the field of biology and biomedical engineering, among all the applications of micropillar, perhaps the most relevant are 3D microelectrode arrays (3D MEAs).

Three-dimensional microelectrode arrays have attracted considerable interest due to their use in various applications for *in vivo* and *in vitro* studies, such as cellular recording, biosensors, and drug delivery.[1-12] This is because three-dimensional structures allow for increased device area, spatial resolution and signal-to-noise ratio. In the case of cellular recording, conductive micropillars are exploited as interface between the device and the cell under investigation to measure the action potential. Regarding biosensors and biomedical implants, the micropillar-based electrodes act as a vital component for monitoring organ activity, and electrically/optically/thermally stimulated therapy. [162–167] In the electrode-tissue interface, the mechanical mismatch between the tissues and the electrode must be minimized to avoid invasive tissue damage and related losses of device. Damaged tissue and scar formation ultimately causes weakly coupled electrode-tissue interfaces with strong attenuation of recorded signals. In addition, implantable microelectrodes have to be designed for long-term applications, so they must adapt to the mechanical strains exerted by the surrounding tissue, while maintaining good coupling with the tissue for recording and stimulation. [12–16] Pillar-like structures, called microneedle, are often use in drug delivery patches to penetrate the skin and release the drug.[168] The drug is loaded into the pores of the microneedle and can diffuse out of the pores when the matrix penetrates the skin. In this case, microneedle

must be able to penetrate the human stratum corneum (~10-20 μm) without breaking or bending. Needle breakage or failure during or after patch application may alter the drug release profile leading to premature and uncontrolled drug release.

Accurate characterization of the mechanical properties of individual micropillar is a very challenging but a crucial aspect in the fabrication and optimization of patterned surfaces and biomedical devices in different applications. In fact, the mechanical properties of individual micropillars vary depending on the material, geometry, and fabrication method and are critical in determining whether the device will fail or perform properly. The characterization of the mechanical properties of individual micropillars is limited by the lack of experimental techniques that are easy to access and use. Most characterization methods available nowadays require that the instrument used for mechanical testing is mounted inside a Scanning Electron Microscope (SEM). The use of SEM is necessary to monitor the displacement in real-time during the mechanical test. Nanoindenters, tensile machines, or Atomic Force Microscope (AFM) inside a SEM chamber, have been used to test tensile, compression, and bending of micropillars. [169–178] Although these approaches lead to reliable results, they require expensive and difficult to use instrumentation. For these reasons, some early experimental techniques with AFM that do not involve SEM have been proposed. These techniques consist of bending tests on pillar-like structures clamped at both ends or cantilevered. [74,179,180] However, most of these methods have been developed for samples obtained using top-down fabrication techniques and require specific designs to hold the sample. It is therefore crucial to develop techniques that allow to measure mechanical properties of individual micropillars, considering their actual geometry. This is indeed a crucial step for the design and, optimization, so that it is desirable to develop techniques for rapid implementation, which require only easy to access equipment.

In this paper, we demonstrate a reliable and easy to operate AFM method to characterize the stiffness and elastic modulus of inkjet-printed micropillars. The method is based on force spectroscopies performed with the AFM tip in contact with the sidewall of the micropillar. By measuring the deflection of the micropillar at different lengths, we obtained the stiffness as a function of micropillar length. In the

measurements we find that the tangential force acting on the AFM tip has a significant impact causing an apparent stiffness variation between loading and unloading. To analyze the data we introduce a mechanical model that relates the stiffness variation with length to the micropillar geometry and elastic material properties. To test our method we characterize micropillars obtained using different inks and microfabrication procedures. Sintered, porous, metal nanoparticle-based pillars were compared to similarly sized polymeric structures. Specifically, 4 types of samples were considered: silver nanoparticle-based micropillars sintered at 100 and 150°C and polyacrylate (PA) micropillars with and without a metallic coating. Silver, commonly used as a conductive material in inkjet printing, was sintered at lower temperatures to promote its use on thermally sensitive substrates. PA was chosen as a non-porous equivalent to the silver-based micropillar (view **Figure 4.4** in the Supporting Information for internal structures of both micropillar types). We decided to test Ag micropillars, as they have already been used for biomedical *in vitro* applications.[148] We then tested PA micropillars, as the material has a significantly lower elastic modulus (by almost two orders of magnitude), confirming that the experimental method can also be used for less rigid materials. Our measurements highlight that all the fabricated micropillars show a stiffness – pillar length relation that follows a cubic power-law. Accordingly the printed micropillar can be modelled as a beam with circular cross-section of constant radius. The elastic moduli obtained for the pillars are consistent with those for the corresponding bulk materials and only minor variations are found for pillars obtained with lower sintering temperatures or for pillars with metal coating.

4.2 EXPERIMENTAL SECTION/METHODS

4.2.1 3D Inkjet printing micropillar arrays

Three-dimensional printed micropillar arrays were printed on 125 µm thick polyethylene naphthalate (PEN) substrate with an inkjet printer (CeraPrinter F-Series, Ceradrop) using 1 pL cartridges (DMC-11601, Fujifilm Dimatix). Two different inks were used: silver nanoparticle (Silverjet DGP 40LT-15C, Sigma-Aldrich) and UV-curable polyacrylate ink (DM-IN-7003-I, Dycotec Materials Ltd.).

Silver 3D inkjet printed micropillars

Following the procedure described in literature [148], Ag micropillars were printed with 3212 droplets. Samples were thermally sintered at 100 and 150 °C for 2 h. After sintering, the samples were cooled back down to room temperature in one hour. Using a 3-axis UV laser marker (MD-U1000C, Keyence) the substrates were cut to the desired dimensions (2.5 cm x 1 cm). The laser used a shutter frequency of 100 kHz, set at 1.5 kW, and a writing speed of 100 mm s^{-1}. The outline was etched with the laser with a total of 100 repetitions.

Polyacrylate 3D inkjet printed micropillars

Prior to printing, the polyacrylate ink was allowed to equilibrate to room temperature before being filtered through a 0.22 µm polyethersulfone (PES) filter (TPP) and loaded into a cartridge, which was covered with Al foil to protect the content against light. For the UV-curable polyacrylate (PA) ink, the same waveform as previously described was used. [148] The nozzle plate and the sample stage were held at 40 and 50 °C, respectively. With an appropriate working distance, 400 droplets of PA ink were ejected to form the micropillars. In order to form the 3D shape, individual droplets were consecutively cured (1 J cm^{-2}) layer-by-layer.

Metal-coated polyacrylate 3D inkjet printed micropillars

PA 3D structures were coated with Ti (10 nm, deposition rate of 0.1 nm/s) followed by Pt (150 nm, deposition rate of 0.2 nm/s) using a high vacuum coating system (BAL-TEC Med 020, LabMakelaar Benelux BV). The pressure inside the deposition chamber was 7.2 µbar.

4.2.2 3D printed micropillars length and diameter measurements

The lengths of micropillars range from 700 µm to 1100 µm. The length values have been obtained as the difference between the Z positions of the AFM probe, when it has been approached to the top and to the base of the 3D printed micropillars, respectively. The average diameter of Ag micropillars is 33 ± 1 µm, while for PA micropillars it is 37 ± 1 µm. The diameters have been measured exploiting the optical microscope mounted on top of the AFM probe.

4.2.3 Sample preparation for AFM mechanical characterization

SU8 3005 epoxy resin (KAYAKU, Advanced Materials) was used to bond the 3D printed micropillar array printed on PEN foils to glass slides. The dimensions of the slides were 1 cm width, 2.5 cm length and 1 mm thickness. The resin was continuously spincoated using three different speeds. An initial speed of 500 rpm was used for 10 s (a = 100 rpm/s), followed by 3000 rpm for 30s (a = 100 rpm/s), and finishing with 6000 rpm for 10 s (a = 500 rpm/s) in order to avoid edge effects.[181] The resin was pre-cured by soft baking at 95°C for 3 min (hotplate, Harry Gestigkeit PR 5-3T) with the foil containing the micropillars on top. For curing, an OtoFlash (model G171, NK-Optik GmbH) system with 2000 flashes set at a wavelength of 365 nm was used. Finally, the samples were again heated on the hot plate using three different temperatures. An initial temperature of 65°C (1 min) was used, followed by 95°C (3 min), and finishing with 150°C (2 min). The temperature variations were done gradually (3 min). Once cooled to room temperature, the PEN film is bonded to the carrier glass slide. To allow AFM characterization, 3D inkjet printed micropillars were positioned close to the carrier substrate border (ca 150 µm).

4.2.4 AFM tip calibration

The AFM system used in this work is NX 10 from Park System with an AFM tip 25Pt300B from Rocky Mountain Nanotechnology. The sensitivity of the tip (19.5 ± 0.3 V/µm) was calibrated on a silicon surface. The force constant for the AFM cantilever (18 N/m) was provided by the manufacturer. To avoid possible indentation effects of the AFM tip in the micropillar, we used a tip with a radius of curvature of 1.5 µm. The radius was obtained by starting from the value given by the manufacturer (10 nm) and scratching the tip on a Si sample. The radius was measured by performing several indentations on a polydimethylsiloxane (PDMS) sample of known elastic modulus (E = 2 MPa) and fitting the curves applying the Hertz's model for the case of spherical rigid indenter.

4.3 RESULTS AND DISCUSSION

Our experimental method is based on force spectroscopy, in which the AFM tip exerts a cyclic load applied to the sidewall of the 3D inkjet printed micropillar (**Figure 4.1a**). A scheme of the experimental setup is shown in **Figure 4.1b**. Initially, the contact between the AFM tip and the sample is established. Then the probe is moved following a trajectory along the Z axis until a maximum user-defined displacement is reached. Afterwards, the direction of displacement is reverted to conclude a measurement cycle. To study bending, it is necessary to apply the load to the lateral surface of the micropillar. Therefore, a dedicated sample holder was designed to position the micropillar in the XY plane of the measurement system. By moving in the Z direction, the AFM tip can approach and bend the micropillar. A representation of the micropillar under the AFM tip is shown in the inset of **Figure 4.1b**. The experimental setup requires that the samples fulfil only two specific requirements: i) the stiffness of the substrate must be sufficiently high to avoid rotations at the base, ii) the position of the micropillars on the substrate must be relatively close to edges to avoid blocking of the AFM laser before reaching the Position Sensitive Photodetector (PSPD). In order to meet i), we glued the final 3D printed micropillar array to glass slides. To meet ii), we microfabricated 3D micropillars such that they were close to the edge of the polyethylene naphthalate (PEN) substrate. It should be noticed that the experimental method is versatile and can be applied to very different samples, as the requirements are not particularly stringent. Similar techniques are reported in [180] and [74], although in that case nanostructures were targeted. A detailed description of the sample treatment for bonding the slide to the substrate and the fabrication of micropillars close to the substrate edge, can be found in the Experimental Section.

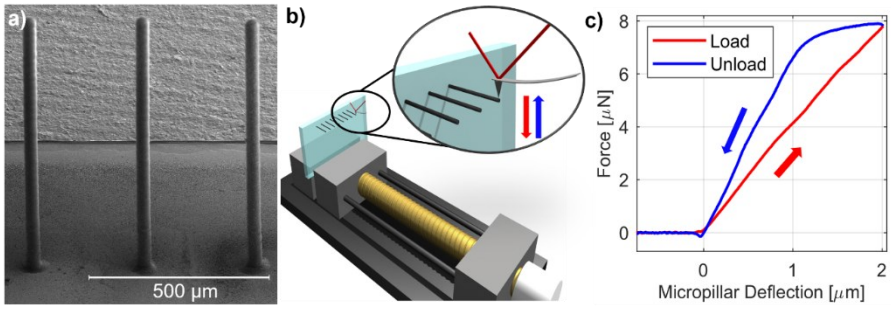

Figure 4.1. Sample and Setup. a) SEM image of PA micropillar. b) Scheme of the sample holder and the samples under the AFM tip. c) Typical Force – Micropillar Deflection curve acquired with the setup. The red and blue arrows indicate the loading and unloading curve, respectively.

The deflection of the micropillar is determined by subtracting the deflection of the AFM cantilever from the total displacement measured along the Z axis. This is valid as long as the indentation of the AFM tip into the microelectrode surface is negligible compared to the deflection of the microelectrode itself (see the Supporting Information **Figure 4.5**). A force-deflection curve obtained with our experimental setup on a metal-coated PA micropillar is shown in **Figure 4.1c**. Both the loading and unloading curves are linear in the low-force regime, however, they are characterized by different slopes. The loading and unloading curves are linked by an almost flat characteristic. To investigate the behavior in more detail and to understand its origin, we present additional measurements in **Figure 4.2**. **Figure 4.2a** shows the results obtained by repeating the force-deflection measurements for several cycles on the same micropillar. It can be observed that the pattern is independent of the number of applied cycles and no permanent deformation of the micropillar, or micropillar substrate contact, occurs. The observation demonstrates the stable clamped condition of the micropillar base to the PEN substrate. If the base was broken by mismatch of mechanical properties between the micropillar and the substrate, different cycles should show different curves due to the non-elastic process during acquisitions. Similarly, **Figure 4.2b** shows results obtained by varying the speed of the AFM probe movement. Also in this case, a very good agreement between cycles with different speed is found, thus excluding that viscous effects play a relevant role in the mechanical response of the micropillar. Finally, we performed cyclic tests with increasing force amplitudes, as reported in **Figure 4.2c**. It is found that the area

enclosed between the loading and unloading branches increases linearly with the applied force. A similar behavior has been reported and modelled by Pratt et al. in the case of cantilever-on-cantilever AFM measurements. [182] The effect was attributed to friction between the AFM tip and the bent beam and applies also to our experimental condition. Due to the friction, a force component builds up during loading, that is oriented normal to the tip axis. As a consequence, a bending moment results at the free-end of the AFM cantilever, causing its rotation. Such additional rotation leads to a modification of the laser position on the PSPD, which results in a misleading modification of the measured force.

To compensate for this effect, a correction strategy is developed based on an analytical model. The sketch reported in **Figure 4.3a** shows the sample and the AFM tip during a force spectroscopy measurement, together with the main variables of the analytical model. The model assumes that the additional bending moment due to friction is influenced not only by the cantilever tilt (θ_0), the coefficient of friction (μ), and the ratio between the tip height and the cantilever length $\left(\frac{H}{L}\right)$, but also by the stiffness of the sample (k_s). The sample stiffness is here defined as the proportionality factor existing between a concentrated force applied in a predetermined point along the micropillar height and the corresponding displacement, measured at the same point. In the model, the AFM cantilever is assumed to be characterized by the stiffness (k_p). The normal force F is linearly related to the frictional force calculated as μF.

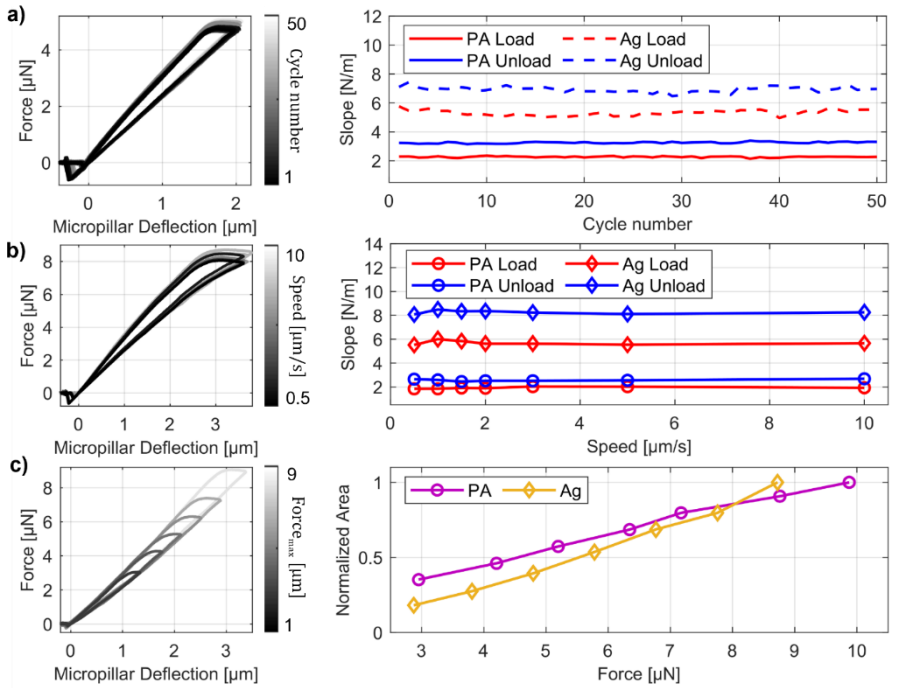

Figure 4.2. Investigation of hysteresis in force deflection curves measured on PA and Ag micropillars. a) Force-deflection curves and extracted slopes of loading and unloading for repeated measurement cycles. b) Force-deflection curves and extracted slopes of loading and unloading acquired at different loading speeds. c) Force-deflection curves and extracted hysteresis area as a function of the maximum loading force reached.

It is now worth mentioning that in AFM experiments, forces are estimated by measuring the variation of the cantilever free-end rotation (θ) while moving the tip along the z-axis (Z). Usually, the conversion from the angle θ to the force amplitude is done automatically by the instrument according to beam theory. Therefore, applying the reverse conversion to the force values provides the angle θ needed. In particular, the converting formula is given by: $\theta(Z) = \frac{3L}{k_p} F(Z)$. Under the assumptions introduced above, as detailed in [182], the slope of the $\theta(Z)$ curves, can be calculated as:

$$m_{\mp} = \frac{\Delta\theta}{\Delta Z} = \frac{3}{2L}\left(\frac{k_s(C \mp \mu D)}{k_p + k_s(A \mp \mu B)}\right) \tag{4.1}$$

where the minus sign corresponds to the loading curve, while the plus sign to the unloading curve. The dimensionless parameters A, B, C, D depend on the tilt angle θ_0 and, in particular $A = \cos^2\theta_0 - \frac{3H}{2L} cos\theta_0 sin\theta_0$, $B = cos\theta_0 sin\theta_0 + \frac{3H}{2L}\cos^2\theta_0$, $C = cos\theta_0 - \frac{2H}{L} sin\theta_0$, $D = sin\theta_0 + \frac{2H}{L} cos\theta_0$. When the slopes of the loading and unloading curves are known, **Equation 4.1** provides a system of two equations and two unknowns, which can be used to calculate μ and k_s. In particular:

$$\mu = \frac{C\left(\frac{m_+}{m_-} - 1\right)}{D\left(\frac{m_+}{m_-} + 1\right) - \frac{4}{3} LBm_+} \tag{4.2}$$

$$k_s = \frac{k_p}{\frac{3(C + \mu D)}{2Lm_+} - (A + \mu B)} \tag{4.3}$$

Once the stiffness of the sample is correctly determined, its dependence on the distance from the micropillar base can be studied. To do this, we acquired 5 force spectroscopies every 50 μm along the micropillar starting from the tip to mid-height. The results are shown in **Figure 4.3b**. Instead of stiffness, we report the compliance ($c_s = \frac{1}{k_s}$) as it allows for a better fit procedure of the measurements obtained at larger distance from the micropillar's base. The data shows an increase of compliance along the micropillar height following a cubic relationship. Such a power law is in agreement with the mechanical model of a beam with constant circular cross section according to the Euler-Bernoulli beam model. Therefore, the relationship between micropillar length and compliance is given by[104]:

$$c_s = \frac{1}{k_s} = \frac{l_{seg}^3}{3E_s I_s} \tag{4.4}$$

where I_s is the moment of inertia of the section, E_s is the elastic modulus of the sample. In the case of a circular cross section of radius *r*, the moment of inertia is given by $I_s = \frac{\pi r^4}{4}$. l_{seg} is the distance from the base of the micropillar to the point of contact between the tip and the specimen. l_{seg} thus, corresponds to the effective length of the specimen. Using **Equation 4.4**, we fit the experimental data acquired at different positions to estimate the elastic moduli. The obtained fits are reported as

dashed lines in **Figure 4.3b** and show excellent agreement with the measurement data. We note that the elastic modulus obtained in this way describes the global behavior of the micropillar and does not provide information on local variations in elastic properties as would be accessible by nanoindentation experiments. To understand the reproducibility of our measurements we analyzed for each sample type, two 3D inkjet printed micropillar arrays for a total of 16 micropillars. The model fits all the experimental data well. The table in **Figure 4.3d** shows the average values of elastic moduli and friction coefficients with standard deviations reported as measurement uncertainties. Our results show that the values of elastic moduli of micropillars are comparable with the corresponding bulk values (76 GPa for Ag, and 2-4 GPa for PA ink after curing).[183,184] Furthermore, we note that different sintering temperatures do not result in a noticeable change in the elastic moduli of the silver micropillars. In fact, the estimated values for the microfabricated samples at 100 and 150°C are comparable considering the uncertainties. Differences in the mean value of the elastic moduli might be related to an intrinsic variability from one micropillar to another, as the micropillar arrays of sintered Ag 100°C and 150°C were fabricated separately. Additionally, it must be noticed that **Equation 4.4** depends on the micropillar length cubed. Therefore, little errors in the micropillar length might result in a considerable variation of the elastic moduli. Nevertheless, these finding highlights that it is much more effective to change the micropillar length or diameter rather than the sintering temperature to tune its stiffness for the proper application. The PA and metal-coated PA samples have comparable elastic moduli. Therefore, we note that the metal coating has no significant impact on the stiffness of the sample. This is related to the fact that the thickness of the metal coating is only 150 nm while the overall diameter of the PA micropillar is 37 µm. It is therefore possible to microfabricate conductive micropillars from nonconductive inks without increasing their stiffness. **Figure 4.3e – i** show images of the morphology of different micropillars obtained by SEM and AFM in non-contact mode over areas of 10 μm^2. The images show that the surfaces of PA and metal-coated PA micropillars are visually smoother than those of Ag. This is confirmed by the friction coefficient estimated from the fit, which is lower for the case of coated and uncoated PA samples than the Ag ones. It must be noticed that metal coating, composed of 10 nm of Ni

and 150 nm of Pt, increases the roughness of the sample with respect to the uncoated samples; this is also highlighted by a slightly greater friction coefficient.

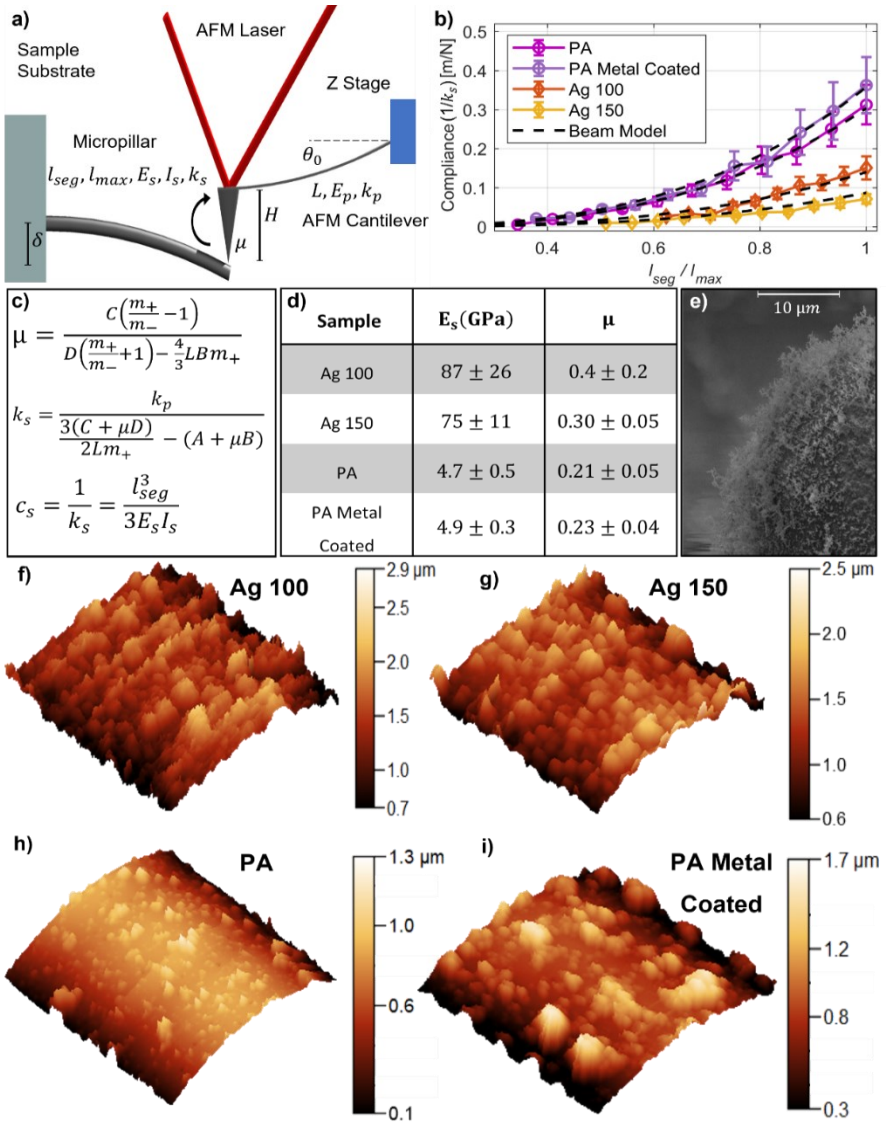

Figure 4.3. Interpretation of micropillar force deflection curves: a) The scheme reports the AFM cantilever bending a micropillar showing the main parameters of the model explaining hysteresis. b) The graph shows the measured compliance ($1/k_s$) as a function of the position of the AFM probe on the micropillar. c) Main formulas of the model. d) Elastic modulus and friction coefficient values obtained for PA, metal-coated PA, and Ag with two different sintering temperature (100 and 150°C). e) SEM image of a metal coated PA micropillar surface. f, g, h, i) AFM images (10x10 μm^2) of the side surfaces of micropillar of different materials.

4.4 CONCLUSIONS

This paper reports the characterization of elastic and frictional properties of 3D inkjet printed micropillars fabricated with different inks and post-treatment procedures. The characterization method relies on atomic force microscopy experiments that measure micropillar bending and forces at different micropillar segment lengths. To analyze the resulting stiffness data and to extract the relevant material and surface properties an analytical mechanical model is provided. The AFM method is easy to conduct, not destructive and does not require particular sample preparation. Accordingly the experiments are simpler than typical micromechanical experiments performed inside a scanning electron microscope. To correctly apply the method, two aspects must be accounted for. Firstly, it is necessary to ensure that compliance of the micropillar substrate is sufficiently small. This has been overcome by thermally bonding the substrate to a glass carrier. Secondly, it is necessary to ensure that the AFM laser is not blocked by the sample itself before reaching the PSPD. This can be easily obtained by positioning the micropillars at the edge of the sample.

The investigated micropillars were printed with different inks and parameters. One kind of samples were based on silver nanoparticles sintered at 100 and 150°C. A second kind of samples were polyacrylate micropillars with and without a metallic coating. We decided to test Ag micropillars, as they have already been used for *in vitro* applications.[148] We then tested PA micropillars, as the material has an elastic modulus lower by almost two orders of magnitude, confirming that the experimental method can also be used for less rigid materials. Our experimental findings show that all micropillars can be modelled as beams with a constant circular cross-section. The elastic moduli determined for the silver samples prepared at different sintering temperatures are comparable to each other, suggesting this does not play a major role in the mechanical properties of the micropillars. Similarly, for the case of PA samples, the coating does not provide measurable alterations of the mechanical properties, but it changes the roughness of the micropillar's surfaces. Although a significant number of micropillars were measured, relatively small standard deviations were obtained demonstrating the reproducibility of our method.

In conclusion, such measurements provide access to the mechanical properties of 3D inkjet printed micropillars employing easy to access laboratory instrumentation and well-established AFM techniques. The method allows for rapid estimation of mechanical properties, thus giving the possibility to parametrize the microfabrication steps and investigate their impact on the final device, repeatedly. This paves the way for tuning the mechanical properties of 3D printed micropillars on demand for different applications.

4.5 SUPPORTING INFORMATION

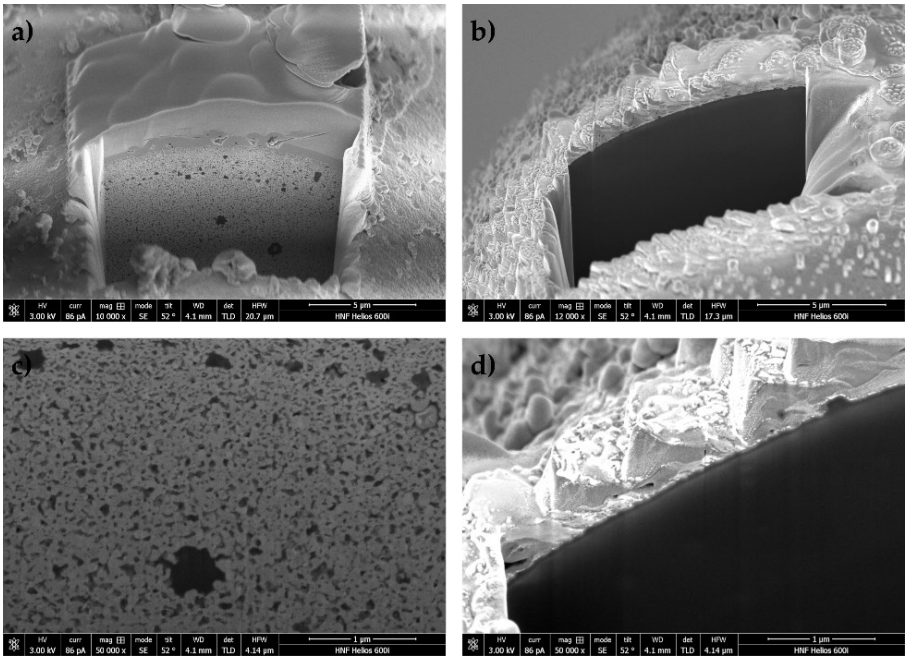

Figure 4.4. Scanning electron microscope images of focused ion beam cut a), c) 150°C sintered silver nanoparticle based and b), d) UV cured polyacrylate based micropillar. All images show the internal structure after bulk milling and polishing.

While bending a micropillar in the configuration shown in **Figure 4.1b**, there are three possible contributions to the displacement along the Z-axis: AFM cantilever deflection, micropillar deflection, and indentation of the AFM tip into the micropillar surface. The indentation is dependent on the AFM tip radius of curvature, the force applied, and the indented material. Well-established models such as the Hertz model[99] and the Oliver – Pharr model[114], describe the relationship between the material parameters and the indenter parameters. The Hertz model is usually used to investigate soft materials, while the Oliver – Pharr model is applied to data acquired on stiff materials. Our investigations on the indentation of the AFM probe into the micropillars highlight that in our case we don't need to apply any contact mechanics model to keep into account the indentation, as the indentation is negligible compared to the micropillar bending. To determine the amount of indentation, we acquired

force spectroscopies on the micropillar in a vertical configuration, to avoid any deflection of the micropillar. **Figure 4.5a** shows a sketch of the experimental setup. A typical force indentation curve acquired in this configuration on a PA micropillar is reported in **Figure 4.5b**. The graph shows that the indentation is smaller than a few nanometers, and it can be considered negligible.

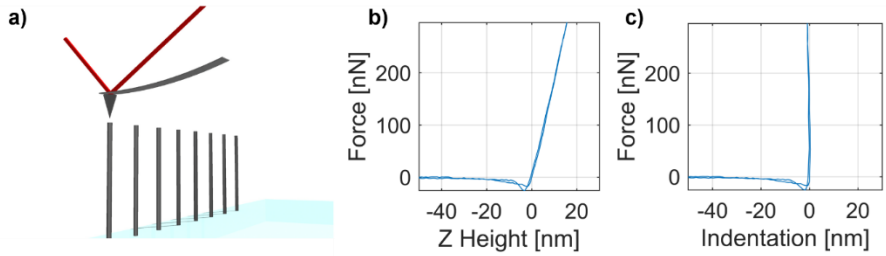

Figure 4.5. a) Scheme of the experimental setup used to estimate the indentation of the AFM tip inside the micropillar surface. b) Typical force-displacement (Z-height) curve obtained estimating the indentation on a PA micropillar. c) Typical force-indentation curve obtained subtracting in the x-axis the AFM cantilever deflection from the force-displacement plot. Note that the indentation is close to zero.

5 CONCLUSIONS

The major limitations of rigid bioelectronic interfaces are mainly due to the mismatches in mechanical properties and in chemical composition between soft biological tissues and conventional hard electronics. The mechanical mismatch between wearable or implantable devices and the target tissue can cause tissue damage and lead to device performance deterioration. Despite significant advances in flexible and stretchable bioelectronic interfaces compared to conventional rigid bioelectronic ones, there are still several mechanical aspects that need to be explored and optimized. Experimental techniques for testing mechanical properties *in situ* at the nanoscale are emerging nowadays. However, these techniques often involve the combined use of two or more instruments, thus being expensive and difficult to reproduce in other laboratories with other experimental setups. Therefore, experimental techniques are needed that are easy to access and require as little sample handling as possible. AFM is a promising candidate for determining the local mechanical properties of bioelectronic soft interfaces *in situ*, because it allows nondestructive nanoscale measurements. In addition, AFM does not require conductive samples or high vacuum condition as SEM. AFM gives the possibility to investigate the sample in air or wet condition. Furthermore, the operating principle of AFM allows simultaneous mechanical probing and sampling of the real sample topography. In this work, the need for local *in situ* experimental techniques and interpretative models has been addressed using solely AFM. The experimental method and the models have been tested and validated with the mechanical characterization of planar (metallic film on elastomer) and three-dimensional (micropillar) prototype of devices suitable for *in vivo* and *in vitro* biomedical experimentation.

Chapter 2 demonstrates how AFM indentation experiments can be performed and interpreted to investigate the nanomechanics of hard nanometer-thick metallic films on soft elastomer substrates. Such samples are of relevance for bioelectronic interfaces and have recently been used to realize stretchable bioelectronic implants with low-invasiveness due to their compliance to the mechanics of the surrounding

tissue. The thin metallic film maintains its conductivity during stretching due to the formation of a microcrack pattern. The microcracked thin film deposited on the elastomer compensates the tensile strain by bending deformations without breaking its interconnectivity. Therefore, the microcracked gold-layer can maintain its electrical conductivity yielding a stretchable conductor. By combining the mechanical nanoindentation experiments with conductive AFM, it was possible to distinguish the perforation of the conductive surface that leads to irreversible damage and conductance failure. Applying forces lower than the critical fracture force, the response is elastic and reversible. In this regime, the findings highlighted the independency of mechanical response on the indenter geometry, and the stiffness scales linearly with layer thickness. The proposed analytical model for the indentation of a hard uniform layer bonded to a soft, elastic half-space. It was shown that a linearized version of the analytical model for the indentation of a hard uniform layer bonded to a soft, elastic half-space already accounts for all the observed phenomena in the experimental parameter range. So, it allows relating the observations to mechanical material properties such as the elastic modulus and Poisson ratio of the involved materials. The finite element simulations underlined that the linearized version of the model is suitable for large mismatches in elastic moduli between the soft substrate and hard metallic thin film. For such a situation the metallic film behaves effectively as a bending plate for which it is possible to disregard local deformation under the tip. To test the proposed experimental method and the linearized model, the case of gold thermally deposited on silicone elastomer was investigated. The experimental data and the model are found in good agreement. By varying the gold layer thickness, it appears that a significant increase in layer stiffness only happens above a threshold thickness. The presence of this threshold was explained by the penetration of initial evaporated gold clusters into the polymer substrate to create a diffuse interface that delays the percolation of interfacial clusters into a continuous film. The existence of a percolation threshold was also confirmed by electrical measurements of surface conductivity that show an onset at a similar layer thickness. Once percolation is achieved, the film builds up a flexural rigidity and significant surface stiffening happens. From the quantitative analysis of the surface stiffness, the local Young's modulus of such ultrathin gold films and the threshold thickness value were estimated. Both are parameters that are crucial to

understand and predict the properties of such films once they are employed as stretchable conductors where their bending is needed to compensate for the tensile strain.

In Chapter 3, a new *in situ* experimental approach for studying the effects of strain on materials and devices for stretchable electronics was reported. This method is based on fast repetitive force spectroscopy acquisitions using a conductive AFM probe, allowing microscopic examination of morphological, mechanical, and electrical properties as a function of strain. The development was made possible by a detailed study of potential issues that can occur when dynamic AFM techniques are performed on a free-standing substrate, only attached at both ends to a tensile stretcher. By deriving and testing the analytical equations that describe substrate deflection and resonant vibrations, the experimental conditions for stable, artifact-free image acquisitions were found. Once stable measurement conditions are met, the proposed method provides a multi-channel imaging technique that can correlate morphological defects generated during tensile strain with mechanical and electrical responses. As an example, the tensile strain and conductivity changes of a thin gold layer deposited with a chromium adhesive layer on a silicon elastomer substrate were studied. With the described experimental setup, insights into the mechanism of charge transport between gold regions separated by microcracks were provided. For this reason, the combination of three imaging channels is crucial: first, the mapping of the surface height enables the identification of gold fragments surrounded by microcracks and the study of their morphological evolution during deformation. Second, the micromechanical imaging channel provides quantitative measurements of the local elastic modulus using the model described in Chapter 2. This suggests that externally applied strain is locally absorbed as microcracks propagate, whereas gold fragments do not change their tensile and stiffness physical properties with increasing strain. Third, the local conductive properties indicate that the individual gold fragments are still highly conductive, and that transport is primarily determined by the cracks that separate the conductive fragments. In the case studied here, it has been found that, even though the crack propagates in the direction perpendicular to the strain, there is still a fully conductive ohmic path. Conversely, at higher strains, the analysis of the local I-V curves reveals a transition from the ohmic to the

tunneling-dominated state, where local barriers must be overcome by a field-enhanced tunneling mechanism. Such barriers are associated with microcracks parallel to the deformation, because only in this direction the microcracks does not open significantly, leaving fragments close enough to permit tunneling transfer. The results show that charge transport occurs even when the conductive fragments are surrounded by microcracks due to tunneling, introducing a conduction mechanism not considered in previous models.

In Chapter 4 a mechanical characterization approach to investigate elastic and frictional properties of 3D inkjet printed micropillars fabricated with different inks and post-treatment procedures was demonstrated. Such conductive three-dimensional structures are of relevance for soft bioelectronic interfaces as they are prototypes of three-dimensional microelectrode arrays. Three-dimensional microelectrode arrays have been recently used in various applications for *in vivo* and *in vitro* studies, such as cellular recording, biosensors, and drug delivery. This is because three-dimensional structures allow for increased device area, spatial resolution and signal-to-noise ratio. The proposed experimental setup provide access to the mechanical properties of 3D printed micropillars employing easy-to-access laboratory instrumentation and well-established AFM techniques. The method allows for rapid estimation of mechanical properties, thus giving the possibility to parametrize the microfabrication steps and investigate their impact on the final device, repeatedly. This paves the way for tuning the mechanical properties of 3D-printed micropillars on demand for different applications. To apply the method, two requirements must be met. First, it is necessary to ensure that the compliance of the micropillar substrate is sufficiently small. This can be overcome by thermally bonding the substrate to a glass carrier. Secondly, it is necessary to ensure that the AFM laser is not blocked by the sample itself before reaching the PSPD. This can be easily obtained by positioning the microelectrodes at the edge of the sample. To test the proposed method, micropillars with different inks and parameters were printed, specifically: silver micropillars sintered at 100 and 150°C, and polyacrylate micropillars with and without a metallic coating. The experimental findings show that all microelectrodes can be modeled as beams with a constant circular cross-section. The elastic moduli determined for the silver samples prepared at different

sintering temperatures are comparable to each other, suggesting this does not play a major role in the mechanical properties of the micropillar. Similarly, in the case of PA samples, the coating does not provide measurable alterations of the mechanical properties, but it changes the roughness of the micropillar's surfaces.

In conclusion, both the nanomechanics of hard thin metallic films on soft polymeric substrates and 3D inkjet printed micropillars were investigated under different deformation states. Such planar metal-elastomer interfaces are essential for stretchable electronic devices used in next-generation wearables, implantable biocompatible sensors, soft energy harvesters, and soft robotics. 3D inkjet printed micropillars are needed in next-generation biomedical implants, cellular recording, biosensors, and drug delivery, since they are elastic, flexible, conducting 3D structures. In this work, several experimental methods supported by predictive models were demonstrated, able to provide access to the local mechanical properties. For the case study of thin-metal Au film on PDMS, the findings highlight the formation of a diffuse interface between the metal film and the polymer with an important impact on the mechanical and electrical properties. Furthermore, the proposed *in situ* multi-channel mapping method allows to observe the strain-induced transition from ohmic transport to tunneling transport in microcracked gold thin films. For the case study of 3D inkjet printed micropillars, the proposed characterization method provides rapid and precise determination of mechanical properties, thus giving the possibility to parametrize the microfabrication steps and investigate their impact on the final device. Only the development of experimental methods, such as those described in this work, will pave the way for tuning the mechanical properties of soft bioelectronic interfaces on demand for different applications, with ease to access, and fast reproducible approaches applicable to a wide range of different functional materials.

LIST OF FIGURES

Figure 1.1. Elastic moduli of target tissues, organs, and materials involved in bioelectronic interfaces. The figure is adapted from [28]. 15

Figure 1.2. Physical Sensors: a) wearable strain sensor as it looks at the macroscopic scale. The image is adapted from [51]. b) SEM image of the strain sensor to investigate the Ag nanoparticles distribution. The inset shows the cross-section of the wearable device. The image is adapted from [51]. c) Scheme of implantable sensors for blood pressure measurements, reported in [52]. 18

Figure 1.3. Electrical Sensors: a) wearable sensor for ECG recording as it looks at the macroscopic scale. The image is adapted from [54]. b) The implantable sensor for ECoG recording is shown on the left. In the center, the flexible microelectrodes array which allows sensing of the device. On the right, a scheme of the sensor implanted into the brain is depicted. The images are adapted from [57]. 20

Figure 1.4. Chemical Sensors: a) On the left the scheme of the working electrode is shown. The figure on the right shows the glucose sensor integrated into the elastic fabric. Both images are adapted from [59]. b) The first image on the left shows an EM-based subcutaneous implant glucose sensor allocated under the skin. The inset zooms into the implantable sensor. The image on the right shows how the sensor looks after the microfabrication. Both images are adapted from [61]. 21

Figure 1.5. Tensile test. a) In situ TEM holder along with a 5x10 mm MEMS chip. In an actual experiment, the MEMS chip is flipped, placed in the TEM holder, and fixed by the left and right clamps. The two SEM images on top show the working configuration of both a thin film and a nanowire. The images are adapted from [63]. b) On the left the AFM image of the diagonal region of spherulite at 10% strain is shown. The label (1) indicates craze nucleated at the boundary of stacks with different lamella orientations, while (2) labels the lamella fragmentation within a lamella stack. The images are adapted from [64]. c) AFM-in-SEM configuration for in situ nanofiber tensile test. The image on the right shows the glued nanofiber attached to the AFM probe before the acquisition. The figures are adapted form [62]. d) in situ TEM tensile testing platform of Ag NW/graphene hybrid film sample. The images are adapted from [65]. e) Image of the aluminum serpentine on a polyimide substrate. On the right, the delamination of the metal serpentine at 40% strain is shown. The images are adapted from [66]. f) FEM results with the mixed-mode cohesive zone model. For comparison, the insets show the topographic height profile measurements from the experiments at the same global stretch increment. The figures are adapted from [67]. 28

Figure 1.6. Bending test. a) SEM images of fabricated structures and AFM bending configuration. AFM images before and after the bending are reported on the right. The figure is adapted from [69]. b) On the left the electrospun nanofibers are shown. On the right, the micromechanical testing setup is reported. The hook used to apply the load to the fibers is drawn in blue. The images are adapted from [70]. c) SEM images

and corresponding schematics of Au NWs in three different configurations: free-ends (left), fixed-ends (center), and cantilevered (right). The images are adapted from [71]. d) SEM image of the nanopillars under investigation. On the right, the force spectroscopy imaging approach and the contact mode imaging method are shown, respectively. The images are adapted form [72]. e) Ultra-thin membrane under investigation and a scheme of the experimental setup with the tuning fork to measure the resonance frequencies. The figure is adapted from [73]. 31

Figure 1.7. Nanoindentation and Micropillar compression tests. a) the indentation at maximum load and the indentation after unloading, showing the trace left by the material on the tip, and used to determine the sink-in. The figure is adapted from [75]. b) Pyramidal structure before (image is at a 30° tilt) and after (taken at an 89° angle relative to the electron beam) compression. The scale bars are 200 nm. The images are adapted from [76]. c) SEM image obtained with secondary electrons (SE) with circles highlighting individual indents and SEM image obtained with backscattered electrons (BSE) indicating the material composition. On the bottom, the AFM image of the same region of the sample is shown. The AFM image allows the extraction of the profiles of the nanoindentation imprint into the sample. The images are adapted from [77]. d)Time step evolution of the micropillar compression test. The figure is adapted from [78]. 34

Figure 2.1. Nanomechanical and electrical characterization of thin gold films on elastomeric substrate. a) Scheme of the AFM experimental setup. b) Force–indentation curves on thin metal films of thickness 38 nm (Au, red) and 57 nm (Ti/Au, blue), compared to pure PDMS substrate (black). c) Height and stiffness map (128 x 128 pixel) of Au deposited on PDMS. d) Force–indentation and conductive AFM curves of PDMS/Ti/Au (40 nm thickness) with different force limits. 46

Figure 2.2. Indentation models for hard films on soft substrates: a) Scheme showing the main parameters. On the right the main equations of the model in case of indentation of a uniform layer bonded to an elastic half-space are reported. b) Calculated force-indentation curves according to the analytical solution (blue) and its linearized version (red).[105] The two curves start to diverge significantly at indentations exceeding 10 μm. The inset shows the calculated indentation curves in the experimental range of indentation. The black data correspond to the result of the FE numerical simulations. 49

Figure 2.3. Experimental validation of the indentation model: a) Force–indentation curves acquired with three different AFM tips on both pure PDMS (warm colors) and PDMS/Ti/Au (blue colors). b) Stiffness dependence on the thin film thickness. Note that the experimental data shown in **Figure 2.3b** correspond to the average of the stiffness of the loading and unloading curves. This avoids possible systematical errors due to thermal drift during the AFM acquisition. c) Comparison between the experimental indentation curves and the model predictions for PDMS/Ti/Au samples of different thickness ($h = 21$ nm, $h = 38$ nm, $h = 53$ nm). 51

Figure 2.4. Relationship between gold layer thickness and electrical properties: a, b, c) Non–Contact Mode AFM images (128 x 128 pixel) acquired on pure PDMS (a),

PDMS/Au with gold film thickness below (b) and above (c) the threshold value $h0mec$. d) Force–indentation curves of PDMS/Au with gold film thickness above and below the threshold value $h0mec$. e) Sheet resistance of samples with different film thickness. f) Qualitative representation of the effective thickness interpretation. 54

Figure 2.5. a) Stiffness map (128 x 128 pixel) on region of PDMS/Au bordering to pure PDMS region. b) Tip imprints left on the gold film by reaching the second regime during nanoindentation. 57

Figure 2.6. Finite Element Model. a) Example of vertical displacement map. Only the first 10 μm near the axis of symmetry are shown. The domain in the simulation is a square of side 50 μm. The inset shows details of the mesh in proximity to the indenter. b) Force-indentation curves obtained from numerical simulation with different indenter radii, namely 20, 100 and 400 nm.....59

Figure 3.1. Experimental design of multichannel AFM *in situ* experiments. a) Scheme of the experimental setup. The stretcher used to apply tensile strain to the sample is represented by its clamps. The electrical circuit permits to apply a bias between tip and sample to measure local currents entering the conducting AFM tip and to also measure the macroscopic sample conductivity. b) Optical microscopy image of the investigated microcracked gold layer. c) Force-indentation and current-indentation curves obtained in a single-pixel acquisition. Blue and red arrows represent the load and unload, respectively. 67

Figure 3.2. Investigation of measurement artifacts in AFM experiments on free standing stretched samples. a) Scheme of the experimental setup to measure the stretched sample's resonant frequencies. Oscillation modes are excited by sound produced at different frequencies. The response of the sample is measured with AFM in contact mode. b) Sample oscillation frequency spectra at different strains. Note that the peak corresponding to the first mode moves to the right as the strain increases. c) Peak frequency, extracted from the data in **Figure 3.2b**, as a function of strain. The red line corresponds to the analytical model. d) Power Spectral Density of forces between sample and AFM probe occurring during fast repetitive force spectroscopy acquisition. Note that tip-sample interactions occur at frequencies below the first vibration mode of the free-standing sample thus excluding possible resonant interactions. 70

Figure 3.3. *In situ* AFM multichannel acquisition. a) Morphology, stiffness, and current maps as a function of strain acquired on the same region of a microcracked gold film deposited on PDMS elastomer. The strain direction is represented by the two red arrows on the left. b) Height, stiffness, and current profiles extracted from the AFM maps. The dashed blue lines in a) indicate the positions of the profiles. 72

Figure 3.4. a) Stiffness histograms obtained from stiffness maps at different strains. The peak at lower stiffness corresponds to the PDMS, while the peak at higher stiffness corresponds to Au thin film. The dotted and dashed lines are Gaussian fit to estimate the average stiffness of PDMS and Au, respectively. b) the first graph on the

left shows the macroscopic I-V curve of the entire metallic thin film at different strains. The graph in the middle shows the microscopic I-V curve of a single gold region acquired with C-AFM at different strains. The insets report the same data in a semilogarithmic plot to show the orders of magnitude. The graph on the right shows the microscopic I-V curve not normalized and fitted with the Simmons model describing the tunneling for a metal-insulator-metal system. 75

Figure 3.5. a) Photo of the strain stage with its dimensions. b) Photo of the experimental setup with sample clamped to the strain stage under the AFM tip.....79

Figure 4.1. Sample and Setup. a) SEM image of PA micropillar. b) Scheme of the sample holder and the samples under the AFM tip. c) Typical Force – Micropillar Deflection curve acquired with the setup. The red and blue arrows indicate the loading and unloading curve, respectively. 88

Figure 4.2. Investigation of hysteresis in force deflection curves measured on PA and Ag micropillars. a) Force-deflection curves and extracted slopes of loading and unloading for repeated measurement cycles. b) Force-deflection curves and extracted slopes of loading and unloading acquired at different loading speeds. c) Force-deflection curves and extracted hysteresis area as a function of the maximum loading force reached. 90

Figure 4.3. Interpretation of micropillar force deflection curves: a) The scheme reports the AFM cantilever bending a micropillar showing the main parameters of the model explaining hysteresis. b) The graph shows the measured compliance ($1/ks$) as a function of the position of the AFM probe on the micropillar. c) Main formulas of the model. d) Elastic modulus and friction coefficient values obtained for PA, metal-coated PA, and Ag with two different sintering temperature (100 and 150°C). e) SEM image of a metal coated PA micropillar surface. f, g, h, i) AFM images (10x10 $\mu m2$) of the side surfaces of micropillar of different materials. 93

Figure 4.4. Scanning electron microscope images of focused ion beam cut a), c) 150°C sintered silver nanoparticle based and b), d) UV cured polyacrylate based micropillar. All images show the internal structure after bulk milling and polishing. 96

Figure 4.5. a) Scheme of the experimental setup used to estimate the indentation of the AFM tip inside the micropillar surface. b) Typical force-displacement (Z-height) curve obtained estimating the indentation on a PA micropillar. c) Typical force-indentation curve obtained subtracting in the x-axis the AFM cantilever deflection from the force-displacement plot. Note that the indentation is close to zero. 97

LIST OF ACRONYMS

1D	One-dimensional
2D	Two-dimensional
3D	Three-dimensional
AFM	Atomic Force Microscope
CLSM	Confocal Laser Scanning Microscope
CNTs	Carbon Nanotubes
ECG	Electrocardiography
ECoG	Electrocorticogram
EEG	Electroencephalography
EMG	Electromyography
MEMS	Microelectromechanical systems
NP	Nanoparticle
NW	Nanowire
PDMS	Poly(dimethylsiloxane)
PSPD	Position Sensitive Photo Detector
SEM	Scanning Electron Microscope
TEM	Transmission Electron Microscope

LIST OF SYMBOLS

D	Flexural rigidity
K	Stiffness
l	Characteristic length
F	Normal load
R	Radius of curvature of AFM tip
δ	Indentation
δ_{hertz}	Indentation estimated with Hertz model
δ_{flex}	Deflection of the plate
ν	Poisson's ratio
ν_{soft}	Poisson's ratio of the soft substrate
ν_{hard}	Poisson's ratio of the hard thin film
E_{soft}	Elastic modulus of the soft substrate
E	Elastic modulus
E_{hard}	Elastic modulus of the hard substrate
h	Thickness
h_0^{mec}	Mechanical thickness threshold
h_0^{el}	Electrical thickness threshold
R_s^{Au}	Sample electrical resistance
ρ^{Au}	Gold resistivity
f_0^{1st}	First resonance frequency
ε	Strain
L	Sample length
ρ	Sample density
I	Moment of inertia
$m_{\mp}$	Slopes

μ	Coefficient of friction
θ	Angle between AFM cantilever and the chip that holds it
Z	Z-Height
k_s	Sample stiffness
k_p	Probe stiffness
c_s	Sample compliance
l_{seg}	Length of the section of the micropillar under investigation
Ag	Silver
Au	Gold
InP	Indium Phosphite
Pt	Platinum

REFERENCES

(1) Chen, P.; Sun, X.; Peng, H. Emerging Soft Bioelectronics. *Adv. Funct. Mater.* **2020**, *30* (29), 1–2. https://doi.org/10.1002/adfm.202001827.

(2) Gao, D.; Parida, K.; Lee, P. S. Emerging Soft Conductors for Bioelectronic Interfaces. *Adv. Funct. Mater.* **2020**, *30* (29), 1–30. https://doi.org/10.1002/adfm.201907184.

(3) Dai, Y.; Song, Y.; Xie, J.; Xiao, G.; Li, X.; Li, Z.; Gao, F.; Zhang, Y.; He, E.; Xu, S.; Wang, Y.; Zheng, W.; Jiang, X.; Qi, Z.; Meng, D.; Fan, Z.; Cai, X. CB1-Antibody Modified Liposomes for Targeted Modulation of Epileptiform Activities Synchronously Detected by Microelectrode Arrays. *ACS Appl. Mater. Interfaces* **2020**, *12* (37), 41148–41156. https://doi.org/10.1021/acsami.0c13372.

(4) Liang, Q.; Xia, X.; Sun, X.; Yu, D.; Huang, X.; Han, G.; Mugo, S. M.; Chen, W.; Zhang, Q. Highly Stretchable Hydrogels as Wearable and Implantable Sensors for Recording Physiological and Brain Neural Signals. *Adv. Sci. (Weinheim, Baden-Wurttemberg, Ger.* **2022**, *9* (16), e2201059. https://doi.org/10.1002/advs.202201059.

(5) Heo, J. S.; Eom, J.; Kim, Y.-H.; Park, S. K. Recent Progress of Textile-Based Wearable Electronics: A Comprehensive Review of Materials, Devices, and Applications. *Small* **2018**, *14* (3), 1703034. https://doi.org/https://doi.org/10.1002/smll.201703034.

(6) Wellman, S. M.; Eles, J. R.; Ludwig, K. A.; Seymour, J. P.; Michelson, N. J.; McFadden, W. E.; Vazquez, A. L.; Kozai, T. D. Y. A Materials Roadmap to Functional Neural Interface Design. *Adv. Funct. Mater.* **2018**, *28* (12), 1701269. https://doi.org/https://doi.org/10.1002/adfm.201701269.

(7) Polikov, V. S.; Tresco, P. A.; Reichert, W. M. Response of Brain Tissue to Chronically Implanted Neural Electrodes. *J. Neurosci. Methods* **2005**, *148* (1), 1–18. https://doi.org/10.1016/j.jneumeth.2005.08.015.

(8) Chen, Y.; Rommelfanger, N. J.; Mahdi, A. I.; Wu, X.; Keene, S. T.; Obaid, A.; Salleo, A.; Wang, H.; Hong, G. How Is Flexible Electronics Advancing Neuroscience Research? *Biomaterials*. 2021, pp 120559-undefined. https://doi.org/10.1016/j.biomaterials.2020.120559.

(9) Fallegger, F.; Schiavone, G.; Lacour, S. P. Conformable Hybrid Systems for Implantable Bioelectronic Interfaces. *Adv. Mater.* **2020**, *32* (15), 1903904-undefined. https://doi.org/10.1002/adma.201903904.

(10) Amjadi, M.; Kyung, K. U.; Park, I.; Sitti, M. Stretchable, Skin-Mountable, and Wearable Strain Sensors and Their Potential Applications: A Review. *Advanced Functional Materials*. 2016, pp 1678–1698. https://doi.org/10.1002/adfm.201504755.

(11) Wu, H.; Huang, Y. A.; Xu, F.; Duan, Y.; Yin, Z. Energy Harvesters for Wearable and Stretchable Electronics: From Flexibility to Stretchability. *Advanced Materials*. 2016, pp 9881–9919. https://doi.org/10.1002/adma.201602251.

(12) Moshayedi, P.; Ng, G.; Kwok, J. C. F.; Yeo, G. S. H.; Bryant, C. E.; Fawcett, J. W.; Franze, K.; Guck, J. The Relationship between Glial Cell Mechanosensitivity and Foreign Body Reactions in the Central Nervous System. *Biomaterials* **2014**, *35* (13), 3919–3925. https://doi.org/10.1016/j.biomaterials.2014.01.038.

(13) Kang, P.-L.; Lin, Y.-H.; Settu, K.; Yen, C.-S.; Yeh, C.-Y.; Liu, J.-T.; Chen, C.-J.; Chang, S.-J. A Facile Fabrication of Biodegradable and Biocompatible Cross-Linked Gelatin as Screen Printing Substrates. *Polymers (Basel).* **2020**, *12* (5), 1186. https://doi.org/10.3390/polym12051186.

(14) Boehler, C.; Stieglitz, T.; Asplund, M. Nanostructured Platinum Grass Enables Superior Impedance Reduction for Neural Microelectrodes. *Biomaterials* **2015**, *67*, 346–353. https://doi.org/10.1016/j.biomaterials.2015.07.036.

(15) Borda, E.; Ferlauto, L.; Schleuniger, J.; Mustaccio, A.; Lütolf, F.; Lücke, A.; Fricke, S.; Marjanović, N.; Ghezzi, D. All-Printed Electrocorticography Array for In Vivo Neural Recordings. *Adv. Eng. Mater.* **2020**, *22* (3), 1901403. https://doi.org/10.1002/adem.201901403.

(16) Kireev, D.; Rincón Montes, V.; Stevanovic, J.; Srikantharajah, K.; Offenhäusser, A. N3-MEA Probes: Scooping Neuronal Networks. *Front. Neurosci.* **2019**, *13*, 320. https://doi.org/10.3389/fnins.2019.00320.

(17) Özkaya, N.; Nordin, M. Mechanical Properties of Biological Tissues BT - Fundamentals of Biomechanics: Equilibrium, Motion, and Deformation; Özkaya, N., Nordin, M., Eds.; Springer New York: New York, NY, 1999; pp 195–218. https://doi.org/10.1007/978-1-4757-3067-8_9.

(18) Ren, X.; Pei, K.; Peng, B.; Zhang, Z.; Wang, Z.; Wang, X.; Chan, P. K. L. A Low-Operating-Power and Flexible Active-Matrix Organic-Transistor Temperature-Sensor Array. *Adv. Mater.* **2016**, *28* (24), 4832–4838. https://doi.org/10.1002/adma.201600040.

(19) Lim, C. L.; Byrne, C.; Lee, J. K. Human Thermoregulation and Measurement of Body Temperature in Exercise and Clinical Settings. *Ann. Acad. Med. Singapore* **2008**, *37* (4), 347–353.

(20) Dagdeviren, C.; Shi, Y.; Joe, P.; Ghaffari, R.; Balooch, G.; Usgaonkar, K.; Gur, O.; Tran, P. L.; Crosby, J. R.; Meyer, M.; Su, Y.; Chad Webb, R.; Tedesco, A. S.; Slepian, M. J.; Huang, Y.; Rogers, J. A. Conformal Piezoelectric Systems for Clinical and Experimental Characterization of Soft Tissue Biomechanics. *Nat. Mater.* **2015**, *14* (7), 728–736. https://doi.org/10.1038/nmat4289.

(21) Wang, C.; Li, X.; Hu, H.; Zhang, L.; Huang, Z.; Lin, M.; Zhang, Z.; Yin, Z.; Huang, B.; Gong, H.; Bhaskaran, S.; Gu, Y.; Makihata, M.; Guo, Y.; Lei, Y.; Chen, Y.; Wang, C.; Li, Y.; Zhang, T.; Chen, Z.; Pisano, A. P.; Zhang, L.; Zhou, Q.; Xu, S. Monitoring of the Central Blood Pressure Waveform via a Conformal Ultrasonic Device. *Nat. Biomed. Eng.* **2018**, *2* (9), 687–695. https://doi.org/10.1038/s41551-018-0287-x.

(22) Biran, R.; Martin, D. C.; Tresco, P. A. Neuronal Cell Loss Accompanies the Brain Tissue Response to Chronically Implanted Silicon Microelectrode Arrays. *Exp. Neurol.* **2005**, *195* (1), 115–126. https://doi.org/https://doi.org/10.1016/j.expneurol.2005.04.020.

(23) Lee, H. C.; Ejserholm, F.; Gaire, J.; Currlin, S.; Schouenborg, J.; Wallman, L.; Bengtsson, M.; Park, K.; Otto, K. J. Histological Evaluation of Flexible Neural Implants; Flexibility Limit for Reducing the Tissue Response? *J. Neural Eng.* **2017**, *14* (3), 036026. https://doi.org/10.1088/1741-2552/aa68f0.

(24) Yamashita, K.; Sawahata, H.; Yamagiwa, S.; Yokoyama, S.; Numano, R.; Koida, K.; Kawano, T. A Floating 5 Mm-Diameter Needle Electrode on the Tissue for Damage-Reduced Chronic Neuronal Recording in Mice. *Lab Chip* **2022**, *22* (4), 747–756. https://doi.org/10.1039/D1LC01031J.

(25) Zang, X.; Wang, X.; Jiang, Y.; Wang, X.; Yang, Z.; Cong, J.; Chen, J.; Ji, J.; Lu, C.; Xue, M. Conducting Polymer Based Visual-Aided Smart Thermosensors on Arbitrary Substrates. *Adv. Funct. Mater.* **2017**, *27* (41), 1702706. https://doi.org/https://doi.org/10.1002/adfm.201702706.

(26) Arora, N.; Martins, D.; Ruggerio, D.; Tousimis, E.; Swistel, A. J.; Osborne, M. P.; Simmons, R. M. Effectiveness of a Noninvasive Digital Infrared Thermal Imaging System in the Detection of Breast Cancer. *Am. J. Surg.* **2008**, *196* (4), 523–526. https://doi.org/10.1016/j.amjsurg.2008.06.015.

(27) Kennedy, D. A.; Lee, T.; Seely, D. A Comparative Review of Thermography as a Breast Cancer Screening Technique. *Integr. Cancer Ther.* **2009**, *8* (1), 9–16. https://doi.org/10.1177/1534735408326171.

(28) Ray, T. R.; Choi, J.; Bandodkar, A. J.; Krishnan, S.; Gutruf, P.; Tian, L.; Ghaffari, R.; Rogers, J. A. Bio-Integrated Wearable Systems: A Comprehensive Review. *Chem. Rev.* **2019**, *119* (8), 5461–5533. https://doi.org/10.1021/acs.chemrev.8b00573.

(29) Someya, T.; Amagai, M. Toward a New Generation of Smart Skins. *Nat.*

Biotechnol. **2019**, *37* (4), 382–388. https://doi.org/10.1038/s41587-019-0079-1.

(30) Liu, Y.; Pharr, M.; Salvatore, G. A. Lab-on-Skin: A Review of Flexible and Stretchable Electronics for Wearable Health Monitoring. *ACS Nano* **2017**, *11* (10), 9614–9635. https://doi.org/10.1021/acsnano.7b04898.

(31) Yao, G.; Yin, C.; Wang, Q.; Zhang, T.; Chen, S.; Lu, C.; Zhao, K.; Xu, W.; Pan, T.; Gao, M.; Lin, Y. Flexible Bioelectronics for Physiological Signals Sensing and Disease Treatment. *J. Mater.* **2020**, *6* (2), 397–413. https://doi.org/10.1016/j.jmat.2019.12.005.

(32) Cho, K. W.; Sunwoo, S. H.; Hong, Y. J.; Koo, J. H.; Kim, J. H.; Baik, S.; Hyeon, T.; Kim, D. H. Soft Bioelectronics Based on Nanomaterials. *Chem. Rev.* **2022**, *122* (5), 5068–5143. https://doi.org/10.1021/acs.chemrev.1c00531.

(33) Chen, X.; Parida, K.; Wang, J.; Xiong, J.; Lin, M.-F.; Shao, J.; Lee, P. S. A Stretchable and Transparent Nanocomposite Nanogenerator for Self-Powered Physiological Monitoring. *ACS Appl. Mater. Interfaces* **2017**, *9* (48), 42200–42209. https://doi.org/10.1021/acsami.7b13767.

(34) Song, J.-K.; Son, D.; Kim, J.; Yoo, Y. J.; Lee, G. J.; Wang, L.; Choi, M. K.; Yang, J.; Lee, M.; Do, K.; Koo, J. H.; Lu, N.; Kim, J. H.; Hyeon, T.; Song, Y. M.; Kim, D.-H. Wearable Force Touch Sensor Array Using a Flexible and Transparent Electrode. *Adv. Funct. Mater.* **2017**, *27* (6), 1605286. https://doi.org/https://doi.org/10.1002/adfm.201605286.

(35) Guo, S.-Z.; Qiu, K.; Meng, F.; Park, S. H.; McAlpine, M. C. 3D Printed Stretchable Tactile Sensors. *Adv. Mater.* **2017**, *29* (27), 1701218. https://doi.org/https://doi.org/10.1002/adma.201701218.

(36) Lin, M.-F.; Xiong, J.; Wang, J.; Parida, K.; Lee, P. S. Core-Shell Nanofiber Mats for Tactile Pressure Sensor and Nanogenerator Applications. *Nano Energy* **2018**, *44*, 248–255. https://doi.org/https://doi.org/10.1016/j.nanoen.2017.12.004.

(37) Liu, Y.; Norton, J. J. S.; Qazi, R.; Zou, Z.; Ammann, K. R.; Liu, H.; Yan, L.; Tran, P. L.; Jang, K.-I.; Lee, J. W.; Zhang, D.; Kilian, K. A.; Jung, S. H.; Bretl, T.; Xiao, J.; Slepian, M. J.; Huang, Y.; Jeong, J.-W.; Rogers, J. A. Epidermal Mechano-Acoustic Sensing Electronics for Cardiovascular Diagnostics and Human-Machine Interfaces. *Sci. Adv.* **2016**, *2* (11), e1601185. https://doi.org/10.1126/sciadv.1601185.

(38) Boutry, C. M.; Nguyen, A.; Lawal, Q. O.; Chortos, A.; Rondeau-Gagné, S.; Bao, Z. A Sensitive and Biodegradable Pressure Sensor Array for Cardiovascular Monitoring. *Adv. Mater.* **2015**, *27* (43), 6954–6961. https://doi.org/https://doi.org/10.1002/adma.201502535.

(39) Park, M.; Do, K.; Kim, J.; Son, D.; Koo, J. H.; Park, J.; Song, J.-K.; Kim, J. H.; Lee, M.; Hyeon, T.; Kim, D.-H. Oxide Nanomembrane Hybrids with Enhanced Mechano- and Thermo-Sensitivity for Semitransparent Epidermal Electronics. *Adv. Healthc. Mater.* **2015**, *4* (7), 992–997. https://doi.org/https://doi.org/10.1002/adhm.201500097.

(40) Choi, M. K.; Park, I.; Kim, D. C.; Joh, E.; Park, O. K.; Kim, J.; Kim, M.; Choi, C.; Yang, J.; Cho, K. W.; Hwang, J.-H.; Nam, J.-M.; Hyeon, T.; Kim, J. H.; Kim, D.-H. Thermally Controlled, Patterned Graphene Transfer Printing for Transparent and Wearable Electronic/Optoelectronic System. *Adv. Funct. Mater.* **2015**, *25* (46), 7109–7118. https://doi.org/https://doi.org/10.1002/adfm.201502956.

(41) Fiorillo, A. S.; Critello, C. D.; Pullano, S. A. Theory, Technology and Applications of Piezoresistive Sensors: A Review. *Sensors Actuators A Phys.* **2018**, *281*, 156–175. https://doi.org/https://doi.org/10.1016/j.sna.2018.07.006.

(42) Zhu, S.-E.; Krishna Ghatkesar, M.; Zhang, C.; Janssen, G. C. A. M. Graphene Based Piezoresistive Pressure Sensor. *Appl. Phys. Lett.* **2013**, *102* (16), 161904. https://doi.org/10.1063/1.4802799.

(43) Huang, C.-T.; Shen, C.-L.; Tang, C.-F.; Chang, S.-H. A Wearable Yarn-Based Piezo-Resistive Sensor. *Sensors Actuators A Phys.* **2008**, *141* (2),

396–403. https://doi.org/https://doi.org/10.1016/j.sna.2007.10.069.

(44) Tzou, H. S.; Tseng, C. I. Distributed Piezoelectric Sensor/Actuator Design for Dynamic Measurement/Control of Distributed Parameter Systems: A Piezoelectric Finite Element Approach. *J. Sound Vib.* **1990**, *138* (1), 17–34. https://doi.org/https://doi.org/10.1016/0022-460X(90)90701-Z.

(45) Ng, T. H.; Liao, W. H. Sensitivity Analysis and Energy Harvesting for a Self-Powered Piezoelectric Sensor. *J. Intell. Mater. Syst. Struct.* **2005**, *16* (10), 785–797. https://doi.org/10.1177/1045389X05053151.

(46) Ihn, J.-B.; Chang, F.-K. Detection and Monitoring of Hidden Fatigue Crack Growth Using a Built-in Piezoelectric Sensor/Actuator Network: I. Diagnostics. *Smart Mater. Struct.* **2004**, *13* (3), 609–620. https://doi.org/10.1088/0964-1726/13/3/020.

(47) Rajala, S.; Siponkoski, T.; Sarlin, E.; Mettänen, M.; Vuoriluoto, M.; Pammo, A.; Juuti, J.; Rojas, O. J.; Franssila, S.; Tuukkanen, S. Cellulose Nanofibril Film as a Piezoelectric Sensor Material. *ACS Appl. Mater. Interfaces* **2016**, *8* (24), 15607–15614. https://doi.org/10.1021/acsami.6b03597.

(48) Senthil Kumar, K.; Xu, Z.; Sivaperuman Kalairaj, M.; Ponraj, G.; Huang, H.; Ng, C.-F.; Wu, Q. H.; Ren, H. Stretchable Capacitive Pressure Sensing Sleeve Deployable onto Catheter Balloons towards Continuous Intra-Abdominal Pressure Monitoring. *Biosensors* **2021**, *11* (5). https://doi.org/10.3390/bios11050156.

(49) Thouti, E.; Chauhan, K.; Prajesh, R.; Farman, M.; Maurya, R. K.; Sharma, P.; Nagaraju, A. Flexible Capacitive Pressure Sensors Using Microdome like Structured Polydimethylsiloxane Dielectric Layers. *Sensors Actuators A Phys.* **2022**, *335*, 113393. https://doi.org/https://doi.org/10.1016/j.sna.2022.113393.

(50) Zhang, S.; Zhang, H.; Yao, G.; Liao, F.; Gao, M.; Huang, Z.; Li, K.; Lin, Y. Highly Stretchable, Sensitive, and Flexible Strain Sensors Based on Silver

Nanoparticles/Carbon Nanotubes Composites. *J. Alloys Compd.* **2015**, *652*, 48–54. https://doi.org/https://doi.org/10.1016/j.jallcom.2015.08.187.

(51) Ruhhammer, J.; Herbstritt, T.; Ruh, D.; Foerster, K.; Heilmann, C.; Beyersdorf, F.; Goldschmidtboeing, F.; Seifert, A.; Woias, P. Magnetic Sensor for Arterial Distension and Blood Pressure Monitoring. *Biomed. Microdevices* **2014**, *16* (6), 815–827. https://doi.org/10.1007/s10544-014-9885-x.

(52) Yuk, H.; Lu, B.; Zhao, X. Hydrogel Bioelectronics. *Chem. Soc. Rev.* **2019**, *48* (6), 1642–1667. https://doi.org/10.1039/C8CS00595H.

(53) Dong, W.; Cheng, X.; Xiong, T.; Wang, X. Stretchable Bio-Potential Electrode with Self-Similar Serpentine Structure for Continuous, Long-Term, Stable ECG Recordings. *Biomed. Microdevices* **2019**, *21* (1), 6. https://doi.org/10.1007/s10544-018-0353-x.

(54) Viventi, J.; Kim, D.-H.; Vigeland, L.; Frechette, E. S.; Blanco, J. A.; Kim, Y.-S.; Avrin, A. E.; Tiruvadi, V. R.; Hwang, S.-W.; Vanleer, A. C.; Wulsin, D. F.; Davis, K.; Gelber, C. E.; Palmer, L.; Van der Spiegel, J.; Wu, J.; Xiao, J.; Huang, Y.; Contreras, D.; Rogers, J. A.; Litt, B. Flexible, Foldable, Actively Multiplexed, High-Density Electrode Array for Mapping Brain Activity in Vivo. *Nat. Neurosci.* **2011**, *14* (12), 1599–1605. https://doi.org/10.1038/nn.2973.

(55) Decataldo, F.; Cramer, T.; Martelli, D.; Gualandi, I.; Korim, W. S.; Yao, S. T.; Tessarolo, M.; Murgia, M.; Scavetta, E.; Amici, R.; Fraboni, B. Stretchable Low Impedance Electrodes for Bioelectronic Recording from Small Peripheral Nerves. *Sci. Rep.* **2019**, *9* (1). https://doi.org/10.1038/s41598-019-46967-2.

(56) Chang, S.-I.; Park, S.-Y.; Yoon, E. Minimally-Invasive Neural Interface for Distributed Wireless Electrocorticogram Recording Systems. *Sensors*. 2018. https://doi.org/10.3390/s18010263.

(57) Schuhmann, T. G. J.; Zhou, T.; Hong, G.; Lee, J. M.; Fu, T.-M.; Park, H.-

G.; Lieber, C. M. Syringe-Injectable Mesh Electronics for Stable Chronic Rodent Electrophysiology. *J. Vis. Exp.* **2018**, No. 137. https://doi.org/10.3791/58003.

(58) Khodagholy, D.; Gelinas, J. N.; Thesen, T.; Doyle, W.; Devinsky, O.; Malliaras, G. G.; Buzsáki, G. NeuroGrid: Recording Action Potentials from the Surface of the Brain. *Nat. Neurosci.* **2015**, *18* (2), 310–315. https://doi.org/10.1038/nn.3905.

(59) Tybrandt, K.; Khodagholy, D.; Dielacher, B.; Stauffer, F.; Renz, A. F.; Buzsáki, G.; Vörös, J. High-Density Stretchable Electrode Grids for Chronic Neural Recording. *Adv. Mater.* **2018**, *30* (15), e1706520. https://doi.org/10.1002/adma.201706520.

(60) Heikenfeld, J.; Jajack, A.; Rogers, J.; Gutruf, P.; Tian, L.; Pan, T.; Li, R.; Khine, M.; Kim, J.; Wang, J.; Kim, J. Wearable Sensors: Modalities, Challenges, and Prospects. *Lab Chip* **2018**, *18* (2), 217–248. https://doi.org/10.1039/c7lc00914c.

(61) Shu, Y.; Su, T.; Lu, Q.; Shang, Z.; Xu, Q.; Hu, X. Highly Stretchable Wearable Electrochemical Sensor Based on Ni-Co MOF Nanosheet-Decorated Ag/RGO/PU Fiber for Continuous Sweat Glucose Detection. *Anal. Chem.* **2021**, *93* (48), 16222–16230. https://doi.org/10.1021/acs.analchem.1c04106.

(62) Kar, A.; Ahamad, N.; Dewani, M.; Awasthi, L.; Patil, R.; Banerjee, R. Wearable and Implantable Devices for Drug Delivery: Applications and Challenges. *Biomaterials* **2022**, *283*, 121435. https://doi.org/10.1016/j.biomaterials.2022.121435.

(63) Kim, S.; Malik, J.; Seo, J. M.; Cho, Y. M.; Bien, F. Subcutaneously Implantable Electromagnetic Biosensor System for Continuous Glucose Monitoring. *Sci. Rep.* **2022**, *12* (1), 17395. https://doi.org/10.1038/s41598-022-22128-w.

(64) Hang, F.; Lu, D.; Bailey, R. J.; Jimenez-Palomar, I.; Stachewicz, U.;

Cortes-Ballesteros, B.; Davies, M.; Zech, M.; Bödefeld, C.; Barber, A. H. In Situ Tensile Testing of Nanofibers by Combining Atomic Force Microscopy and Scanning Electron Microscopy. *Nanotechnology* **2011**, *22* (36). https://doi.org/10.1088/0957-4484/22/36/365708.

(65) Zhu, Y.; Espinosa, H. D. An Electromechanical Material Testing System for in Situ Electron Microscopy and Applications. *Proc. Natl. Acad. Sci. U. S. A.* **2005**, *102* (41), 14503–14508. https://doi.org/10.1073/pnas.0506544102.

(66) Thomas, C.; Ferreiro, V.; Coulon, G.; Seguela, R. In Situ AFM Investigation of Crazing in Polybutene Spherulites under Tensile Drawing. *Polymer (Guildf).* **2007**, *48* (20), 6041–6048. https://doi.org/10.1016/j.polymer.2007.07.062.

(67) Cao, K.; Yang, H.; Gao, L.; Han, Y.; Feng, J.; Yang, H.; Zhang, H.; Wang, W.; Lu, Y. In Situ Mechanical Characterization of Silver Nanowire/Graphene Hybrids Films for Flexible Electronics. *Int. J. Smart Nano Mater.* **2020**, *11* (3), 265–276. https://doi.org/10.1080/19475411.2020.1790056.

(68) Cattarinuzzi, E.; Lucchini, R.; Gastaldi, D.; Vena, P.; Adami, A.; Lorenzelli, L. Design of Aluminum/Polyimide Stretchable Interconnects Investigated through in-Situ Testing. *Proc. 2015 18th AISEM Annu. Conf. AISEM 2015* **2015**, 28–31. https://doi.org/10.1109/AISEM.2015.7066784.

(69) Kleinendorst, S. M.; Fleerakkers, R.; Cattarinuzzi, E.; Vena, P.; Gastaldi, D.; van Maris, M. P. F. H. L.; Hoefnagels, J. P. M. Micron-Scale Experimental-Numerical Characterization of Metal-Polymer Interface Delamination in Stretchable Electronics Interconnects. *Int. J. Solids Struct.* **2020**, *204–205*, 52–64. https://doi.org/10.1016/j.ijsolstr.2020.08.011.

(70) Zhu, T. T.; Bushby, A. J.; Dunstan, D. J. Materials Mechanical Size Effects: A Review. *Mater. Technol.* **2008**, *23* (4), 193–209. https://doi.org/10.1179/175355508X376843.

(71) Kim, Y. J.; Son, K.; Choi, I. C.; Choi, I. S.; Park, W. Il; Jang, J. Il. Exploring Nanomechanical Behavior of Silicon Nanowires: AFM Bending versus Nanoindentation. *Adv. Funct. Mater.* **2011**, *21* (2), 279–286. https://doi.org/10.1002/adfm.201001471.

(72) Morel, A.; Domaschke, S.; Urundolil Kumaran, V.; Alexeev, D.; Sadeghpour, A.; Ramakrishna, S. N.; Ferguson, S. J.; Rossi, R. M.; Mazza, E.; Ehret, A. E.; Fortunato, G. Correlating Diameter, Mechanical and Structural Properties of Poly(L-Lactide) Fibres from Needleless Electrospinning. *Acta Biomater.* **2018**, *81*, 169–183. https://doi.org/10.1016/j.actbio.2018.09.055.

(73) Antsov, M.; Polyakov, B.; Zadin, V.; Mets, M.; Oras, S.; Vahtrus, M.; Lõhmus, R.; Dorogin, L.; Vlassov, S. Mechanical Characterisation of Pentagonal Gold Nanowires in Three Different Test Configurations: A Comparative Study. *Micron* **2019**, *124* (February). https://doi.org/10.1016/j.micron.2019.102686.

(74) Angeloni, L.; Ganjian, M.; Nouri-Goushki, M.; Mirzaali, M. J.; Hagen, C. W.; Zadpoor, A. A.; Fratila-Apachitei, L. E.; Ghatkesar, M. K. Mechanical Characterization of Nanopillars by Atomic Force Microscopy. *Addit. Manuf.* **2021**, *39*, 101858. https://doi.org/10.1016/j.addma.2021.101858.

(75) Abrahamians, J. O.; Sauvet, B.; Polesel-Maris, J.; Braive, R.; Régnier, S. A Nanorobotic System for in Situ Stiffness Measurements on Membranes. *IEEE Trans. Robot.* **2014**, *30* (1), 119–124. https://doi.org/10.1109/TRO.2013.2280831.

(76) Schuh, C. A. Nanoindentation Studies of Materials. *Mater. Today* **2006**, *9* (5), 32–40. https://doi.org/https://doi.org/10.1016/S1369-7021(06)71495-X.

(77) Guillonneau, G.; Wheeler, J. M.; Wehrs, J.; Philippe, L.; Baral, P.; Höppel, H. W.; Göken, M.; Michler, J. Determination of the True Projected Contact Area by in Situ Indentation Testing. *J. Mater. Res.* **2019**, *34* (24), 4086. https://doi.org/10.1557/jmr.2019.310.

(78) Lewis, B. B.; Mound, B. A.; Srijanto, B.; Fowlkes, J. D.; Pharr, G. M.; Rack, P. D. Growth and Nanomechanical Characterization of Nanoscale 3D Architectures Grown: Via Focused Electron Beam Induced Deposition. *Nanoscale* **2017**, *9* (42), 16349–16356. https://doi.org/10.1039/c7nr05274j.

(79) Novotna, V.; Horak, J.; Konecny, M.; Hegrova, V.; Novotny, O.; Novacek, Z.; Neuman, J. AFM-in-SEM as a Tool for Comprehensive Sample Surface Analysis. *Micros. Today* **2020**, *28* (3), 38–46. https://doi.org/DOI: 10.1017/S1551929520000875.

(80) Jun, T.-S.; Sernicola, G.; Dunne, F. P. E.; Britton, T. B. Local Deformation Mechanisms of Two-Phase Ti Alloy. *Mater. Sci. Eng. A* **2016**, *649*, 39–47. https://doi.org/https://doi.org/10.1016/j.msea.2015.09.016.

(81) Park Systems Corporation. Nx10 User ' S Manual. **2015**.

(82) Voigtländer, B. *Atomic Force Microscopy Designs*; 2019. https://doi.org/10.1007/978-3-030-13654-3_4.

(83) Kim, D. H.; Rogers, J. A. Stretchable Electronics: Materials Strategies and Devices. *Adv. Mater.* **2008**, *20* (24), 4887–4892. https://doi.org/10.1002/adma.200801788.

(84) Kim, D. C.; Shim, H. J.; Lee, W.; Koo, J. H.; Kim, D. H. Material-Based Approaches for the Fabrication of Stretchable Electronics. *Advanced Materials*. 2020, pp 1902743-undefined. https://doi.org/10.1002/adma.201902743.

(85) Qi, D.; Zhang, K.; Tian, G.; Jiang, B.; Huang, Y. Stretchable Electronics Based on PDMS Substrates. *Adv. Mater.* **2020**, *33* (6). https://doi.org/10.1002/adma.202003155.

(86) Angeli, M. A. C.; Cramer, T.; Fraboni, B.; Magagnin, L.; Gastaldi, D.; Vena, P. Reliability of Inkjet Printed Silver Nanoparticle Interconnects on Deformable Substrates Tested through an Electromechanical In-Situ Technique. *MRS Commun.* **2019**, *9* (1), 129–136. https://doi.org/10.1557/mrc.2019.10.

(87) Harris, K. D.; Elias, A. L.; Chung, H. J. Flexible Electronics under Strain: A Review of Mechanical Characterization and Durability Enhancement Strategies. *Journal of Materials Science*. 2016, pp 2771–2805. https://doi.org/10.1007/s10853-015-9643-3.

(88) Shyu, T. C.; Damasceno, P. F.; Dodd, P. M.; Lamoureux, A.; Xu, L.; Shlian, M.; Shtein, M.; Glotzer, S. C.; Kotov, N. A. A Kirigami Approach to Engineering Elasticity in Nanocomposites through Patterned Defects. *Nat. Mater.* **2015**, *14* (8), 785–789. https://doi.org/10.1038/nmat4327.

(89) Guo, C. F.; Liu, Q.; Wang, G.; Wang, Y.; Shi, Z.; Suo, Z.; Chu, C. W.; Ren, Z. Fatigue-Free, Superstretchable, Transparent, and Biocompatible Metal Electrodes. *Proc. Natl. Acad. Sci. U. S. A.* **2015**, *112* (40), 12332–12337. https://doi.org/10.1073/pnas.1516873112.

(90) Zhou, C.; Bette, S.; Schnakenberg, U. Flexible and Stretchable Gold Microstructures on Extra Soft Poly(Dimethylsiloxane) Substrates. *Adv. Mater.* **2015**, *27* (42), 6664–6669. https://doi.org/10.1002/adma.201502630.

(91) Kim, S.; Geryak, R. D.; Zhang, S.; Ma, R.; Calabrese, R.; Kaplan, D. L.; Tsukruk, V. V. Interfacial Shear Strength and Adhesive Behavior of Silk Ionomer Surfaces. *Biomacromolecules* **2017**, *18* (9), 2876–2886. https://doi.org/10.1021/acs.biomac.7b00790.

(92) Xie, L.; Cui, X.; Liu, J.; Lu, Q.; Huang, J.; Mao, X.; Yang, D.; Tan, J.; Zhang, H.; Zeng, H. Nanomechanical Insights into Versatile Polydopamine Wet Adhesive Interacting with Liquid-Infused and Solid Slippery Surfaces. *ACS Appl. Mater. Interfaces* **2021**, *13* (5), 6941–6950. https://doi.org/10.1021/acsami.0c22073.

(93) Gisbert, V. G.; Benaglia, S.; Uhlig, M. R.; Proksch, R.; Garcia, R. High-Speed Nanomechanical Mapping of the Early Stages of Collagen Growth by Bimodal Force Microscopy. *ACS Nano* **2021**, *15* (1), 1850–1857. https://doi.org/10.1021/acsnano.0c10159.

(94) Garcia, R. Nanomechanical Mapping of Soft Materials with the Atomic

Force Microscope: Methods, Theory and Applications. *Chem. Soc. Rev.* **2020**, *49* (16), 5850–5884. https://doi.org/10.1039/d0cs00318b.

(95) Hsueh, C. H.; Miranda, P. Master Curves for Hertzian Indentation on Coating/Substrate Systems. *J. Mater. Res.* **2004**, *19* (1), 9-undefined. https://doi.org/10.1557/jmr.2004.19.1.94.

(96) Sarrazin, B.; Brossard, R.; Guenoun, P.; Malloggi, F. Investigation of PDMS Based Bi-Layer Elasticity via Interpretation of Apparent Young's Modulus. *Soft Matter* **2016**, *12* (7), 2200–2207. https://doi.org/10.1039/c5sm02133b.

(97) Doss, B. L.; Eliato, K. R.; hui Lin, K.; Ros, R. Quantitative Mechanical Analysis of Indentations on Layered, Soft Elastic Materials. *Soft Matter* **2019**, *15* (8), 1776–1784. https://doi.org/10.1039/c8sm02121j.

(98) Johnson, K. L. *Contact Mechanics*; Cambridge University Press, 1985.

(99) Hertz, H. On the Contact of Elastic Solids. *Z. Reine Angew. Math.* **1881**, *92*, 156–171.

(100) Cripps, A. C. F.-. *Nanoindentation*, Springer.; 2011.

(101) Perriot, A.; Barthel, E. Elastic Contact to a Coated Half-Space: Effective Elastic Modulus and Real Penetration. *J. Mater. Res.* **2004**, *19* (2), 600–608. https://doi.org/10.1557/jmr.2004.19.2.600.

(102) Alaboodi, A. S.; Hussain, Z. Finite Element Modeling of Nano-Indentation Technique to Characterize Thin Film Coatings. *Journal of King Saud University - Engineering Sciences*. 2019, pp 61–69. https://doi.org/10.1016/j.jksues.2017.02.001.

(103) Chiodini, S.; Ruiz-Rincón, S.; Garcia, P. D.; Martin, S.; Kettelhoit, K.; Armenia, I.; Werz, D. B.; Cea, P. Bottom Effect in Atomic Force Microscopy Nanomechanics. *Small* **2020**, *16* (35), 2000269-undefined. https://doi.org/10.1002/smll.202000269.

(104) Timoshenko, S. P.; Woinowsky-Krieger, S. *Theory of Plates and Shells*,

2nd ed.; McGraw-Hill, Ed.; 1959.

(105) Popov, G. I. Bending of a Semi-Infinite Plate Resting on a Linearly Deformable Foundation. *J. Appl. Math. Mech.* **1961**, *25* (2), 502–520. https://doi.org/10.1016/0021-8928(61)90082-X.

(106) Argatov, I. I.; Sabina, F. J. Small-Scale Indentation of an Elastic Coated Half-Space: The Effect of Compliant Substrate. *Int. J. Eng. Sci.* **2016**, *104*, 87–96. https://doi.org/10.1016/j.ijengsci.2016.04.008.

(107) Lee, D.; Barber, J. R.; Thouless, M. D. Indentation of an Elastic Half Space with Material Properties Varying with Depth. *Int. J. Eng. Sci.* **2009**, *47* (11–12). https://doi.org/10.1016/j.ijengsci.2008.08.005.

(108) Minev, I. R.; Musienko, P.; Hirsch, A.; Barraud, Q.; Wenger, N.; Moraud, E. M.; Gandar, J.; Capogrosso, M.; Milekovic, T.; Asboth, L.; Torres, R. F.; Vachicouras, N.; Liu, Q.; Pavlova, N.; Duis, S.; Larmagnac, A.; Vörös, J.; Micera, S.; Suo, Z.; Courtine, G.; Lacour, S. P. Electronic Dura Mater for Long-Term Multimodal Neural Interfaces. *Science (80-.).* **2015**, *347* (6218), 159–163. https://doi.org/10.1126/science.1260318.

(109) Lacour, S. P.; Wagner, S.; Huang, Z.; Suo, Z. Stretchable Gold Conductors on Elastomeric Substrates. *Appl. Phys. Lett.* **2003**, *82* (15). https://doi.org/10.1063/1.1565683.

(110) Zhu, B.; Gong, S.; Cheng, W. Softening Gold for Elastronics. *Chemical Society Reviews*. 2019, pp 1668–1711. https://doi.org/10.1039/c8cs00609a.

(111) Lacour, S. P.; Chan, D.; Wagner, S.; Li, T.; Suo, Z. Mechanisms of Reversible Stretchability of Thin Metal Films on Elastomeric Substrates. *Appl. Phys. Lett.* **2006**, *88* (20), 204103. https://doi.org/10.1063/1.2201874.

(112) der Pauw, L. Van. A Method for Measure Specific Resistivity and Hall Effect of Discs of Arbitrary Shape. *Philips Res. Reports* **1958**, *13*, 1–9.

(113) Kinder, R.; Mikolášek, M.; Donoval, D.; Kováč, J.; Tlaczala, M. Measurement System with Hall and a Four Point Probes for

Characterization of Semiconductors. *J. Electr. Eng.* **2013**, *64* (2), 106–111. https://doi.org/10.2478/jee-2013-0015.

(114) Oliver, W. C.; Pharr, G. M. An Improved Technique for Determining Hardness and Elastic Modulus Using Load and Displacement Sensing Indentation Experiments. *J. Mater. Res.* **1992**, *7* (6), 1564–1583. https://doi.org/10.1557/jmr.1992.1564.

(115) Graudejus, O.; Görrn, P.; Wagner, S. Controlling the Morphology of Gold Films on Poly(Dimethylsiloxane). *ACS Appl. Mater. Interfaces* **2010**, *2* (7), 1927–1933. https://doi.org/10.1021/am1002537.

(116) Cordill, M. J.; Glushko, O.; Kreith, J.; Marx, V. M.; Kirchlechner, C. Measuring Electro-Mechanical Properties of Thin Films on Polymer Substrates. *Microelectron. Eng.* **2015**, *137* (1). https://doi.org/10.1016/j.mee.2014.08.002.

(117) Mohri, M.; Nili-Ahmadabadi, M.; PouryazdanPanah, M.; Hahn, H. Evaluation of Structure and Mechanical Properties of Ni-Rich NiTi/Kapton Composite Film. *Mater. Sci. Eng. A* **2016**, *668*. https://doi.org/10.1016/j.msea.2016.05.044.

(118) Kleinbichler, A.; Bartosik, M.; Völker, B.; Cordill, M. J. Thin Film Adhesion of Flexible Electronics Influenced by Interlayers. *Adv. Eng. Mater.* **2017**, *19* (4). https://doi.org/10.1002/adem.201600665.

(119) Lang, U.; Süss, T.; Wojtas, N.; Dual, J. Novel Method for Analyzing Crack Growth in Polymeric Microtensile Specimens by in Situ Atomic Force Microscopy. *Exp. Mech.* **2010**, *50* (4). https://doi.org/10.1007/s11340-009-9240-y.

(120) Li, X.; Sun, M.; Shan, C.; Chen, Q.; Wei, X. Mechanical Properties of 2D Materials Studied by In Situ Microscopy Techniques. *Adv. Mater. Interfaces* **2018**, *5* (5). https://doi.org/10.1002/admi.201701246.

(121) Roy, S.; Ryan, J.; Webster, S.; Nepal, D. A Review of in Situ Mechanical Characterization of Polymer Nanocomposites: Prospect and Challenges.

Appl. Mech. Rev. **2017**, *69* (5). https://doi.org/10.1115/1.4038257.

(122) Haque, M. A.; Saif, M. T. A. In Situ Tensile Testing of Nanoscale Freestanding Thin Films inside a Transmission Electron Microscope. *J. Mater. Res.* **2005**, *20* (7). https://doi.org/10.1557/JMR.2005.0220.

(123) Bobji, M. S.; Bhushan, B. In Situ Microscopic Surface Characterization Studies of Polymeric Thin Films during Tensile Deformation Using Atomic Force Microscopy. *J. Mater. Res.* **2001**, *16* (3). https://doi.org/10.1557/JMR.2001.0110.

(124) Godard, P.; Renault, P. O.; Faurie, D.; Thiaudière, D. Relaxation Mechanisms in a Gold Thin Film on a Compliant Substrate as Revealed by X-Ray Diffraction. *Appl. Phys. Lett.* **2017**, *110* (21). https://doi.org/10.1063/1.4984135.

(125) Godard, P.; Faurie, D.; Renault, P. O. Strain Ratio Effects in Mechanical Properties of Supported Thin Films. *J. Appl. Phys.* **2020**, *127* (10). https://doi.org/10.1063/1.5133715.

(126) Li, X.; Xu, W.; Sutton, M. A.; Mello, M. In Situ Nanoscale In-Plane Deformation Studies of Ultrathin Polymeric Films during Tensile Deformation Using Atomic Force Microscopy and Digital Image Correlation Techniques. *IEEE Trans. Nanotechnol.* **2007**, *6* (1). https://doi.org/10.1109/TNANO.2006.888527.

(127) Cramer, T.; Travaglini, L.; Lai, S.; Patruno, L.; De Miranda, S.; Bonfiglio, A.; Cosseddu, P.; Fraboni, B. Direct Imaging of Defect Formation in Strained Organic Flexible Electronics by Scanning Kelvin Probe Microscopy. *Sci. Rep.* **2016**, *6* (September). https://doi.org/10.1038/srep38203.

(128) Kleinbichler, A.; Pfeifenberger, M. J.; Zechner, J.; Moody, N. R.; Bahr, D. F.; Cordill, M. J. New Insights into Nanoindentation-Based Adhesion Testing. *Jom* **2017**, *69* (11). https://doi.org/10.1007/s11837-017-2496-2.

(129) Zhong, J.; He, D. Combination of Universal Mechanical Testing Machine

with Atomic Force Microscope for Materials Research. *Sci. Rep.* **2015**, *5* (August). https://doi.org/10.1038/srep12998.

(130) Renault, P. O.; Villain, P.; Coupeau, C.; Goudeau, P.; Badawi, K. F. Damage Mode Tensile Testing of Thin Gold Films on Polyimide Substrates by X-Ray Diffraction and Atomic Force Microscopy. *Thin Solid Films* **2003**, *424* (2). https://doi.org/10.1016/S0040-6090(02)01127-6.

(131) Glushko, O.; Kraker, P.; Cordill, M. J. Explicit Relationship between Electrical and Topological Degradation of Polymer-Supported Metal Films Subjected to Mechanical Loading. *Appl. Phys. Lett.* **2017**, *110* (19). https://doi.org/10.1063/1.4982802.

(132) Glushko, O.; Putz, B.; Cordill, M. J. Determining Effective Crack Lengths from Electrical Measurements in Polymer-Supported Thin Films. *Thin Solid Films* **2020**, *699* (August 2019). https://doi.org/10.1016/j.tsf.2020.137906.

(133) Matsuhisa, N.; Chen, X.; Bao, Z.; Someya, T. Materials and Structural Designs of Stretchable Conductors. *Chemical Society Reviews*. 2019. https://doi.org/10.1039/c8cs00814k.

(134) Lacour, S. P.; Wagner, S.; Huang, Z.; Suo, Z. Stretchable Gold Conductors on Elastomeric Substrates. *Appl. Phys. Lett.* **2003**, *82* (15). https://doi.org/10.1063/1.1565683.

(135) Cortelli, G.; Patruno, L.; Cramer, T.; Murgia, M.; Fraboni, B.; De Miranda, S. Atomic Force Microscopy Nanomechanics of Hard Nanometer-Thick Films on Soft Substrates: Insights into Stretchable Conductors. *ACS Appl. Nano Mater.* **2021**, *4* (8). https://doi.org/10.1021/acsanm.1c01590.

(136) Clough, R. W.; Penzien, J. *Dynamics of Structures*; 2002.

(137) Graudejus, O.; Li, T.; Cheng, J.; Keiper, N.; Ponce Wong, R. D.; Pak, A. B.; Abbas, J. The Effects of Bending on the Resistance of Elastically Stretchable Metal Conductors, and a Comparison with Stretching. *Appl. Phys. Lett.* **2017**, *110* (22). https://doi.org/10.1063/1.4984207.

(138) Dubois, V.; Raja, S. N.; Gehring, P.; Caneva, S.; van der Zant, H. S. J.; Niklaus, F.; Stemme, G. Massively Parallel Fabrication of Crack-Defined Gold Break Junctions Featuring Sub-3 Nm Gaps for Molecular Devices. *Nat. Commun.* **2018**, *9* (1). https://doi.org/10.1038/s41467-018-05785-2.

(139) Banerjee, A.; Khan, S. U. H.; Broadbent, S.; Likhite, R.; Looper, R.; Kim, H.; Mastrangelo, C. H. Batch-Fabricated α-Si Assisted Nanogap Tunneling Junctions. *Nanomaterials* **2019**, *9* (5). https://doi.org/10.3390/nano9050727.

(140) Simmons, J. G. Generalized Formula for the Electric Tunnel Effect between Similar Electrodes Separated by a Thin Insulating Film. *J. Appl. Phys.* **1963**, *34* (6). https://doi.org/10.1063/1.1702682.

(141) Hu, L.; Chen, G. Analysis of Optical Absorption in Silicon Nanowire Solar Cells. *ASME Int. Mech. Eng. Congr. Expo. Proc.* **2007**, *8*, 1285–1287. https://doi.org/10.1115/IMECE2007-43422.

(142) Muthukumar, M.; Bobji, M. S. Effect of Micropillar Surface Texturing on Friction under Elastic Dry Reciprocating Contact. *Meccanica* **2018**, *53* (9), 2221–2235. https://doi.org/10.1007/s11012-017-0816-9.

(143) Didier, C. M.; Kundu, A.; DeRoo, D.; Rajaraman, S. Development of in Vitro 2D and 3D Microelectrode Arrays and Their Role in Advancing Biomedical Research. *J. Micromechanics Microengineering* **2020**, *30* (10), 103001. https://doi.org/10.1088/1361-6439/ab8e91.

(144) Choi, J. S.; Lee, H. J.; Rajaraman, S.; Kim, D.-H. Recent Advances in Three-Dimensional Microelectrode Array Technologies for in Vitro and in Vivo Cardiac and Neuronal Interfaces. *Biosens. Bioelectron.* **2021**, *171* (October 2020), 112687. https://doi.org/10.1016/j.bios.2020.112687.

(145) Vaezi, M.; Seitz, H.; Yang, S. A Review on 3D Micro-Additive Manufacturing Technologies. *Int. J. Adv. Manuf. Technol.* **2013**, *67* (5–8), 1721–1754. https://doi.org/10.1007/s00170-012-4605-2.

(146) Cho, Y. H.; Park, Y.-G.; Kim, S.; Park, J.-U. 3D Electrodes for

Bioelectronics. *Adv. Mater.* **2021**, *33* (47), 2005805. https://doi.org/https://doi.org/10.1002/adma.202005805.

(147) Tian, G.; Liu, Y.; Yu, M.; Liang, C.; Yang, D.; Huang, J.; Zhao, Q.; Zhang, W.; Chen, J.; Wang, Y.; Xu, P.; Liu, Z.; Qi, D. Electrostatic Interaction-Based High Tissue Adhesive, Stretchable Microelectrode Arrays for the Electrophysiological Interface. *ACS Appl. Mater. Interfaces* **2022**, *14* (4), 4852–4861. https://doi.org/10.1021/acsami.1c18983.

(148) Grob, L.; Rinklin, P.; Zips, S.; Mayer, D.; Weidlich, S.; Terkan, K.; Weiß, L. J. K.; Adly, N.; Offenhäusser, A.; Wolfrum, B. Inkjet-Printed and Electroplated 3D Electrodes for Recording Extracellular Signals in Cell Culture. *Sensors* **2021**, *21* (12), 3981. https://doi.org/10.3390/s21123981.

(149) Ali, M. A.; Hu, C.; Yttri, E. A.; Panat, R. Recent Advances in 3D Printing of Biomedical Sensing Devices. *Adv. Funct. Mater.* **2022**, *32* (9), 2107671. https://doi.org/10.1002/adfm.202107671.

(150) Cirelli, M.; Hao, J.; Bor, T. C.; Duvigneau, J.; Benson, N.; Akkerman, R.; Hempenius, M. A.; Vancso, G. J. Printing “Smart” Inks of Redox-Responsive Organometallic Polymers on Microelectrode Arrays for Molecular Sensing. *ACS Appl. Mater. Interfaces* **2019**, *11* (40), 37060–37068. https://doi.org/10.1021/acsami.9b11927.

(151) Choi, J. S.; Lee, H. J.; Rajaraman, S.; Kim, D. H. Recent Advances in Three-Dimensional Microelectrode Array Technologies for in Vitro and in Vivo Cardiac and Neuronal Interfaces. *Biosensors and Bioelectronics*. 2021. https://doi.org/10.1016/j.bios.2020.112687.

(152) Leber, M.; Körner, J.; Reiche, C. F.; Yin, M.; Bhandari, R.; Franklin, R.; Negi, S.; Solzbacher, F. Advances in Penetrating Multichannel Microelectrodes Based on the Utah Array Platform; Zheng, X., Ed.; Springer Singapore: Singapore, 2019; pp 1–40. https://doi.org/10.1007/978-981-13-2050-7_1.

(153) Szostak, K. M.; Grand, L.; Constandinou, T. G. Neural Interfaces for

Intracortical Recording: Requirements, Fabrication Methods, and Characteristics. *Frontiers in Neuroscience*. 2017.

(154) Zhang, K.; Xiao, X.; Wang, X.; Fan, Y.; Li, X. Topographical Patterning: Characteristics of Current Processing Techniques, Controllable Effects on Material Properties and Co-Cultured Cell Fate, Updated Applications in Tissue Engineering, and Improvement Strategies. *J. Mater. Chem. B* **2019**, *7* (45), 7090–7109. https://doi.org/10.1039/C9TB01682A.

(155) Adly, N.; Weidlich, S.; Seyock, S.; Brings, F.; Yakushenko, A.; Offenhäusser, A.; Wolfrum, B. Printed Microelectrode Arrays on Soft Materials: From PDMS to Hydrogels. *npj Flex. Electron.* **2018**, *2* (1), 15. https://doi.org/10.1038/s41528-018-0027-z.

(156) Rinklin, P.; Wolfrum, B. Recent Developments and Future Perspectives on Neuroelectronic Devices. *Neuroforum* **2021**, *27* (4), 213–224. https://doi.org/10.1515/nf-2021-0019.

(157) Hierlemann, A.; Frey, U.; Hafizovic, S.; Heer, F. Growing Cells Atop Microelectronic Chips: Interfacing Electrogenic Cells In Vitro With CMOS-Based Microelectrode Arrays. *Proc. IEEE* **2011**, *99* (2), 252–284. https://doi.org/10.1109/JPROC.2010.2066532.

(158) Bruno, G.; Colistra, N.; Melle, G.; Cerea, A.; Hubarevich, A.; Deleye, L.; De Angelis, F.; Dipalo, M. Microfluidic Multielectrode Arrays for Spatially Localized Drug Delivery and Electrical Recordings of Primary Neuronal Cultures. *Front. Bioeng. Biotechnol.* **2020**, *8* (June), 1–11. https://doi.org/10.3389/fbioe.2020.00626.

(159) Boretius, T.; Badia, J.; Pascual-Font, A.; Schuettler, M.; Navarro, X.; Yoshida, K.; Stieglitz, T. A Transverse Intrafascicular Multichannel Electrode (TIME) to Interface with the Peripheral Nerve. *Biosens. Bioelectron.* **2010**, *26* (1), 62–69. https://doi.org/10.1016/j.bios.2010.05.010.

(160) Fekete, Z. Recent Advances in Silicon-Based Neural Microelectrodes and

Microsystems: A Review. *Sensors Actuators B Chem.* **2015**, *215*, 300–315. https://doi.org/10.1016/j.snb.2015.03.055.

(161) Heuschkel, M. O.; Fejtl, M.; Raggenbass, M.; Bertrand, D.; Renaud, P. A Three-Dimensional Multi-Electrode Array for Multi-Site Stimulation and Recording in Acute Brain Slices. *J. Neurosci. Methods* **2002**, *114* (2), 135–148. https://doi.org/10.1016/S0165-0270(01)00514-3.

(162) Choi, C.; Lee, Y.; Cho, K. W.; Koo, J. H.; Kim, D.-H. Wearable and Implantable Soft Bioelectronics Using Two-Dimensional Materials. *Acc. Chem. Res.* **2019**, *52* (1), 73–81. https://doi.org/10.1021/acs.accounts.8b00491.

(163) Chen, X.; Rogers, J. A.; Lacour, S. P.; Hu, W.; Kim, D.-H. Materials Chemistry in Flexible Electronics. *Chem. Soc. Rev.* **2019**, *48* (6), 1431–1433. https://doi.org/10.1039/C9CS90019E.

(164) Lee, Y.; Kim, D.-H. Wireless Metronomic Photodynamic Therapy. *Nat. Biomed. Eng.* **2019**, *3* (1), 5–6. https://doi.org/10.1038/s41551-018-0341-8.

(165) Ganji, M.; Kaestner, E.; Hermiz, J.; Rogers, N.; Tanaka, A.; Cleary, D.; Lee, S. H.; Snider, J.; Halgren, M.; Cosgrove, G. R.; Carter, B. S.; Barba, D.; Uguz, I.; Malliaras, G. G.; Cash, S. S.; Gilja, V.; Halgren, E.; Dayeh, S. A. Development and Translation of PEDOT:PSS Microelectrodes for Intraoperative Monitoring. *Adv. Funct. Mater.* **2018**, *28* (12), 1700232. https://doi.org/https://doi.org/10.1002/adfm.201700232.

(166) Cho, Y. U.; Lee, J. Y.; Jeong, U.-J.; Park, S. H.; Lim, S. L.; Kim, K. Y.; Jang, J. W.; Park, J. H.; Kim, H. W.; Shin, H.; Jeon, H.; Jung, Y. M.; Cho, I.-J.; Yu, K. J. Ultra-Low Cost, Facile Fabrication of Transparent Neural Electrode Array for Electrocorticography with Photoelectric Artifact-Free Optogenetics. *Adv. Funct. Mater.* **2022**, *32* (10), 2105568. https://doi.org/10.1002/adfm.202105568.

(167) Lee, S. H.; Thunemann, M.; Lee, K.; Cleary, D. R.; Tonsfeldt, K. J.; Oh, H.; Azzazy, F.; Tchoe, Y.; Bourhis, A. M.; Hossain, L.; Ro, Y. G.; Tanaka,

A.; Kılıç, K.; Devor, A.; Dayeh, S. A. Scalable Thousand Channel Penetrating Microneedle Arrays on Flex for Multimodal and Large Area Coverage BrainMachine Interfaces. *Adv. Funct. Mater.* **2022**, *32* (25), 2112045. https://doi.org/https://doi.org/10.1002/adfm.202112045.

(168) Makvandi, P.; Kirkby, M.; Hutton, A. R. J.; Shabani, M.; Yiu, C. K. Y.; Baghbantaraghdari, Z.; Jamaledin, R.; Carlotti, M.; Mazzolai, B.; Mattoli, V.; Donnelly, R. F. Engineering Microneedle Patches for Improved Penetration: Analysis, Skin Models and Factors Affecting Needle Insertion. *Nano-Micro Lett.* **2021**, *13* (1), 93. https://doi.org/10.1007/s40820-021-00611-9.

(169) Zhao, Y.; Singaravelu, A. S. S.; Ma, X.; Zhang, Q.; Liu, X.; Chawla, N. Micromechanical Properties and Deformation Behavior of Al3BC/6061 Al Composites via Micropillar Compression. *Mater. Sci. Eng. A* **2020**, *773* (October 2019), 138852. https://doi.org/10.1016/j.msea.2019.138852.

(170) Goncalves, S. B.; Peixoto, A. C.; Silva, A. F.; Correia, J. H. Fabrication and Mechanical Characterization of Long and Different Penetrating Length Neural Microelectrode Arrays. *J. Micromechanics Microengineering* **2015**, *25* (5), 055014. https://doi.org/10.1088/0960-1317/25/5/055014.

(171) Jiang, C.; Lu, H.; Zhang, H.; Shen, Y.; Lu, Y. Recent Advances on In Situ SEM Mechanical and Electrical Characterization of Low-Dimensional Nanomaterials. *Scanning* **2017**, *2017*, 1–11. https://doi.org/10.1155/2017/1985149.

(172) Deng, F.; Lu, W.; Zhao, H.; Zhu, Y.; Kim, B.-S.; Chou, T.-W. The Properties of Dry-Spun Carbon Nanotube Fibers and Their Interfacial Shear Strength in an Epoxy Composite. *Carbon N. Y.* **2011**, *49* (5), 1752–1757. https://doi.org/10.1016/j.carbon.2010.12.061.

(173) Kaplan-Ashiri, I.; Cohen, S. R.; Gartsman, K.; Ivanovskaya, V.; Heine, T.; Seifert, G.; Wiesel, I.; Wagner, H. D.; Tenne, R. On the Mechanical Behavior of WS 2 Nanotubes under Axial Tension and Compression. *Proc. Natl. Acad. Sci.* **2006**, *103* (3), 523–528.

https://doi.org/10.1073/pnas.0505640103.

(174) Zhu, Y.; Xu, F.; Qin, Q.; Fung, W. Y.; Lu, W. Mechanical Properties of Vapor−Liquid−Solid Synthesized Silicon Nanowires. *Nano Lett.* **2009**, *9* (11), 3934–3939. https://doi.org/10.1021/nl902132w.

(175) Yue, Y.; Chen, N.; Li, X.; Zhang, S.; Zhang, Z.; Chen, M.; Han, X. Crystalline Liquid and Rubber-Like Behavior in Cu Nanowires. *Nano Lett.* **2013**, *13* (8), 3812–3816. https://doi.org/10.1021/nl401829e.

(176) Jennings, A. T.; Burek, M. J.; Greer, J. R. Microstructure versus Size: Mechanical Properties of Electroplated Single Crystalline Cu Nanopillars. *Phys. Rev. Lett.* **2010**, *104* (13), 135503. https://doi.org/10.1103/PhysRevLett.104.135503.

(177) Greer, J. R.; Kim, J.-Y.; Burek, M. J. The In-Situ Mechanical Testing of Nanoscale Single-Crystalline Nanopillars. *JOM* **2009**, *61* (12), 19–25. https://doi.org/10.1007/s11837-009-0174-8.

(178) Shahbeyk; Voyiadjis; Habibi; Astaneh; Yaghoobi. Review of Size Effects during Micropillar Compression Test: Experiments and Atomistic Simulations. *Crystals* **2019**, *9* (11), 591. https://doi.org/10.3390/cryst9110591.

(179) Sundararajan, S.; Bhushan, B. Development of AFM-Based Techniques to Measure Mechanical Properties of Nanoscale Structures. *Sensors Actuators A Phys.* **2002**, *101* (3), 338–351. https://doi.org/10.1016/S0924-4247(02)00268-6.

(180) Gordon, M. J.; Baron, T.; Dhalluin, F.; Gentile, P.; Ferret, P. Size Effects in Mechanical Deformation and Fracture of Cantilevered Silicon Nanowires. *Nano Lett.* **2009**, *9* (2), 525–529. https://doi.org/10.1021/nl802556d.

(181) MicroChemicals. Application Notes - Spin-Coating. *Datasheet* **2019**.

(182) Pratt, J. R.; Shaw, G. A.; Kumanchik, L.; Burnham, N. A. Quantitative Assessment of Sample Stiffness and Sliding Friction from Force Curves in

Atomic Force Microscopy. *J. Appl. Phys.* **2010**, *107* (4), 044305. https://doi.org/10.1063/1.3284957.

(183) Corporation, J. Printed Electronic Materials Product Line Overview Development and Commercialization of Printed. No. September 2021.

(184) Cardarelli, F. Less Common Nonferrous Metals BT - Materials Handbook: A Concise Desktop Reference; Cardarelli, F., Ed.; Springer International Publishing: Cham, 2018; pp 317–695. https://doi.org/10.1007/978-3-319-38925-7_4.

(185) Chitrakar, C.; Hedrick, E.; Adegoke, L.; Ecker, M. Flexible and Stretchable Bioelectronics. *Materials (Basel).* **2022**, *15* (5). https://doi.org/10.3390/ma15051664.